Hadron-Hadron Interactions from $N_f = 2 + 1 + 1$ Lattice QCD

The ρ-resonance

Dissertation
zur
Erlangung des Doktorgrades (Dr. rer. nat.)
der
Mathematisch-Naturwissenschaftlichen Fakultät
der
Rheinischen Friedrich-Wilhelms-Universität Bonn

von
Markus Alexander Oliver Werner
aus
Lindenfels

Bonn, 19.09.2019

Dieser Forschungsbericht wurde als Dissertation von der Mathematisch-Naturwissenschaftlichen Fakultät der Universität Bonn angenommen und ist auf dem Hochschulschriftenserver der ULB Bonn http://nbn-resolving.de/urn:nbn:de:hbz:5n-56974 elektronisch publiziert.

1. Gutachter:	Prof. Dr. Carsten Urbach
2. Gutachter:	Prof. Dr. Tom Luu
Tag der Promotion:	08.11.2019
Erscheinungsjahr:	2020

Abstract

In this work the calculation of the ρ resonance's decay parameters with $N_f = 2 + 1 + 1$ flavour lattice QCD is presented. The calculation is performed based on gauge configuration ensembles produced by the ETM collaboration which were generated with three different lattice spacing values and pion masses ranging from 230 MeV to 500 MeV. The calculation of resonance parameters with Lattice QCD requires correlation functions of all relevant decay channels in multiple moving reference frames. In this work operators resembling a ρ meson as well as a $\pi^+\pi^-$–system are used. The boost to moving frames breaks rotational symmetry and thereby causes a level splitting. Operators which transform like basis states of the reduced symmetry groups' irreducible representations are constructed to determine each energy level individually. Aided by the stochastic Laplacian Heaviside method correlation functions are calculated for all lattice momenta up to $(0, 0, 2)$ and all irreducible representations that emerge.

From these correlation functions energy levels are determined under consideration of systematic error sources. Most notably the effect of thermal pollutions and bias from fit range selection are taken into account. By applying the Lüscher method the energy spectra are translated into phase shift curves on each ensemble separately. From a Breit-Wigner fit to the phase shift curves the ρ meson mass and width on all ensembles are determined. The results are fed into a combined fit of mass and width and extrapolated to the chiral and continuum limit.

The main result of this thesis are the continuum extrapolated values of M_ρ and Γ_ρ at the physical point which were determined to

$$M_\rho \;=\; 769(19)\ \text{MeV}\,, \qquad \Gamma_\rho \;=\; 129(7)\ \text{MeV}\,.$$

Lattice artefacts could not be resolved within the statistical uncertainties of this work. While the ρ-meson massis in very good agreement with experiment the corresponding decay width differs by about two standard deviations from its experimental counterpart. The results of this thesis were pre-published in [1].

Danksagung

Ich möchte an dieser Stelle allen danken, die mich in den letzten Jahren unterstützt und damit diese Dissertation erst möglich gemacht haben.

Ganz besonders danken möchte ich meinen Eltern, Renate und Manfred Werner und meiner Freundin Hannah. Ich danke meinem Bruder Stefan sowie all den Freunden, die mich durch mein Studium begleitet haben: Marcel, Anton und Julius; Tobi, Yannik und Michel; Christian, Christopher und Martin.

Weiterhin besonders danken möchte ich meinem Doktorvater Carsten Urbach. Ich danke Tom sowie all den Kollegen, die meinen Alltag bereichert und meinen fachlichen Horizont erweitert haben: Bastian Knippschild als meinen ersten Betreuer; Christian, Christopher, Martin und ganz besonders Tobi zum zweiten Mal; Akaki, Barbara, Bartek, Bastian Kubis, Bernard, Marcus, Malwin und allen anderen deren Namen ich an dieser Stelle nicht alle aufzählen kann.

Danke.

Contents

1 Introduction **1**

2 Theoretical Background **5**
2.1 Scattering . . . 5
2.1.1 Asymptotic states . . . 5
2.1.2 The S-matrix . . . 6
2.1.3 Resonances . . . 7
2.2 Quantum Chromodynamics: The theory of strong interaction . . . 8
2.2.1 Discretization of the action . . . 9
2.2.2 Sampling of the path integral . . . 13
2.2.3 Resampling of gauge configurations . . . 14
2.3 Scattering on the lattice . . . 15
2.3.1 Derivation of the Lüscher formula . . . 16
2.3.2 Moving reference frames . . . 19
2.3.3 Angular momentum on the Lattice . . . 20
2.3.4 Subduction of the Lüscher formula . . . 23
2.4 Angular momentum basis in moving frames . . . 24
2.5 The relation between equivalent moving frames . . . 25
2.5.1 The Orbit stabilizer theorem . . . 26
2.5.2 Conjugation of little groups . . . 28
2.5.3 Projection operator . . . 28
2.6 Extraction of Energy Levels . . . 29

3 Operators for the ρ meson **31**
3.1 The Rho meson . . . 31
3.2 Operator construction . . . 32
3.2.1 Continuum operators . . . 33
3.2.2 Operators in the twisted basis . . . 35
3.3 Projection of operators . . . 36
3.3.1 Set of ρ operators . . . 40

4 Wick contractions **41**
4.1 Wick contractions . . . 41
4.1.1 Wick contractions for the ρ^0 meson . . . 42
4.1.2 Thermal states . . . 48
4.1.3 Weighting and Shifting . . . 50

5 Numerical Setup **53**
5.1 Numerical Setup . . . 53
5.1.1 Scale Setting . . . 53
5.2 sLapH method . . . 54
5.2.1 Laplacian Heaviside smearing . . . 54
5.2.2 Stochastic Estimation . . . 57
5.3 Correlation functions with Quarkline estimates . . . 59

6 Results **61**
6.1 Pion Dispersion Relation . . . 61
6.2 Energy Levels . . . 62
6.3 Phase Shift Determination . . . 65
6.4 Pion Mass Dependence . . . 69
6.5 Discussion . . . 73

7 Summary **77**

Bibliography **79**

A Appendix **87**
A.1 Point Group Theory Tables . . . 87
A.2 Subduction coefficients . . . 92
A.3 Dirac matrix conventions . . . 94
A.4 Implemented diagrams . . . 94

List of Figures **101**

List of Tables **103**

CHAPTER 1

Introduction

Physical phenomena have been observed from cosmologic down to subatomic scale. Just four fundamental interactions are capable of describing the world over all these orders of magnitude: Gravitation describes the attraction of mass. Electromagnetism describes the electric and magnetic forces between electromagnetically charged objects. The strong interaction describes the interaction between quarks and gluons it is responsible for the formation of nuclei and a wealth of other particles called hadrons. Finally the weak interaction mediates certain transitions that would not occur otherwise.

Each of these four interactions may be described as a field. With gavity as the exception, electromagnetism and both, the weak and the strong force can be formulated as a quantum field theory. The former two can be unified into the Glashow-Weinberg-Salam (GWS) or "electroweak" theory. The latter is described by Quantum Chromodynamics (QCD). They are merged into the standard model of particle physics which has been very successful in describing the physics at subatomic scale. Still it is not complete and experimental results which differ from their predicted value have become a hot topic in research as they could be the key to understand physics beyond the standard model (BSM).

One of the most prominent of such observables is the muon $g-2$ anomalous moment where experiment and theory differ by 4 standard deviations [2]. On the theoretical side the uncertainty is nowadays dominated by hadronic contributions which are mediated by the strong interaction. This is due to the arguably most peculiar feature of QCD: The coupling constant increases with decreasing energy. At the typical energy scale of a hadron, around 1GeV, perturbative expansions in the coupling constant no longer converge. To describe the physical phenomena at this energy scale effective field theories, in particular Chiral Perturbation Theory (χPT) [3–5] and dispersion theory [6, 7] have been used to great success. However, χPT relies on unknown low energy constants for its predictions and therefore requires experimental input.

With the advent of high performance computing it became possible to estimate physical observables at low energies stochastically with a method named lattice QCD [8]. By approximating spacetimewith a hypercubic lattice, QCD is regulated in both, the ultraviolet and the infrared regime. This regularization synergizes well with the path integral formalism as the integral's value may be estimated in a systematically improvable fashion by generating ensembles with Monte Carlo methods. The computing power required to generate such an ensemble are enormous but decrease drastically with increasing quark mass and coupling constant.[1] Therefore usually a set of (cheaper) ensembles with unphysical input parameters are generated and the

[1] This is more commonly as decreasing β-value or equivalently increasing lattice spacing for practical reasons.

connection to the real world is established by extrapolating to the physical values. At present lattice QCD is the only method available at low energies that relies solely on first principles.

This thesis addresses the description of resonances, in particular the ρ resonance, with lattice QCD. As the lightest vector meson the ρ resonance plays an important role in the standard model. Among the aforementioned hadronic contributions to the muon $g-2$ anamalous moment the hadronic vacuum polarization and hadronic light-by-light contribution like many other processes can be understood within the context of vector meson dominance which informally states that the exchange of vector mesons is the dominating mechanism in electromagnetic and final state interactions of hadrons. For a review see [9].

Experimentally the ρ resonance was established in the early 1960s [10–14]. Nowadays the experimental accuracy is below the per mil level. As a resonance the ρ has a finite lifetime. It is usually parametrized by the "phase shift" $\delta_1(E_{\mathrm{CM}})$ depicted in Figure 1.1. The curve as a

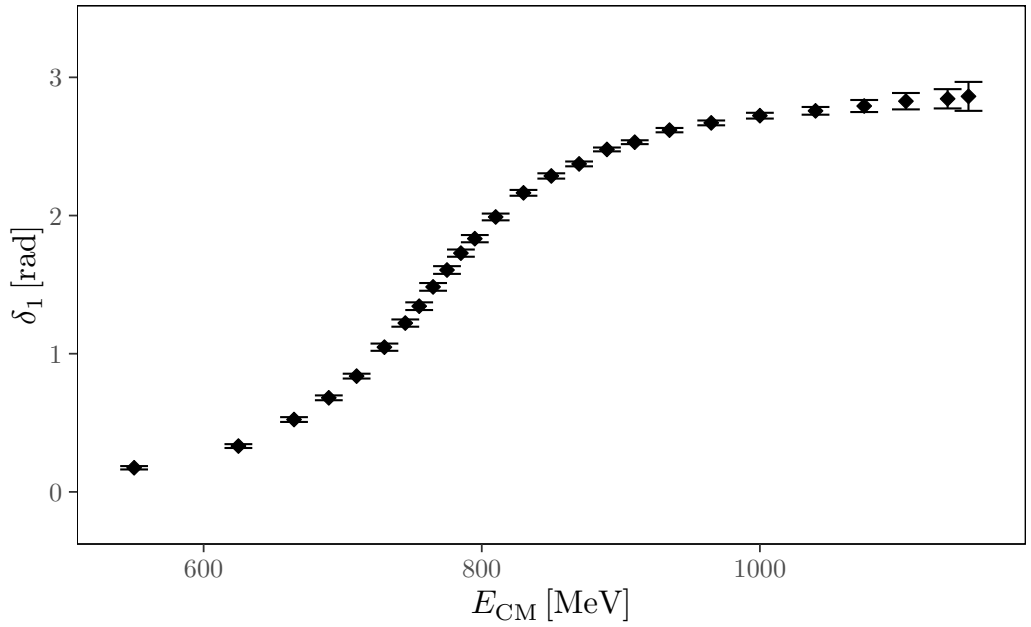

Figure 1.1: Experimental phase shift data for the ρ meson [15]. The characteristic S-shape of resonances can be clearly observed.

function of the energy exhibits the characteristic "S"-shape of a resonance curve. This is an ideal scenario which occurs because the ρ decays almost exclusively into pairs of pions and nearly no background phase is observable. The absence of complications by multi-channel branching ratios or background phase in addition to its importance makes the ρ meson is the logical first candidate to attempt a study of resonances with lattice QCD.

The study of unstable particles with lattice QCD requires special care. The volume is finite and in order to use Monte Carlo methods a Wick rotation to euclidean spacetime is required. Therefore infinite volume scattering properties can only be computed indirectly using the by now famous Lüscher method [16–18]. Since its conception the Lüscher method has been developed further in many directions. For a review see [19]. In this work the extension to moving frames will be used [20–22]. The finite lifetime of resonances manifests itself as a energy width. To capture this feature the scattering properties must be determined over a range of different energies. Moving frames allow one to map out the phase shift by using many different scattering

momenta on a single ensemble rather than by using many different volumes which each require the generation of a new ensemble.

For a long time the Lüscher method was difficult to apply to the ρ in realistic lattice calculations, albeit some early attempts [23, 24]. By now, there are a number of investigations of the ρ meson from lattice QCD using the Lüscher method [21, 25–33]. The first computation with light dynamical up and down quarks can be found in the pioneering work of Ref. [21]. Subsequent investigations focused on different aspects like large operator bases [34] or asymmetric boxes [31]. Recently, a first investigation involving different lattice spacings and a range of pion masses has been performed [33]. However, in the latter reference chiral and continuum extrapolations could not be taken.

In this thesis the ρ meson is computed applying the Lüscher method using gauge ensembles generated with $N_f = 2 + 1 + 1$ dynamical quark flavours by the ETM collaboration at three different lattice spacing values and a wide range of pion masses [35, 36]. This allows a controlled chiral and continuum extrapolation of the ρ meson mass and width.

This thesis is structured as follows: In Chap. 2 the foundations for the remainder of this work are laid. Scattering theory as well as Lattice QCD are briefly recapitulated. The Lüscher formalism is introduced and finally the implications of moving reference frames are discussed. The application to the ρ meson is discussed in Chap. 3 about operators and in Chap. 4 about Wick contractions. In Chap. 5 the setup of the numerical calculation is bridging to the results that are finally presented in Chap. 6.

Lastly many of the more technical details are deepened in the appendix.

CHAPTER 2

Theoretical Background

2.1 Scattering

The ρ meson appears as a resonance in $\pi\pi$ scattering. Therefore it will be useful to recapitulate scattering in quantum field theory. This section closely follows [37]. Starting from asymptotic quantum fields, the S-matrix introduced and parametrized by the phase shift. The characteristic "S"-shape of the phase shift for resonant channels is motivated. Reproducing this feature from first principles is one of the main goals of this thesis.

2.1.1 Asymptotic states

The starting point may be any quantum theory with Hamiltonian $\mathcal{H}$ and eigenstates Ψ_α such that the Schrödinger equation

$$\mathcal{H}\Psi_\alpha = (\mathcal{H}_0 + V)\Psi_\alpha = E_\alpha \Psi_\alpha \tag{2.1}$$

is fulfilled. The potential V contains the interaction terms which usually impede a closed solution of Schrödinger's equation. However, any interaction becomes negligible at a certain distance and in a typical scattering experiment any observation takes place far beyond this distance.

Let the "incoming" fields Ψ^+_α and "outgoing" fields Ψ^-_α be at $t \to -\infty$ before and $t \to +\infty$ after a collision. Let Φ_α be solutions for the free Schrödinger equation

$$\mathcal{H}_0\Phi_\alpha = E_\alpha \Phi_\alpha \tag{2.2}$$

where we assumed the same eigenvalues to appear as for the full solution.[1]

We may derive a formal solution for the Schrödinger equation by expressing $\Psi^\pm_\alpha$ in terms of the free fields. This leads to the Lippmann–Schwinger equation:

$$\Psi^\pm_\alpha = \Phi_\alpha + \int \mathrm{d}\beta \; \frac{\mathrm{T}^\pm_{\beta\alpha}\Phi_\beta}{E_\alpha - E_\beta \pm i\epsilon} \tag{2.3}$$

where the T -matrix is given by

$$\mathrm{T}^\pm_{\beta\alpha} = \left\langle \Phi_\beta \right| V \left| \Psi^\pm_\alpha \right\rangle \tag{2.4}$$

[1] This might require to absorb certain terms into V

In order to localize the incoming and outgoing fields in time, consider a wave packet

$$\Psi_g^{\pm}(t) = \int \mathrm{d}\alpha \; \mathrm{e}^{-\mathrm{i}E_\alpha t} g(\alpha) \Psi_\alpha^{\pm} \tag{2.5}$$

and analogously for $\Phi_g(t)$. By applying the Lippmann–Schwinger equation (2.3) to equation (2.5) we obtain

$$\Psi_g^{\pm}(t) = \Phi_g^{\pm} + \int \mathrm{d}\alpha \int \mathrm{d}\beta \; \frac{\mathrm{e}^{-\mathrm{i}E_\alpha t} g(\alpha) \mathrm{T}_{\beta\alpha}^{\pm} \Phi_\beta}{E_\alpha - E_\beta \pm \mathrm{i}\epsilon} \tag{2.6}$$

$$= \Phi_g^{\pm} + \int \mathrm{d}\beta \; \Phi_\beta \int \mathrm{d}\alpha \; \frac{\mathrm{e}^{-\mathrm{i}E_\alpha t} g(\alpha) \mathrm{T}_{\beta\alpha}^{\pm}}{E_\alpha - E_\beta \pm \mathrm{i}\epsilon} \,. \tag{2.7}$$

To solve the integral over α the standard approach is, to close the contour integral such that the exponential $\mathrm{e}^{-\mathrm{i}E_\alpha t}$ vanishes for $\mathrm{Im}(E_\alpha) \neq 0$ and $t \to \pm\infty$ and apply Cauchy's integral theorem. For in the upper (Ψ_g^+) or lower (Ψ_g^-) complex half-plane – depending on the sign of t.

In general $g(\alpha)$ and $\mathrm{T}_{\beta\alpha}$ may have poles enclosed in the contour. Specifically a pole at

$$E_\alpha = E_R - \mathrm{i}\frac{\Gamma}{2} \tag{2.8}$$

would lead to a contribution proportional to $\mathrm{e}^{-\Gamma t/2}$. The probability of such a state is given by its absolute value squared and thus decays like $\mathrm{e}^{-\Gamma t}$. We will revisit this result when introducing resonances in section 2.1.3.

It also proves that wave packets of incoming and outgoing states approach a free wave packet in the limit where t becomes very large

$$\int \mathrm{d}\alpha \; \mathrm{e}^{-\mathrm{i}E_\alpha t} g(\alpha) \Psi_\alpha^{\pm} \to \int \mathrm{d}\alpha \; \mathrm{e}^{-\mathrm{i}E_\alpha t} g(\alpha) \Phi_\alpha \,. \tag{2.9}$$

Therefore the fields $\Psi_\alpha^{\pm}$ are also called "asymptotic states".

2.1.2 The S-matrix

The asymptotic states describe the fields before and after a collision.The interaction might cause a transition $\alpha \to \beta$. Let the S-matrix be the complex matrix of probability amplitudes

$$S_{\beta\alpha} = \left\langle \Psi_\beta^-| \; \Psi_\alpha^+ \right| \Psi_\beta^-| \; \Psi_\alpha^+ \right\rangle \,. \tag{2.10}$$

In Equation (2.7) the asymptotic states were expressed in terms of free states and the T -matrix. By using the S-matrix the outgoing states may as well be expressed in terms of the incoming states

$$\Psi_g^+(t) = \int \mathrm{d}\beta \; \Psi_\beta^- \mathrm{e}^{-\mathrm{i}E_\beta t} \int \mathrm{d}\alpha \; g(\alpha) S_{\beta\alpha} \tag{2.11}$$

and vice versa. Comparing both equations yields

$$S_{\beta\alpha} = \delta(\beta - \alpha) - 2\mathrm{i}\pi\delta(E_\alpha - E_\beta)\mathrm{T}_{\beta\alpha}^{+} \tag{2.12}$$

If only the connected part of the S-matrix is considered (that is there is no unchanged subsystem of α still in β), the delta distributions may be factored out:

$$S_{\beta\alpha} = -2\pi \mathrm{i}\delta^{(4)}(p_\beta - p_\alpha) M_{\beta\alpha}\,. \tag{2.13}$$

The transition $\alpha \to \beta$ is then completely parametrized by $M_{\beta\alpha}$

2.1.3 Resonances

In many multi-particle collision processes, the participating particles can form an intermediate state consisting of a single unstable particle R, that eventually decays into the particles observed as finite state. If the total decay rate is relatively small with regard to the rate of oscillation of the wave function in its rest frame $\hbar/M_R$ the cross section exhibits a rapid variation (usually a peak) at the energy of the intermediate state R This is known as "resonance". It will proof useful to express S in a basis where all variables except for total momentum $\boldsymbol{p}$ and energy E are denoted by a multiindex N.

$$S_{N',N}(E, \boldsymbol{p}) = \delta_{N',N} - 2\mathrm{i}\pi M_{N',N}(E, \boldsymbol{p}) \tag{2.14}$$

In the center-of-mass frame near the pole it becomes

$$S_{N'N}(E, \mathbf{0}) = \mathcal{S}_{0N'N} + \frac{\mathcal{R}_{N'N}}{E - E_R + \mathrm{i}\Gamma/2} \equiv \mathcal{S}_{N'N}(E) \tag{2.15}$$

$\mathcal{S}_{0N'N}$ denotes the non-resonant background S-matrix and is approximately constant over the relevant energy range. The pole at $E_R + \mathrm{i}\Gamma/2$ procures the correct decay rate for the resonance as already discussed section 2.1.1 and $\mathcal{R}_{N'N}$ denotes the residue. In general $\mathcal{S}_0$ and $\mathcal{R}$ receive contributions from all possible asymptotic states.

The result assumes a particularly simple form if only one channel couples to the resonance because $\mathcal{S}$ is nonzero if and only if $N' = N$. In this case the non-resonant background may be parametrized by a single number δ_{0N} such that

$$\mathcal{S}_{0N'N} = \exp(2\mathrm{i}\delta_{0N})\delta_{N'N}\,. \tag{2.16}$$

From the unitarity condition for $\mathcal{S}$ follows $\mathcal{R} = -\mathrm{i}\Gamma \exp(2\mathrm{i}\delta_{0N})\delta_{N'N}$. This yields

$$\mathcal{S}_{N'N}(E) = \delta_{N'N}\left(1 - \frac{\mathrm{i}\Gamma}{E - E_R + \mathrm{i}\Gamma/2}\right)\exp(2\mathrm{i}\delta_{0N}) = \delta_{N'N}\exp(2\mathrm{i}\delta_N(E)) \tag{2.17}$$

where we defined the phase shift

$$\delta_N(E) = \delta_{0N} - \arctan\left(\frac{\Gamma/2}{E - E_R}\right)\,. \tag{2.18}$$

In the range from $E_R - \Gamma$ to $E_R + \Gamma$ the phase shift as a function of the energy is rising from δ_{0N} to $\delta_{0N} + \pi$ following the characteristic "S"-shape which was already presented in Figure 1.1.

2.2 Quantum Chromodynamics: The theory of strong interaction

While the scattering theory discussed in section 2.1 holds quite generally, the decay $\rho \to \pi\pi$ is governed by the strong force. The accepted theory of strong force is Quantum Chromodynamics (QCD). This chapter is intended to briefly summarize the features of QCD and lattice QCD relevant for this work and for the most part leans on [38] and [39].

QCD describes the interaction of quarks and gluons. Its fundamental degrees of freedom are the coupling constant α_s (or coupling strength g_s; $\alpha_s = g_s^2/4\pi$) and the quark masses m_q. One prominent feature is the energy dependence of α_s, often called "running coupling". It is obeys the renormalization group equation

$$\mu_R^2 \frac{\mathrm{d}\alpha_s}{\mathrm{d}\mu_R^2} = -(b_0\alpha_s^2 + b_1\alpha_s^3 + b_2\alpha_s^4 + \dots)\,. \tag{2.19}$$

When the renormalization scale μ_R decreases the coupling constant increases. For "soft processes" with momentum transfers lower than $\sim 4 - 10$ GeV, QCD becomes non-perturbative in the coupling constant. The mass of the ρ meson given in Eq. (3.2) is well below this scale. There exist several propositions how to calculate physical observables without relying on perturbation theory. In this work we will use Lattice QCD a non-perturbative formulation which is derived from first principles.

The Lagrangian of QCD is given by

$$\mathcal{L}_{\mathrm{QCD}} = \sum_f \bar{\psi}_f(x)\left(\gamma^\mu(\partial_\mu + \mathrm{i}A_\mu(x)) + m_f\right)\psi_f(x) + \frac{1}{2g^2}\,\mathrm{tr}(F_{\mu\nu}F^{\mu\nu}) \tag{2.20}$$

where as usual ψ_f denotes quark fields with flavor f, A_μ denotes the gluon field and $F_{\mu\nu} = \partial_\mu A_\nu(x) - \partial_\nu A_\mu(x) + \mathrm{i}[A_\mu(x), A_\nu(x)]$ is the field strength tensor. Additionally an explicitly CP-violating term $\theta\frac{\alpha_s}{16\pi}\epsilon^{\mu\nu\sigma\rho}F^A_{\mu\nu}F^A_{\sigma\rho}$ would be possible. However if it is there, the coefficient is very small. The most precise upper limit for θ stems from neutron electric dipole moment measurements and constrains $|\theta| \lesssim 10^{-10}$. For the quantities relevant in this work, it may be safely neglected.

Lattice QCD is naturally formulated in the path integral formalism. It describes the expectation value of an interpolating field operator $\mathcal{O}$ as the integral

$$\langle\mathcal{O}\rangle = \frac{1}{Z}\int \mathcal{D}\psi\ \mathcal{D}\bar{\psi}\ \mathcal{D}A\ \mathrm{e}^{\mathrm{i}S_{\mathrm{QCD}}[\psi,\bar{\psi},A]}\mathcal{O}[\psi,\bar{\psi},A] \tag{2.21}$$

where the partition function Z and action S are defined as

$$Z = \int \mathcal{D}\psi\ \mathcal{D}\bar{\psi}\ \mathcal{D}A\ \mathrm{e}^{\mathrm{i}S_{\mathrm{QCD}}[\psi,\bar{\psi},A]}\,, \qquad S_{\mathrm{QCD}} = \int \mathrm{d}^4x\ \mathcal{L}_{\mathrm{QCD}}\,. \tag{2.22}$$

Replacing spacetime by a finite lattice simultaneously regulates infrared as well as ultraviolet divergences. It also makes finite the dimension of the path integral. By sampling the space of possible field configurations the path integral and therefore the vacuum expectation value of an operator may be estimated. To rewrite the path integral for a lattice, first a discretized version of the action, the "lattice action", is required.

2.2.1 Discretization of the action

The naive fermion action

The Lagrangian and therefore also the action of QCD is gauge invariant under the $\mathrm{SU}(3)_{\mathrm{color}}$ gauge transformations

$$\psi(x) \xrightarrow{\text{g.t.}} \Omega(x)\psi(x) \tag{2.23}$$

$$\mathrm{A}_\mu(x) \xrightarrow{\text{g.t.}} \Omega(x)A_\mu(x)\Omega(x)^\dagger + \mathrm{i}(\partial_\mu\Omega(x))\Omega(x)^\dagger\,. \tag{2.24}$$

Let Λ be the aforementioned four-dimension lattice

$$\Lambda = \{\, n = (n_0, n_1, n_2, n_3) \mid 0 \le n_0 \le T,\ 0 \le n_i \le L \,\} \tag{2.25}$$

with extent L in spatial and T in temporal direction and in units of the lattice spacing a. Integrals become sums and derivatives are discretized.

$$\int \mathrm{d}^4x \to a^4 \sum_{n\in\Lambda}, \qquad \partial_\mu\psi(n) \to \frac{\psi(n+\hat{\mu}) - \psi(n-\hat{\mu})}{2a} \tag{2.26}$$

In the second equation, $\hat{\mu}$ denotes a translation by one in direction μ. With the derivative defined in Eq. (2.26), the Lagrangian would obtain terms $\gamma^\mu\bar{\psi}(n)\psi(n\pm\hat{\mu})$ which violate gauge invariance:

$$\bar{\psi}(n)\psi(n+\hat{\mu}) \xrightarrow{\text{g.t.}} \bar{\psi}(n)\Omega(n)^\dagger\Omega(n+\hat{\mu})\psi(n+\hat{\mu}) \neq \bar{\psi}(n)\psi(n+\hat{\mu})\,. \tag{2.27}$$

To preserve gauge invariance change from the algebra-valued gauge fields $A_\mu(x)$ to group valued gauge fields

$$U_\mu(n) = \exp(\mathrm{i}aA_\mu(n)) \tag{2.28}$$

which transform as

$$U_\mu(n) \xrightarrow{\text{g.t.}} \Omega(n)U_\mu(n)\Omega(n+\hat{\mu})^\dagger + \mathcal{O}\left(a^2\right) \tag{2.29}$$

under gauge transformations. They are the lattice equivalent of the parallel transporter in the continuum. Upon replacing Eq. (2.26) by

$$\partial_\mu\psi(n) \to \frac{U_\mu(n)\psi(n+\hat{\mu}) - U_\mu(n-\hat{\mu})^\dagger\psi(n-\hat{\mu})}{2a} \tag{2.26'}$$

it is straightforward to show that the gauge invariance of $\bar{\psi}\partial_\mu\psi$ and therefore the kinetic part of Eq. (2.20) is preserved. Furthermore holds up to lattice artifacts

$$U_\mu(n) = 1 + \mathrm{i}aA_\mu + \mathcal{O}\left(a^2\right). \tag{2.30}$$

Therefore the kinetic term of the action is up lattice artifacts

$$\begin{aligned} S_{\mathrm{F}}[\psi,\bar{\psi},U] &= a^4 \sum_{n\in\Lambda} \bar{\psi}(n)\gamma^\mu \frac{U_\mu(n)\psi(n+\hat{\mu}) - U_\mu(n-\hat{\mu})^\dagger\psi(n-\hat{\mu})}{2a} + m\bar{\psi}(n)\psi(n) \\ &= a^4 \sum_{n\in\Lambda} \bar{\psi}(n)\gamma^\mu\partial_\mu\psi(n) + \bar{\psi}(n)\gamma^\mu \frac{\mathrm{i}A_\mu(n)\psi(n+\hat{\mu}) - \mathrm{i}A_\mu(n-\hat{\mu})\psi(n-\hat{\mu})}{2} \\ &\qquad + m\bar{\psi}(n)\psi(n) + \mathcal{O}(a) \\ &= a^4 \sum_{n\in\Lambda} \bar{\psi}(n)(\gamma^\mu(\partial_\mu + \mathrm{i}A_\mu(n)) + m)\psi(n) + \mathcal{O}(a) \end{aligned} \tag{2.31}$$

which already correctly approaches Eq. (2.20) in the continuum limit $a \to 0$. Eq. (2.31) is called naive fermion action. The gauge transporters $U_\mu(x)$ replace $A_\mu(x)$ as fundamental variables of the lattice Lagrangian.

The second term of the Lagrangian emerges in the continuum limit from a closed chain of gauge transporters. The smallest nontrivial closed loop on the lattice is the "plaquette"

$$U_{\mu\nu}(n) = U_\mu(n)U_\nu(n+\hat{\mu})U_\mu(n+\hat{\nu})^\dagger U_\nu(n)^\dagger\,. \tag{2.32}$$

Per construction the plaquette is gauge invariant. Inserting Eq. (2.28) for the factors of the plaquette and the Baker-Campbell-Hausdorff formula give

$$\begin{aligned} U_{\mu\nu}(n) &= \exp\Big(\mathrm{i}a^2(\partial_\mu A_\nu(n) - \partial_\nu A_\mu(n) + \mathrm{i}[A_\mu(n), A_\nu(n)]) + \mathcal{O}\Big(a^3\Big)\Big) \\ &= \exp\Big(\mathrm{i}a^2 F_{\mu\nu}(n) + \mathcal{O}\Big(a^3\Big)\Big) \end{aligned}$$

With this, the "Wilson gauge action" may be defined as

$$\begin{aligned} S_{\mathrm{G}}[U] &= \frac{2}{g^2}\sum_{n\in\Lambda}\sum_{\mu<\nu} \mathrm{Re}\,\mathrm{tr}(1 - U_{\mu\nu}(n)) \\ &= a^4 \sum_{n\in\Lambda} \frac{1}{2g^2}\sum_{\mu,\nu} \mathrm{tr}\Big(F_{\mu\nu}(n)^2\Big) + \mathcal{O}\Big(a^2\Big) \end{aligned} \tag{2.33}$$

which is correctly approaches Eq. (2.20) in the continuum limit as well. In this work an improved version of the gauge action, the Iwasaki action [40] is used.

The Wilson term

It will turn out in Sec. 2.2.2 that the integration over the fermion fields ψ and $\bar{\psi}$ may be separated from the rest of the path integral and performed analytically. Therefore it will prove useful to make explicit the dependence ψ and $\bar{\psi}$ already at this point. By introducing the "Dirac matrix"

$$D(n|m) = D_0(n|m) + m\delta_{n,m} = \sum_\mu \gamma_\mu \frac{U_\mu(n)\delta_{n+\hat{\mu},m} - U_{-\mu}(n)\delta_{n-\hat{\mu},m}}{2a} + m\delta_{n,m} \tag{2.34}$$

the action Eq. (2.31) may be reexpressed as

$$S_{\mathrm{F}}[\psi,\bar{\psi},U] \to a^4 \sum_{m,n\in\Lambda} \bar{\psi}(n) D(n|m) \psi(m)\,. \tag{2.35}$$

Applying a Fourier transformation to $D(n|m)$ and inverting yields the the propagator

$$\tilde{D}(p)^{-1} = \frac{m - \mathrm{i}a^{-1}\sum_\mu \gamma_\mu \sin(p_\mu a)}{m^2 + a^{-2}\sum_\mu \sin(p_\mu a)}^2 \tag{2.36}$$

in momentum space. While the propagator has the usual pole at $p^2 = m^2$, there are 15 additional poles from the freedom to add π/a to each component of p without changing the value of the sine. The existince of such unphysical solutions for the equations of motion of the naive fermion action from Eq. (2.31) is called "fermion doubling problem".

To remove these doublers one may add the "Wilson term"

$$-\frac{a}{2}\bar{\psi}\partial_\mu\partial^\mu\psi \to -a^5 \sum_{m,n\in\Lambda} \bar{\psi}(n) \sum_\mu \frac{U_\mu(n)\delta_{n+\hat{\mu},m} - 2\delta_{n,m} + U_{-\mu}(n)\delta_{n-\hat{\mu},m}}{2a^2}\psi(m) \tag{2.37}$$

to the naive fermion action. Because the Wilson term has dimension 5, it will vanish in the continuum limit. The Dirac matrix from Eq. (2.34) becomes

$$D(n|m) = D_{\mathrm{W}}(n|m) + m\delta_{n,m} \tag{2.38}$$

where we defined the "Wilson Dirac matrix"

$$\begin{aligned} D_{\mathrm{W}}(n|m) &= D_0(n|m) - a\frac{U_\mu(n)\delta_{n+\hat{\mu},m} - 2\delta_{n,m} + U_{-\mu}(n)\delta_{n-\hat{\mu},m}}{2a^2} \\ &= -\frac{1}{2a}\sum_\mu \left((1-\gamma_\mu)U_\mu(n)\delta_{n+\hat{\mu},m} + (1+\gamma_\mu)U_{-\mu}(n)\delta_{n-\hat{\mu},m}\right) + \frac{4}{a}\delta_{n,m}\,. \end{aligned} \tag{2.39}$$

The Wilson term acts like an additional mass term $\Delta m = 2/a$ for each nonvanishing component of p. Therefore in the continuum limit the doubler's mass becomes infinite and they decouple from the theory while the physical solution remains unchanged.

The twisted mass

Introducing the Wilson term comes at a cost. The generators of axial transformations and therefore chiral symmetry are explicitly broken. In fact, it has been shown that it is not possible to find a doubler-free discretization in four dimensions without breaking either chiral symmetry or Lorentz invariance [41]. Chiral symmetry can expressed by the non-homogeneous anticommutator relation

$$D\gamma_5 + \gamma_5 D = aD\gamma_5 D \tag{2.40}$$

for finite a. This is the "Ginsparg-Wilson equation". In the continuum limit the right hand side vanishes together with the Wilson term and the continuum anticommutator relation is recovered.

Assume an axial rotation

$$\boldsymbol{\psi} = \exp(i/2\omega_A^a \tau_a \gamma_5)\boldsymbol{\chi} \qquad \bar{\boldsymbol{\psi}} = \bar{\boldsymbol{\chi}} \exp(i/2\omega_A^a \tau_a \gamma_5) \tag{2.41}$$

where ω_A^a are the Lie parameters of the axial transformation, τ_a are the Pauli-matrices and everything will be formulated in terms of isospin doublets which are denoted by bold greek symbols. The set of fields χ is called "twisted basis" whereas up to now we worked in the "physical basis".

In the continuum, the kinetic part of the fermion action

$$S_{\mathrm{F}}[\boldsymbol{\psi}, \bar{\boldsymbol{\psi}}, A] = \int \mathrm{d}^4x \; \bar{\boldsymbol{\psi}}(\not{D} + m)\boldsymbol{\psi} \tag{2.42}$$

is still chirally invariant and only the mass term transforms to

$$\begin{aligned} m\bar{\boldsymbol{\psi}}\boldsymbol{\psi} &= m\bar{\boldsymbol{\chi}} \exp(i\boldsymbol{\omega}_A^a \tau_a \gamma_5)\boldsymbol{\chi} \\ &= m\cos(\omega_A)\bar{\boldsymbol{\chi}}\boldsymbol{\chi} + \mathrm{i}m\sin(\omega_A)\frac{\boldsymbol{\omega}_A^a}{\omega_A}\bar{\boldsymbol{\chi}}\tau_a\gamma_5\boldsymbol{\chi}\,. \end{aligned} \tag{2.43}$$

On the lattice however, the Wilson term transforms as well and therefore applying the axial rotation results in a different infrared regulator. The following discussion of twisted mass lattice QCD is in addition to [39] inspired by [42].

One usally chooses $\boldsymbol{\omega}_A = (0, 0, \alpha_{\mathrm{tm}}\tau_3)$ and flavor symmetry is reduced to an exact U(1) symmetry with generator τ_3. With the definitions $m_0 = m\cos(\alpha_{\mathrm{tm}})$ and $\mu = m\sin(\alpha_{\mathrm{tm}})$, the mass term simplifies to

$$\begin{aligned} m\bar{\boldsymbol{\psi}}\boldsymbol{\psi} &= m\cos(\alpha_{\mathrm{tm}})\bar{\boldsymbol{\chi}}\boldsymbol{\chi} + im\sin(\alpha_{\mathrm{tm}})\bar{\boldsymbol{\chi}}\gamma_5\tau_3\boldsymbol{\chi} \\ &\equiv m_0\bar{\boldsymbol{\chi}}\boldsymbol{\chi} + i\mu\bar{\boldsymbol{\chi}}\gamma_5\tau_3\boldsymbol{\chi}\,. \end{aligned} \tag{2.44}$$

The real phase α_{tm} is called "twist angle" and μ is called "twisted mass". The transformation is non-anomalous because $\mathrm{tr}\{\tau_3\}$ is traceless.

These modifications becomes relevant when the regulator like the Wilson Dirac matrix from Eq. (2.39) breaks chiral symmetry. In this case reverting the axial transformation transforms the regulator. Therefore the Wilson twisted mass action [43]

$$S_{\mathrm{F}}[\boldsymbol{\chi}, \bar{\boldsymbol{\chi}}, U] = a^4 \sum_{m,n\in\Lambda} \bar{\boldsymbol{\chi}}(n)\left(D_{\mathrm{W}}(n|m) + m_0 + \mathrm{i}\mu\gamma_5\tau_3\right)\boldsymbol{\chi}(m)\,. \tag{2.45}$$

is a different infrared regulator for QCD.

The main advantage of twisted mass appears at "maximal twist", that is $\alpha_{\mathrm{tm}} = \pi/2$. The dependence on a of the vacuum expectation value of any nonvanishing operator (this includes hadron masses) must at least by $\mathcal{O}\left(a^2\right)$ [44]!

The twisted action must obey the same symmetries as the original one, the transformation prescriptions become dependent on ω_A. The main disadvantage of twisted mass is that due to the non-trivial flavor structure introduced in the twisted mass term parity P and total isospin I are no longer good quantum numbers at maximal twist. In particular, states with all parameters identical but P or I may mix. This has been observed for the π^0 which has quantum number indistinguishable from the vacuum and therefore acquires a mass different to its charged partners [45]. One way to control this splitting is by performing a continuum extrapolation as with chiral

symmetry also isospin conservation will be restored.

This concludes our discussion of the discretized action. With the lattice action in place, we may now turn our attention to the the path integral introduced in Eq. (2.21).

2.2.2 Sampling of the path integral

For brevity, the path integral will be discussed for just a single flavor fermion field. The ideas carry over to twisted mass.

Even in discretized spacetime, the configuration space of the path integral samples is still large and an exact calculation is unfeasible. Nevertheless one may obtain an stochastic estimate for the path integral with Monte Carlo methods.

The first step is to perform a Wick rotation $t \to \mathrm{i}t^{\mathrm{E}}$ and therefore work with the Euclidean rather than the usual Minkowski metric. An immediate consequence is, that the phase factor in the path integral becomes real:

$$\exp(\mathrm{i}S_{\mathrm{QCD}}) \to \exp\Big(-S^{\mathrm{E}}_{\mathrm{QCD}}\Big)\,. \tag{2.46}$$

In the following we will throughout assume Euclidean spacetime and therefore drop any superscript E's.

We already mentioned that the integration over the fermion fields ψ and $\bar{\psi}$ may be separated from the rest of the path integral and performed analytically when introducing the Dirac matrix. To this end we rewrite the path integral Eq. (2.21)

$$\begin{aligned}
\langle\mathcal{O}\rangle &= \frac{1}{Z}\int \mathcal{D}\psi\ \mathcal{D}\bar{\psi}\ \mathcal{D}U\ \mathrm{e}^{-S_{\mathrm{QCD}}[\psi,\bar{\psi},U]}\ \mathcal{O}[\psi,\bar{\psi},U] \\
&= \frac{1}{Z}\int \mathcal{D}U\ \mathrm{e}^{-S_{\mathrm{G}}[U]}\int \mathcal{D}\psi\ \mathcal{D}\bar{\psi}\ \mathrm{e}^{-S_{\mathrm{F}}[\psi,\bar{\psi},U]}\ \mathcal{O}[\psi,\bar{\psi},U] \\
&= \frac{1}{Z}\int \mathcal{D}U\ \mathrm{e}^{-S_{\mathrm{G}}[U]}\ Z_F[U]\ \Big\langle\mathcal{O}[\psi,\bar{\psi},U]\Big\rangle_F
\end{aligned} \tag{2.47}$$

where we defined the fermionic partition function

$$Z_{\mathrm{F}} = \int \mathcal{D}\psi\ \mathcal{D}\bar{\psi}\mathrm{e}^{-S_{\mathrm{F}}[\psi,\bar{\psi},U]} \tag{2.48}$$

and the fermionic expectation value $\langle\ \rangle_F$ is the path integral over ψ and $\bar{\psi}$ Because the fermion fields may be represented as vector of Grassmann numbers we may rewrite the fermionic partition function with the Matthews-Salam formula

$$\int \mathrm{d}\eta_N\ \mathrm{d}\bar{\eta}_N \ldots \mathrm{d}\eta_1\ \mathrm{d}\bar{\eta}_1 \exp\left(\sum_{i,j=1}^{N}\bar{\eta}_i M_{ij}\eta_j\right) = \det(M) \tag{2.49}$$

with η denote the Grassmann numbers. Upon inserting $M = -a^4 D$ the exponent becomes the fermion action Eq. (2.35) and

$$Z_{\mathrm{F}} = -\det(D)\,. \tag{2.50}$$

The path integral Eq. (2.47) becomes

$$\langle \mathcal{O} \rangle = \frac{1}{Z} \int \mathcal{D}U \ \mathrm{e}^{-S_\mathrm{G}[U]} \ (-1)^{N_f} \prod_f \det(D_f[U]) \left\langle \mathcal{O}[\psi_1, \bar{\psi}_1, \ldots \psi_{N_f}, \bar{\psi}_{N_f}, U] \right\rangle_F \tag{2.51}$$

where a determinant appears for each of the N_f distinct flavors in $\mathcal{O}$. Because squares of Grassmann numbers vanish, every interpolating operator may be expressed by "n-point functions" $\left\langle \eta_{i_1} \bar{\eta}_{j_1} \ldots \eta_{i_n} \bar{\eta}_{j_n} \right\rangle_F$. These may be evaluated with Wick's theorem

$$\left\langle \eta_{i_1} \bar{\eta}_{j_1} \ldots \eta_{i_n} \bar{\eta}_{j_n} \right\rangle_F = \sum_{\sigma \in \mathrm{S}_n} \mathrm{sign}(\sigma) D^{-1}_{i_1 j_{\sigma(1)}} \ D^{-1}_{i_2 j_{\sigma(2)}} D^{-1}_{i_n j_{\sigma(n)}} \tag{2.52}$$

where S_n is the permution group with n elements. The inverse fermion matrix D^{-1} is the propagator. The concrete operators $\mathcal{O}$ used for the ρ channel in this work are constructed in Chap. 3. Consequently we defer the calculations to Sec. 4.1. Because the fermionic degrees of freedom are integrated out the only remaining dependence is on U.

Now, gauge field configurations for which the action becomes large are exponentially suppressed and we may reinterpret

$$P = Z^{-1} \exp(-S_\mathrm{G}[U]) \det(D_f[U]) \tag{2.53}$$

as a probability weight.

Rather than evenly sampling potentially strongly suppressed field configurations, it is far more efficient to sample from the distribution given by the action and give each the same weight [46]. When generating the sample configurations with a Markov chain algorithm such as Hybrid Monte Carlo [47] they are mathematically proven to approximate the target distribution and due to the central limit theorem the approximation error is systematically improvable by increasing the number of configurations.

Let N_conf by the number of such sample gauge field configurations generated with probabilty distribution P. The estimate of the expectation value is simply the arithmetic mean over the samples.

$$\begin{aligned} \langle O \rangle &\approx \frac{1}{N_\mathrm{conf}} \sum_{r=1}^{N_\mathrm{conf}} \langle O[U_r] \rangle_F \\ &= \frac{1}{N_\mathrm{conf}} \sum_{r=1}^{N_\mathrm{conf}} \sum_{\sigma \in \mathrm{S}_n} \mathrm{sign}(\sigma) \ D^{-1}_{i_1 j_{\sigma(1)}}[U_r] \ D^{-1}_{i_2 j_{\sigma(2)}}[U_r] \ D^{-1}_{i_n j_{\sigma(n)}}[U_r] \,. \end{aligned} \tag{2.54}$$

2.2.3 Resampling of gauge configurations

While Eq. (2.54) produces a value for the sample estimate, it does not make a statement about the sampling distribution. A common way to infer the standard error on the estimate is by resamling. In the boostrap method N_conf gauge configuration are drawn with replacement from the original set and their mean is taken. This procedure is repeated N_boot times until. These means obey the central limit theorem and therefore are gaussian distributed (provided the statistics is sufficient and the original distribution is not too pathological). Their standard

deviation estimates the standard error of the original sample estimate

$$\mathrm{SE}(\langle O \rangle) = \mathrm{SD}\left(\frac{1}{N_{\mathrm{conf}}} \sum_{r=1}^{N_{\mathrm{conf}}} \langle O[U_{b,r}] \rangle_F \right) \tag{2.55}$$

where $U_{b,r}$ is the r^{th} element of the b^{th} bootstrap sample.

One particular special case of the bootstrap is the jackknife method. Rather than emulated samples like the original one by randomly drawing, for $k < n$ all $\binom{N}{k}$ ways to choose a subset with $n - k$ elements are taken. In practice, almost always delete-1 jackknife is used. Historically the jackknife preceeds bootstrap as the computation is far less demanding. It also is more robust against outliers. The distribution of jackknife sample means is smaller than the bootstrap by a factor $n - 1$:

$$\mathrm{SE}(\langle O \rangle) = \sqrt{n-1}\ \mathrm{SD}\left(\frac{1}{N_{\mathrm{conf}} - 1} \sum_{r=1}^{N_{\mathrm{conf}}-1} \langle O[U_{j,r}] \rangle_F \right) \tag{2.56}$$

where this time $U_{j,r}$ is the r^{th} element of the j^{th} jackknife sample. The jackknife requires certain smoothness conditions to be fulfilled. It performs poorly compared to bootstrap if the estimated quantity is not smooth or highly non-linear.

If reversely the error of an observable is known, but not the underlying distribution the bootstrap may also be used to generate pseudosamples. Usually the distribution is assumed to be gaussian where the expectation value and standard deviation are the given central value and error. From this distribution N_{boot} values are drawn randomly and from there on they may be treated the same way bootstrap samples would be. This approach is called “parametric bootsrap”.

2.3 Scattering on the lattice

In Sec. 2.1 was established that scattering quantities by definition live in infinite volume Minkowski spacetime. The theoretical description of scattering via S-matrix formalism relies on asymptotic final and initial states and merely quantifies the transition between these.

We aim to describe the ρ resonance which to a very good approximation is only sensitive to the strong interactions. The currently accepted theory of strong interactions, Quantum Chromodynamic (QCD), is non-perturbative at the energy scale relevant here. In Sec. 2.2 we introduced Lattice QCD which, systematically improvable and from first principles, approximates the predictions of QCD. Unfortunately in order to sample the configuration space with Monte Carlo methods it require a transition to Euclidean space. This renders a direct extraction of scattering results in lattice QCD impossible [48].

Therefore an indirect aproach is taken. When two particles are confined to a finite volume their interaction shifts the spectrum. In contrast to asymptotic states, the spectrum can be measured in lattice QCD. Further details can be found in Sec. 2.6. By comparing the non-interacting spectrum i.e. the masses of the free particles to the shifted spectrum, the effect of the interaction can be measured in the form of energy shifts. These are related to infinite volume scattering properties by the Lüscher formula [17, 18]. While originally derived for two identical stable scalar particles in the rest frame, these limitations have largely been lifted by other authors. See e.g. [49–53] for the Lüscher method in a three particle systems and [19] for a review.

In this section we illustrate the key concepts of the Lüscher formula and in doing so introduce all the notation we need later on. We proceed by discussing the descent of symmetry to finite volumes and the consequences for the Lüscher method. It will turn out that in order to map out an energy region and extract the ρ width, a solid foundation in group theory as well as finite representation theory is required. We will discuss everything necessary to understand the "subduction" of continuum states to the lattice and close with the Lüscher formula for the lattice.

2.3.1 Derivation of the Lüscher formula

The following derivation is quantum mechanical for simplicity. The extension to field theory is rigorously established in Theorem 7.1 of [18]: "Up to terms which vanish exponentially at large L, the relationship between the scattering phases and the two-particle spectrum in finite volume is exactly the same as in quantun mechanics." Furthermore assume continuous spacetime. The discretization will be postponed to Sec. 2.3.4.

Consider two identical bosons of mass M in S-wave in a finite cube with periodic boundary conditions. This is the topology of a three-dimensional torus.

Assume a spherically symmetric interaction potential $V(r)$ that admits square-integrable solution of the Klein-Gordan equation. The only requirement is the potential to be negligible outside a finite range

$$V(r) \approx 0 \text{ for } r > R\,.$$

The extent of the cube has to be larger than R, so that there is an "exterior region" within the cube where the wave function does not feel the potential. In this exterior region the relevant equation of motion is the Helmholtz equation.

Now there is a one-to-one correspondence between wave functions in finite volume and the solutions of the Helmholtz equation in the exterior region. This correspondence yields a relation between scattering phase shift (from the wave functions) and the lattice energy levels (from the Helmholtz equation). To see this, we follow three steps:

1. Calculate wave functions via partial wave decomposition
2. Construct solutions of the Helmholtz equation
3. Compare the coefficients of both solutions

1. Calculation of wave functions

The wave functions are the eigenfunction of Hamilton operator. Because we assumed a spherically symmetric potential, angular momentum is a good quantum number and we may seperate any wave function into a radial and an angular part and decompose the later into a basis of spherical harmonics.

$$\psi(r,\theta,\phi) = \sum_{l=0}^{\infty} \sum_{m=-l}^{l} Y_{lm}(\theta,\phi)\psi_{lm}(r) \tag{2.57}$$

As usual, l denotes the angular momentum and m the magnetic quantum number. The radial part $\psi_{lm}(r)$ solves the radial differential equation whose principal solutions are the spherical

Bessel functions. Therefore $\psi_{lm}(r)$ may be decomposed as

$$\psi_{lm}(r) = b_{lm}\left(\alpha_l(k) j_l(kr) + \beta_l(k) n_l(kr)\right) . \tag{2.58}$$

where the scattering momentum k is related to the energy E of the interacting two-particle system by

$$k^2 \;=\; \frac{E^2}{4} - M^2 . \tag{2.59}$$

The coefficients $\alpha_l(k)$ and $\beta_l(k)$ are related to the scattering phase shift δ_l of the l-th partial wave

$$\mathrm{e}^{2\mathrm{i}\delta_l(k)} = \frac{\alpha_l(k) + \mathrm{i}\beta_l(k)}{\alpha_l(k) + \mathrm{i}\beta_l(k)} . \tag{2.60}$$

Solution of Helmholtz equation

The exterior region where the potential is negligible is given by the set

$$\Omega = \left\{ r \in \mathbb{R}^3 , \quad \forall\, \vec{n} \in \mathbb{Z}^3 : |\vec{r} + \vec{n}L| > R \right\} . \tag{2.61}$$

In the exterior region, $\psi(\boldsymbol{r})$ satisfies the Helmholtz equation

$$(\Delta + k^2)\psi(\boldsymbol{r}) = 0 \tag{2.62}$$

As long as k is not singular, a set of generalized Greens functions of the Helmholtz equation $G_{lm}(\boldsymbol{r}, k^2)$ form a basis for the set of its solutions.

For the calculation a formal partial wave cutoff Λ must be introduced, that will be taken to infinity in the end. The expansion of $\psi(r)$ neglecting partial waves $l \geq \Lambda$ is given by

$$\psi(\boldsymbol{r}) = \sum_{l=0}^{\Lambda} \sum_{m=-l}^{l} 4\pi(-1)^l v_{lm} G_{lm}(\boldsymbol{r}, k^2) \tag{2.63}$$

where v_{lm} are just some coefficients and the expansion of the Greens function into spherical harmonics leads to

$$G_{lm}(\vec{r}, k^2) = \frac{(-1)^l}{4\pi} k^{l+1} \cdot \left(Y_{lm}(\theta,\phi) n_l(kr) + \sum_{l'=0}^{\infty} \sum_{m'=-l'}^{l'} \mathcal{M}_{lm,l'm'} Y_{l'm'}(\theta,\phi) j_{l'}(kr) \right) \tag{2.64}$$

with the matrix elements of M given by

$$M_{lm,l'm'} = \frac{(-1)^l}{\pi^{3/2}} \sum_{j=|l-l'|}^{l+l'} \sum_{s=-j}^{j} \frac{i^l}{q^{j+1}} \mathcal{Z}_{js}(1; q^2)^* C_{lm,js,l'm'} , \quad q = \frac{L}{2\pi} \cdot k . \tag{2.65}$$

Here, $\mathcal{Z}_{lm}$ denotes the Lüscher Zeta-function

$$\mathcal{Z}_{lm}(s, q^2) = \sum_{\boldsymbol{n}\in\mathbb{Z}^3} \frac{\mathcal{Y}_{lm}(\vec{n})}{(\boldsymbol{n}^2 - q^2)^s} \tag{2.66}$$

with the harmonic polynomials

$$\mathcal{Y}_{lm}(r, \theta, \phi) = r^l Y_{lm}(\theta, \phi) \tag{2.67}$$

and $C_{lm,js,l'm'}$ may be expressed by Wigner $3j$-symbols

$$C_{lm,js,l'm'} = (-1)^{m'} i^{l-j+j'} \sqrt{(2l+1)(2j+1)(2l'+1)} \begin{pmatrix} l & j & l' \\ m & s & m' \end{pmatrix} \begin{pmatrix} l & j & l' \\ 0 & 0 & 0 \end{pmatrix} . \tag{2.68}$$

For certain values of k, $\psi(r)$ assumes a singularity. On the set of singular values

$$\mathcal{J} = \left\{ k \in \mathbb{R}\,, \quad \exists\, \vec{n} \in \mathbb{Z}^3 : k = \pm\frac{2\pi}{L}|\vec{n}| \right\} ,$$

plane waves also solve the equations of motion. The Green functions no longer are singular periodic solutions, but it is possible to construct modified Green functions with the same properties as before. They may again be expanded into spherical harmonics and an analog result may be found. However the physical relevance is questionable because the interaction typically only causes a slight deviation from the non-interacting energy levels and therefore obtaining an interacting energy levels that is in $\mathcal{J}$ is virtually impossible in a lattice simulation. Therefore in this work we only discuss the case where k is real and $k > 0$.

Lüscher formula

The expansions Eq. (2.58) and Eq. (2.64) both contain the Bessel functions. In order to fulfill the correspondence of solutions inside and outside the potential, the coefficients of both expansions must coincide.

$$b_{lm}\alpha_l(k) = \sum_{l'=0}^{\Lambda} \sum_{m=-l'}^{l'} v_{l'm'} \frac{(-1)^{l'}}{4\pi} k^{l'+1} M_{l'm',lm} \tag{2.69}$$

$$b_{lm}\beta_l(k) = v_{lm} \frac{(-1)^{l}}{4\pi} k^{l+1} \tag{2.70}$$

The coefficients v_{lm} may be eliminated and one finds that a solution to the resulting system of equations in angular momentum space exists if and only if the determinant vanishes. Reexpressing α_l and β_l by the phase shift δ_l with the help of Eq. (2.60) leads to the Lüscher formula

$$\det\Big(M_{lm,l'm'}(k) - \delta_{ll'}\delta_{mm'} \cot\delta_l(k)\Big) = 0\,. \tag{2.71}$$

Given an estimate for higher partial waves, the Lüscher formula provides the phase shift $\delta_l(k)$ for each scattering momentum k obtained on the lattice.

2.3.2 Moving reference frames

To meaningfully describe the functional form of the phase shift, a single point in the spectrum is not sufficient. Because the argument of the Lüscher Zeta function $\mathcal{Z}_{js}(1;q^2)$ is dependend on the spatial lattice size L, it is possible to obtain different values of k by using multiple lattice volumes. As this requires the generation of new gauge configurations for each volume, this approach is very costly and additionally control over finite size effects is lost. However applying a Lorentz boost to the operators changes the extracted energy values in the CM frame, similar to the effect a different volume would have. In this section we illustrate the modifications necessary to extend the Lüscher formula to moving reference frames [20, 22, 54]

However, the distinction of a particular direction as the CM momentum restricts the rotational symmetry group even further than it already was by the discretization.

Let $\boldsymbol{p}_{\mathrm{cm}}$ by the CM momentum. Due to the finite volume it is quantized as

$$\boldsymbol{p}_{\mathrm{cm}} = \frac{2\pi}{L} \cdot \boldsymbol{d}\,, \quad \boldsymbol{d} \in \mathbb{Z}^3 \tag{2.72}$$

and the relativistic energy W_{L} is given by the dispersion relation

$$W_{\mathrm{L}} = \sqrt{\boldsymbol{p}_{\mathrm{cm}}^2 + E_{\mathrm{CM}}^2}\,. \tag{2.73}$$

Until now we worked in the rest frame and therefore $E \equiv E_{\mathrm{CM}}$.

The energy Eq. (2.73) is only dependent on the absolute value, not the direction of $\boldsymbol{p}_{\mathrm{cm}}$. Therefore we denote each "momentum sector" by the corresponding integer value $d \equiv |\boldsymbol{d}|$ from Eq. (2.72). We discuss the relation between different representatives of the same momentum sector in Sec. 2.5

The derivation of the Lüscher formula (2.71) relied on an expansion of $\psi(r)$ in spherical harmonics. This is only meaningful if the angular momentum is a good quantum number i.e. in center-of-mass frame. Therefore a Lorentz boost must be applied. The boost factor is given by

$$\gamma \;=\; \frac{W_{\mathrm{L}}}{E_{\mathrm{CM}}} = \frac{W_{\mathrm{L}}}{\sqrt{W_{\mathrm{L}}^2 - \boldsymbol{p}_{\mathrm{cm}}^2}} \tag{2.74}$$

where E_{CM} was replaced with Eq. (2.73).

The boost expands space in direction $\boldsymbol{d}$ for an observer in the CM frame. The boundary conditions of the wave function $\psi(\boldsymbol{r})$ and the potential V become d-periodic and compared to Eq. (2.61) the exterior region

$$\Omega_{\mathrm{CM}} = \left\{ r \in \mathbb{R}^3\,, \quad \forall\, n \in \mathbb{Z}^3 : |\vec{r} - \vec{\gamma}\vec{n}L| > R \right\} \tag{2.75}$$

where $\psi(r)$ satisfies the Helmholtz equation becomes dependent on γ. However, the steps of the derivation in Sec. 2.3.1 are still valid. In the CM frame the wave function may still be calculated. The solution of the Helmholtz equation may be constructed in the basis of a set of generalized Greens function $G^{\boldsymbol{d}}(\vec{x}, p)$ and their derivatives which now depend on the CM momentum and

the expansion into spherical harmonics still works. Eq. (2.64) - (2.66) become

$$G^{\boldsymbol{d}}_{lm}(\vec{r},k^2) = \frac{(-1)^l}{4\pi}k^{l+1}\cdot\left(Y_{lm}(\theta,\phi)n_l(kr) + \sum_{l'=0}^{\infty}\sum_{m'=-l'}^{l'}\mathcal{M}^{\boldsymbol{d}}_{lm,l'm'}Y_{l'm'}(\theta,\phi)j_{l'}(kr)\right) \tag{2.76}$$

with the modified matrix elements $M^{\boldsymbol{d}}$ given by

$$M^{\boldsymbol{d}}_{lm,l'm'}(k) = \frac{(-1)^l\gamma^{-1}}{\pi^{3/2}}\sum_{j=|l-l'|}^{l+l'}\sum_{s=-j}^{j}\frac{i^l}{q^{j+1}}\mathcal{Z}^{\boldsymbol{d}}_{js}(1;q^2)^*C_{lm,js,l'm'}\,,\quad q=\frac{L}{2\pi}\cdot k\,. \tag{2.77}$$

and the generalized Lüscher Zeta-function

$$\mathcal{Z}^{\boldsymbol{d}}_{lm}(s,q^2) = \sum_{\vec{r}\in\mathbb{Z}^3_{\boldsymbol{d}}}\frac{\mathcal{Y}_{lm}(\boldsymbol{r})}{(\boldsymbol{r}^2-q^2)^s}\,. \tag{2.78}$$

Except for the additional γ in the matrix elements, the only difference is that the singular values of k and therefore poles of the Zeta-function appear dilated to an observer in the CM frame. The set $\mathbb{Z}^3_{\boldsymbol{d}}$ is defined as

$$\mathbb{Z}^3_{\boldsymbol{d}} = \left\{\,\boldsymbol{r}\in\mathbb{R}\,,\quad \exists\,\boldsymbol{z}\in\mathbb{Z}^3 : r=\gamma^{-1}\left(\boldsymbol{z}-\boldsymbol{d}/2\right)\right\}\,. \tag{2.79}$$

If $d=0$, $\gamma=1$ and our previous result is recovered.

Finally the dependence on $\boldsymbol{d}$ is encapsulated by introducing

$$w^{\boldsymbol{d}}_{js} = \frac{\mathcal{Z}^{\boldsymbol{d}}_{js}(1,q^2)}{\pi^{3/2}\sqrt{2j+1}\gamma q^{j+1}}\,,\qquad q=\frac{kL}{2\pi} \tag{2.80}$$

to express the matrix $M^{\boldsymbol{d}}$ as

$$M^{\boldsymbol{d}}_{lm,l'm'}(k) = (-1)^l\sum_{j=\left|l-l'\right|}^{l+l'}\sum_{s=-j}^{j}\sqrt{2j+1}\;i^j w^{\boldsymbol{d}}_{js}C_{lm,js,l'm'}\,. \tag{2.81}$$

2.3.3 Angular momentum on the Lattice

The lattice introduced in Eq. (2.25) is a four dimensional hypercube with identical edge lengths in spatial directions. Other geometries are possible [31] but tremendously complicate the following discussion.

In an infinte volume the rotational symmetry group is the special orthogonal group in three dimensions, SO(3). It has exactly one $2l+1$ dimensional irreducible representation ("irrep") for all $l\in\mathbb{N}$. Ascribing an angular momentum quantum number is equivalent to specifying the irreducible representation of SO(3) an eigenvector of the Hamiltonian transforms under. The magnetic quantum number $-l\leq m\leq l$ is used to label each of those $2l+1$ states. To describe fermions the symmetry considerations are more complicated[2] but for this work considering just

[2] Fermions have half-integer spin and therefore transform under an even-dimensional irrep. Mathematically this may be expressed by taking the double cover group $\mathrm{SO}(3)^{\mathrm{D}}\cong\mathrm{SU}(2)$. As the name implies double covering is a

the rotations in SO(3) is sufficient. The ρ is a boson and exclusively decays into bosons.

The symmetry group may be extended by including improper rotations: rotations followed by a subsequent inversion. This is needed because parity is no longer conserved in moving frames.[3] Improper rotations have determinant -1 and therefore the full isometries of spacetime are described by the orthogonal group O(3).

The rotational symmetry group of our lattice is restricted to the subset of rotations under which the lattice remains invariant. In the rest frame this is the symmetry group of a cube, the octahedral group O_h.[4] After a Lorentz boost, due to length contraction this cube will appear stretched in direction of the CM momentum $\boldsymbol{p}_{\mathrm{cm}}$ and unchanged in perpendicular directions to an observer in the rest frame. Therefore the restricted symmetry group must additionally conserve $\boldsymbol{p}_{\mathrm{cm}}$.

As already discussed in Sec. 2.3.2 $\boldsymbol{p}_{\mathrm{cm}}$ is quantized as

$$\boldsymbol{p}_{\mathrm{cm}} = \frac{2\pi}{L} \cdot \boldsymbol{d}\,, \quad \boldsymbol{d} \in \mathbb{Z}^3 \tag{2.72}$$

due to the finite volume. If two vectors have the same absolute value they are connected by an allowed lattice rotation from $\mathrm{O_h}$ and their symmetry groups are isomorphic. Furthermore, rotations preserve length and the prefactor $2\pi/L$ is irrelevant here. Therefore it suffices to characterize the groups by d^2.

In this work all momenta with $d^2 \leq 4$ are used. To simplify notation we introduce the "little group" $\mathrm{LG}(\boldsymbol{d})$ which will be explained further in Sec. 2.5. In addition to the group $\mathrm{O_h}$ for $\boldsymbol{d} = (0,0,0)$, the little groups are $\mathrm{C_{4v}}$ for all $\boldsymbol{d}$ with $d^2 = 1$ or 4, $\mathrm{C_{2v}}$ for $d^2 = 2$ and $\mathrm{C_{3v}}$ for $d^2 = 3$. For a detailed discussion of the groups relevant to this work we invite the reader to take a look at Sec. A.1. We follow the conventions in [55] and stick to the Schönflies notation [56] which nowadays is predominantly used in crystallography and molecular physics but has become the norm for lattice QCD as well.

Let L denote the l^{th} angular momentum irrep of O(3), $\mathrm{LG}(\boldsymbol{d})$ be one of the little groups and Γ be an irrep of $\mathrm{LG}(\boldsymbol{d})$. All lattice groups finite and as an immediate consequence of the great orthogonality theorem, so is the number of their irreps N_Γ. The mapping from denumerable angular momentum irreps of O(3) to a finite number of lattice irreps is surjective. Furthermore, it is not even a mapping because the existence of a $2l+1$-dimensional lattice irrep is not guaranteed and different m components of the same irrep L may be sent to different Γ. When that happens, the degeneracy of energy eigenvalues withing a multiplet is lifted and each Γ have their own energy levels which coalesce in the infinite volume limit. The decomposition of the lowest partial waves into the octahedral group [57–59] as well as the other groups [60, 61] is well established. We may write the decomposition as a direct product

$$\mathrm{L} \to \bigoplus_{i=1}^{N_\Gamma} n_i \Gamma_i\,, \qquad \sum_i n_i \cdot \dim(\Gamma_i) = 2l+1\,. \tag{2.82}$$

The factor n_i is called "multiplitiy". $n_i = 0$ means Γ_i does not appear in the decomposition of

one-to-two mapping and double cover groups have additional representations. For distinction the irreps of the simply connected group are called vector representations while the addtional irreps of the double cover group are named ray or projective representations.

[3] In principle the twisted mass term breaks parity even in the rest frame but this could be neglected.

[4] Because cubes and an octahedron are dual to each other, they share the same symmetry group and it was named after the latter

the l^{th} partial wave and $n_i > 1$ points to an accidental degeneracy of energy levels.

In the remainder of this section we follow [22, 54] and express the basis vectors of a lattice irrep Γ as a linear combination of L eigenstates $|\mathrm{L}, m\rangle$. This is called "subduction" and the linear coefficients which signify the m components exactly contributing to Γ are called "subduction coefficients".

Rotation of angular momentum states For all $g \in \mathrm{LG}(\boldsymbol{d})$ the corresponding rotation $R_g \in \mathrm{O}(3)$ is known. Because L is an irrep of O(3) the transformation of $|\mathrm{L}, m\rangle$ under the operator $\hat{R}_g$ is well defined:

$$\hat{R}_g \, |\mathrm{L}, m\rangle = \sum_{m'} \left|\mathrm{L}, m'\right\rangle \left\langle \mathrm{L}, m'\right| \hat{R}_g \left|\mathrm{L}, m\right\rangle = \sum_{m'} D^{\mathrm{L}}(R_g)_{m'm} \left|\mathrm{L}, m'\right\rangle . \tag{2.83}$$

In the last step we used that in a given basis $|\mathrm{L}, m\rangle$

$$\forall \; R \in \mathrm{O}(3) : D^{\mathrm{L}}_{m,m'}(R) = \left\langle \mathrm{L}, m'\right| \hat{R} \left|\mathrm{L}, m\right\rangle . \tag{2.84}$$

defines the matrix representation of L.

For proper rotations R the canonical coice are the Wigner D-matrices

$$D^{\mathrm{L}}(R) \equiv D^{\mathrm{L}}(\alpha, \beta, \gamma) \tag{2.85}$$

where we parametrized the rotation by the Euler angles α, β, γ.[5] For the spatial inversion i we use $D^{\mathrm{L}}_{m,m'}(i) = -1 \cdot \delta_{m,m'}$. The remaining improper rotations may by definition be written as a product of inversion and a proper rotation R. Because the representation preserves the group multiplication table, the matrices may be generated from the matrix product

$$D^{\mathrm{L}}(i \cdot R) = D^{\mathrm{L}}(i) \cdot D^{\mathrm{L}}(R) \equiv -D^{\mathrm{L}}(\alpha, \beta, \gamma) \, . \tag{2.86}$$

The matrix representations D^{Γ} of Γ is conceptually much simpler because there is only a finite number of matrices involved. As mentioned before we follow the conventions in [55] where complete lists for all the group elements may be found

Projection operator We use the projection method that was already applied in [32] to calculate the subduction coefficients. Let $\alpha, \beta \in \{\, 1, \ldots, \dim(\Gamma) \,\}$.[6] The operator

$$\hat{P}^{\Gamma}_{\alpha\beta}(\boldsymbol{d}) = \frac{\dim(\Gamma)}{|\mathrm{LG}(\boldsymbol{d})|} \sum_{g \in \mathrm{LG}(\boldsymbol{d})} D^{\Gamma}(g)^{*}_{\alpha\beta} \hat{R}_g \tag{2.87}$$

projects to a state that transforms like $|\Gamma, \alpha\rangle$. By summing over all m, the expression of $|\Gamma, \alpha\rangle$ as a linear combination of $|\mathrm{L}, m\rangle$ is achieved. The result will obviously be different for each momentum sector and the states still carry remembrance of the chosen L. Furthermore all linear combinations of such projected states share the transformation properties and therefore a sum

[5] Equivalently it can be expressed through a rotation axis $\boldsymbol{n}$ and an angle ϑ. This will lead to the same matrix elements. If one considers the double cover, the generalize will be easier because rotations with by angles largen than 2π are straightforward.

[6] not to be confused with the Euler angles

over different β and phases ϕ_m and ϕ_β may be used to obtain a complete and orthonormal basis labelled by α.

$$|\Gamma, \alpha, \mathrm{L}\rangle = \sum_\beta \phi_\beta \sum_m \phi_m \hat{P}^\Gamma_{\alpha\beta}(\boldsymbol{d}) \, |\mathrm{L}, m\rangle \tag{2.88}$$

$$= \sum_\beta \phi_\beta \sum_{m,m'} \phi_m \frac{\dim(\Gamma)}{|\mathrm{LG}(\boldsymbol{d})|} \sum_{g \in \mathrm{LG}(\boldsymbol{d})} D^\Gamma(R_g)^*_{\alpha\beta} \, D^\mathrm{L}(R_g)_{m'm} \, \Big| \, \mathrm{L}, m' \Big\rangle \, . \tag{2.89}$$

Because α was introduced as the row index of the matrix D^Γ, the basis vectors of Γ are called "rows". Choosing different columns β yields the same basis states, only with their order interchanged. Therefore in this work $\beta = 1$ and $\phi_\beta = \boldsymbol{e}_1$ was chosen throughout.

A more detailed discussion as well as proofs may be found in Sec. A.2. If the multiplicity of Γ is larger than 1, the projected basis state is not unique. Instead, the resulting set of states may also be orthonormalized by choosing different ϕ_m. and the projection yields a different basis states for each occurrence of Γ. Therefore the new basis must also be labelled by a multiplicity index n. The lattice basis expressed by angular momentum states is

$$|\Gamma, \alpha, \mathrm{L}, n\rangle = \sum_m s^{\Gamma,\alpha,n}_{\mathrm{L},m} \, |\mathrm{L}, m\rangle \, . \tag{2.90}$$

where $s^{\Gamma n}_\mathrm{L}$ is the final set of subduction coefficients with appropriately chosen phases.

2.3.4 Subduction of the Lüscher formula

In Sec. 2.3.1 and 2.3.2 we derived the Lüscher formula

$$\det\Big(M^{\boldsymbol{d}}_{lm,l'm'}(k) - \delta_{ll'}\delta_{mm'} \cot\delta_l(k)\Big) = 0 \tag{2.91}$$

with $M^{\boldsymbol{d}}$ given by (2.81) and the determinant acting in angular momentum space. Furthermore in Sec. 2.3.3 we established that angular momentum is no longer is a good quantum number on the lattice and its role is taken by the irreps of finite symmetry groups. This chapter concludes the discussion of scattering on the lattice by subducing the Lüscher formula into the basis given in Eq. (2.90). We assume the direction of $\boldsymbol{d}$ to be arbitrary but fixed. The relation between different representatives of the same momentum sector will be discussed in Sec. 2.5

In the new basis the matrix elements are

$$\Big\langle \Gamma, \alpha, \mathrm{L}, n \, \Big| \, \hat{M}^{\boldsymbol{d}} \, \Big| \, \Gamma', \alpha', \mathrm{L}', n' \Big\rangle = \sum_{m,m'} s^{\Gamma,\alpha,n^*}_{\mathrm{L},m} s^{\Gamma',\alpha',n'}_{\mathrm{L}',m'} \Big\langle \mathrm{L}, m \, \Big| \, \hat{M}^{\boldsymbol{d}} \, \Big| \, \mathrm{L}', m' \Big\rangle \tag{2.92}$$

$$= \sum_{m,m'} s^{\Gamma,\alpha,n^*}_{\mathrm{L},m} s^{\Gamma',\alpha',n'}_{\mathrm{L}',m'} M^{\boldsymbol{d}}_{lm,l'm'} \tag{2.93}$$

Furthermore Γ and α are still good quantum numbers and as a consequence of Schur's Lemma, the matrix is blockdiagonal

$$\Big\langle \Gamma, \alpha, \mathrm{L}, n \, \Big| \, \hat{M}^{\boldsymbol{d}} \, \Big| \, \Gamma, \alpha, \mathrm{L}', n' \Big\rangle = \delta_{\Gamma\Gamma'}\delta_{\alpha\alpha'} \Big\langle \Gamma, \alpha, \mathrm{L}, n \, \Big| \, \hat{M}^{\boldsymbol{d}} \, \Big| \, \Gamma, \alpha, \mathrm{L}', n' \Big\rangle \equiv M^{\boldsymbol{d},\Gamma,\alpha}_{ln,l'n'} \tag{2.94}$$

where we defined $M^{\boldsymbol{d},\Gamma,\alpha}$ as the nontrivial block that belongs to Γ.

Upon inverting Eq. (2.94) one finds

$$M^{\boldsymbol{d},\Gamma,\alpha}_{ln,l'n'}(k) = \delta_{\Gamma\Gamma'}\delta_{\alpha\alpha'} \sum_{m,m'} s^{\Gamma,\alpha,n*}_{\mathrm{L},m} s^{\Gamma,\alpha,n'}_{\mathrm{L}',m'} M^{\boldsymbol{d}}_{lm,l'm'}(k) \tag{2.95}$$

$$= \sum_{m,m'} s^{\Gamma,\alpha,n*}_{\mathrm{L},m} s^{\Gamma,\alpha,n'}_{\mathrm{L}',m'} (-1)^{l} \sum_{j=\left|l-l'\right|}^{l+l'} \sum_{s=-j}^{j} \sqrt{2j+1}\; i^{j} w^{\boldsymbol{d}}_{js}(k) C_{lm,js,l'm'}\,. \tag{2.96}$$

and Lüscher formula remains unchanged except for the space it acts in

$$\det\left(M^{\boldsymbol{d},\Gamma,\alpha}_{ln,l'n'}(k) - \delta_{ll'}\delta_{nn'}\cot\delta_l(k)\right) = 0 \tag{2.97}$$

2.4 Angular momentum basis in moving frames

So far the only states with momenta were basis vectors of moving reference frames with momentum $\boldsymbol{p}_{\mathrm{cm}}$. The rotations that make up the projection operator in Eq. (2.87) are all the elements of $\mathrm{LG}(\boldsymbol{p}_{\mathrm{cm}})$ which, as we repeatedly used already, leave the boost vector unchanged. Therefore a last subtlety that could be ignored so far are nontrivial rotations of states with momenta.

In continuous and infinite spacetime the full spatial symmetry group the subgroup

$$\mathcal{T}^3 \rtimes \mathrm{O}(3) \tag{2.98}$$

of the Poincaré group.[60]. It is the semidirect product of the abelian Lie group of translations $\mathcal{T}^3$ and the rotation-reflection group O(3) already discussed above. The irreps of $\mathcal{T}^3$ may be labelled by three-dimensional wave number vectors $\boldsymbol{p}$ [62]. The eigenstates $|\mathrm{L}, m\rangle$ generalize to

$$|\boldsymbol{p}; \mathrm{L}, m\rangle \equiv |\boldsymbol{p}\rangle \otimes |\mathrm{L}, m\rangle \tag{2.99}$$

but this new states are variant under the action of O(3). Let $R \in \mathrm{O}(3)$:

$$\begin{aligned} \hat{R}\,|\boldsymbol{p}; \mathrm{L}, m\rangle &= \hat{R}\,|\boldsymbol{p}\rangle \otimes \hat{R}\,|\mathrm{L}, m\rangle \\ &= \left|\hat{R}\,\boldsymbol{p}\right\rangle \otimes \sum_{m'} D^{\mathrm{L}}(R)_{m'm} \left|\mathrm{L}, m'\right\rangle \\ &= \sum_{m'} D^{\mathrm{L}}(R)_{m'm} \left|\hat{R}\,\boldsymbol{p}; \mathrm{L}, m'\right\rangle \end{aligned} \tag{2.100}$$

where we used Eq. (2.83) for $\hat{R}\,|\mathrm{L}, m\rangle$.

On the lattice defined in Eq. (2.25) $\mathcal{T}^3$ must respect the boundary conditions and is therefore restricted to translations by aL. The remaining irreps are given by those wave number vectors whose components may be written as an integer multiple of $2\pi/L$ [63, 64] and there eigenstates are

$$|\boldsymbol{p}\rangle\ , \quad \boldsymbol{p} = \frac{2\pi}{L} \cdot \boldsymbol{d}\,, \quad \boldsymbol{d} \in \mathbb{Z}^3 \tag{2.101}$$

This is the origin of the quantization condition Eq. (2.72).

The states for an irrep Γ of $\mathrm{LG}(\boldsymbol{p}_{\mathrm{cm}})$ were labelled by α and therefore the lattice version of

Eq. (2.99) is

$$|\boldsymbol{p};\Gamma,\alpha\rangle \equiv |\boldsymbol{p}\rangle \otimes |\Gamma,\alpha\rangle \ . \tag{2.102}$$

In analogy to Eq. (2.100), the effect of a rotation R_g

$$\hat{R}_g\,|\boldsymbol{p};\Gamma,\alpha\rangle = \sum_{\alpha'} D^{\Gamma}(R_g)_{\alpha'\alpha}\ \left|\hat{R}\,\boldsymbol{p};\Gamma,\alpha'\right\rangle \ . \tag{2.103}$$

is nontrivial as $\boldsymbol{p}$ may change. It is crucial that $D^{\Gamma}(R_g)$ and therefore $\hat{R}_g\,|\boldsymbol{p};\Gamma,\alpha\rangle$ are only well defined for $g \in \mathrm{LG}(\boldsymbol{p}_{\mathrm{cm}})$.

2.5 The relation between equivalent moving frames

The Lüscher formula Eq. (2.97) depends on the CM momentum but as already discussed in Eq. (2.73) the energy levels and therefore k do not. Likewise, α still is a good quantum number on the lattice and therefore the energy levels of Γ are degenerate. The values $\delta_l(k)$ from different $\boldsymbol{d}$ and α will be identical up to statistical fluctuations. However the determination of k suffers from large systematic errors that are alleviated with larger statistics as we will discuss in Sec. 6.2. Compared to calculating $\delta_l(k)$ for all directions and rows, calculating only one energy level per irrep by averaging over equivalent $\boldsymbol{d}$ and α and only applying the Lüscher formula once is more robust. To achieve this, the basis states must be distinguished by $\boldsymbol{p}_{\mathrm{cm}}$ and the effect of the projector Eq. (2.87) must be revised.

As mentioned before, if two boosts have the same absolute value they are connected by an allowed lattice rotation from $\mathrm{O_h}$ and their symmetry groups are isomorphic. Let $\boldsymbol{p}_{\mathrm{cm}}$ be a boost the obeys the quantization condition Eq. (2.72). We call the set of all allowed boosts with the same absolute value "momentum sector" and denote it by

$$\{\,\boldsymbol{p}_{\mathrm{cm}}\,\} :- \left\{\,\boldsymbol{p}\in\mathbb{R}^3\,,\quad \exists\,\boldsymbol{d}\in\mathbb{Z}^3 : |2\pi/L\cdot\boldsymbol{d}| = |\boldsymbol{p}|\,\right\}\,. \tag{2.104}$$

The restricted subgroups of O(3) have already been discussed in Sec. 2.3.3 and A.1. Depending on the boost $\boldsymbol{p}$ these are the little groups

$$\mathrm{LG}(\boldsymbol{p}) :- \{\,g\in \mathrm{O_h} \mid \hat{R}_g\,\boldsymbol{p} = \boldsymbol{p}\,\} \tag{2.105}$$

comprised of all rotations in the octohedral group which leave $\boldsymbol{p}$ invariant. Even though for all $\boldsymbol{p}\in\{\,\boldsymbol{p}_{\mathrm{cm}}\,\}$ the little groups $\mathrm{LG}(\boldsymbol{p})$ are isomorphic, they consist of physically different rotations. The existence of an isomorphism is not enough to identify the elements that share the same representation matrix. Constructing the mapping is crucial to ensure the projection operators from Eq. (2.87) are consistent.

In this section the relation between different little groups will be put on a firmer ground by discussing them from a more formal perspective. The orbit stabilizer theorem will provide another valuable point of view. On that basis the mapping between different little groups is constructed and lastly the connection between different moving frames will be discussed.

2.5.1 The Orbit stabilizer theorem

Informally, the orbit stabilizer theorem states that the octahedral groups partitions into a set of elements for each boost direction and the partition is given by the left cosets a little group in $\mathrm{O_h}$. In this section we will discuss the practical consequences of this statement as well as fix consistent coset representatives that will be used throughout this work. The definitions and proofs are adopted from [65].

In Eq. (2.105) the action of a group element $g \in \mathrm{O_h}$ on $\boldsymbol{p} \in \{\, \boldsymbol{p}_{\mathrm{cm}} \,\}$ was already implicitly defined by the mapping

$$g \cdot \boldsymbol{p} :- \hat{R}_g \, \boldsymbol{p} \tag{2.106}$$

and little group is just another name for the stabilizer of G with respect to $\boldsymbol{p}$.

The orbit of $\boldsymbol{p}_{\mathrm{cm}}$ is defined as the image

$$\mathrm{O_h}(\boldsymbol{p}_{\mathrm{cm}}) :- \mathrm{O_h} \cdot \boldsymbol{p}_{\mathrm{cm}} = \{\, \boldsymbol{p}\,, \quad \exists\, \mathrm{g} \in \mathrm{O_h} : g\, \boldsymbol{p}_{\mathrm{cm}} = \boldsymbol{p} \,\} \tag{2.107}$$

of Eq. (2.106). This is precisely the momentum sector $\{\, \boldsymbol{p}_{\mathrm{cm}} \,\}$ defined by Eq. (2.104). Furthermore the first isomorphism theorem states, that the coimage of this mapping is canonically isomorphic to the orbit. It is given by

$$\mathrm{O_h}/\mathrm{LG}(\boldsymbol{p}_{\mathrm{cm}}) \tag{2.108}$$

which is the set of all left cosets $\{\, g\ \mathrm{LG}(\boldsymbol{p}_{\mathrm{cm}})\,, \mathrm{g} \in \mathrm{O_h} \,\}$ of $\mathrm{LG}(\boldsymbol{p}_{\mathrm{cm}})$ in $\mathrm{O_h}$. More formally the orbit stabilizer theorem states that the concrete bijection between the orbit and the left cosets of the stabilizer is given by

$$g \cdot \boldsymbol{p}_{\mathrm{cm}} \leftrightarrow g\mathrm{LG}(\boldsymbol{p}_{\mathrm{cm}})\,. \tag{2.109}$$

The use for this mapping is best illustrated by two examples:

1. If g in Eq. (2.109) is the identitiy element, the mapping becomes

$$\boldsymbol{p}_{\mathrm{cm}} \leftrightarrow \mathrm{LG}(\boldsymbol{p}_{\mathrm{cm}})\,. \tag{2.110}$$

For $\boldsymbol{p}_{\mathrm{cm}}$ the orbit stabilizer theorem just yields the little group of $\boldsymbol{p}_{\mathrm{cm}}$. This is how the little group was originally introduced in Sec. 2.3.3 and therefore an important affirmation.

2. Let $\tilde{g} \in \mathrm{O_h} : \tilde{\boldsymbol{p}} = \tilde{g} \cdot \boldsymbol{p}_{\mathrm{cm}}$ Then Eq. (2.109) becomes

$$\tilde{\boldsymbol{p}} \leftrightarrow \tilde{g}\ \mathrm{LG}(\boldsymbol{p}_{\mathrm{cm}})\,. \tag{2.111}$$

By definition $\boldsymbol{p}_{\mathrm{cm}}$ is invariant under its stabilizer. Therefore $\forall g \in \mathrm{LG}(\boldsymbol{p}_{\mathrm{cm}}) : \tilde{g}g\boldsymbol{p}_{\mathrm{cm}} = \tilde{g}\boldsymbol{p}_{\mathrm{cm}} = \tilde{\boldsymbol{p}}$. Because $\mathrm{LG}(\boldsymbol{p}_{\mathrm{cm}})$ forms a group it contains the identity and $\tilde{g} \in \tilde{g}\ \mathrm{LG}(\boldsymbol{p}_{\mathrm{cm}})$. In fact, the coset of $\mathrm{LG}(\boldsymbol{p}_{\mathrm{cm}})$ in $\mathrm{O_h}$ with respect to $\tilde{g}$ are exactly all elements of $\mathrm{O_h}$ which transform $\boldsymbol{p}_{\mathrm{cm}}$ to $\tilde{\boldsymbol{p}}$. This means, that the decomposition into physically distinct momentum directions is mathematically reflected by the decomposition into (by definition disjoint) cosets.

As the result is the same for all elements of the coset. Therefore it suffices to choose one $\boldsymbol{p}_{\mathrm{cm}}$ for each momentum sector and one coset representative $\tilde{g}$ for each $\boldsymbol{p} \in \{\, \boldsymbol{p}_{\mathrm{cm}} \,\}$. For the sake of

LG($\boldsymbol{p}_{\mathrm{cm}}$)	$\boldsymbol{d}_{\mathrm{cm}}$	$\tilde{g}$	$\tilde{\boldsymbol{d}}$	α	β	γ	i
O_h	$(0,0,0)$	E	$(0,0,0)$	0	0	0	1
C_{4v}	$(0,0,1)$	E	$(0,0,1)$	0	0	0	1
		C4x+	$(0,1,0)$	$-\pi/2$	$\pi/2$	$\pi/2$	1
		C4y−	$(1,0,0)$	π	$\pi/2$	π	1
		i	$(0,0,-1)$	0	0	0	−1
		C4x−	$(0,-1,0)$	$\pi/2$	$\pi/2$	$-\pi/2$	1
		C4y+	$(-1,0,0)$	0	$\pi/2$	0	1
C_{2v}	$(1,1,0)$	E	$(1,1,0)$	0	0	0	1
		σ_{y}	$(1,-1,0)$	0	π	0	−1
		σ_{x}	$(-1,1,0)$	0	π	π	−1
		C2b‘	$(-1,-1,0)$	0	π	$-\pi/2$	1
		σ_{d6}	$(1,0,1)$	$-\pi/2$	$\pi/2$	$-\pi/2$	−1
		σ_{d4}	$(1,0,-1)$	$\pi/2$	$\pi/2$	$\pi/2$	−1
		C2d‘	$(-1,0,1)$	$\pi/2$	$\pi/2$	$\pi/2$	1
		C2f‘	$(-1,0,-1)$	$-\pi/2$	$\pi/2$	$-\pi/2$	1
		σ_{d5}	$(0,1,1)$	π	$\pi/2$	0	−1
		σ_{d3}	$(0,1,-1)$	0	$\pi/2$	π	−1
		C2c‘	$(0,-1,1)$	0	$\pi/2$	π	1
		C2e‘	$(0,-1,-1)$	π	$\pi/2$	0	1
C_{3v}	$(1,1,1)$	E	$(1,1,1)$	0	0	0	1
		σ_{z}	$(1,1.-1)$	0	0	π	−1
		σ_{y}	$(1,-1,1)$	0	π	0	−1
		σ_{x}	$(-1,1,1)$	0	π	π	−1
		σ_{d4}	$(1,-1,-1)$	$\pi/2$	$\pi/2$	$\pi/2$	−1
		σ_{d3}	$(-1,1,-1)$	0	$\pi/2$	π	−1
		σ_{d1}	$(-1,-1,1)$	0	π	$\pi/2$	−1
		i	$(-1,-1,-1)$	0	0	0	−1
C_{4v}	$(0,0,2)$	E	$(0,0,2)$	0	0	0	1
		C4x+	$(0,2,0)$	$-\pi/2$	$\pi/2$	$\pi/2$	1
		C4y−	$(2,0,0)$	π	$\pi/2$	π	1
		i	$(0,0,-2)$	0	0	0	−1
		C4x−	$(0,-2,0)$	$\pi/2$	$\pi/2$	$-\pi/2$	1
		C4y+	$(-2,0,0)$	0	$\pi/2$	0	1

Table 2.1: Choice of reference vectors for the little groups and rotations chosen to relate reference frames to all equivalent moving frames. The physical rotoflections are identified by the Euler angles α, β, γ of the rotation part and the sign i under reflection.

notation we again drop the constant factors $2\pi/L$ by defining

$$\boldsymbol{d}_{\mathrm{cm}} = \frac{L}{2\pi}\boldsymbol{p}_{\mathrm{cm}} \qquad \tilde{\boldsymbol{d}} = \frac{L}{2\pi}\tilde{\boldsymbol{p}}\,. \tag{2.112}$$

A complete list of our choices is given in Tab. 2.1.

2.5.2 Conjugation of little groups

Let again $\tilde{g} \in \mathrm{O_h} : \tilde{\boldsymbol{p}} = \tilde{g} \cdot \boldsymbol{p}_{\mathrm{cm}}$ be a coset representative. Furthermore let $g' \in \mathrm{LG}(\tilde{\boldsymbol{p}})$.[7] By definition $g' \cdot (\tilde{g} \cdot \boldsymbol{p}_{\mathrm{cm}}) = g' \cdot \tilde{\boldsymbol{p}} = \tilde{\boldsymbol{p}} = \tilde{g} \cdot \boldsymbol{p}_{\mathrm{cm}}$. Applying $\tilde{g}^{-1}$ to both sides of this equation yields $(\tilde{g}^{-1} g' \tilde{g}) \cdot \boldsymbol{p}_{\mathrm{cm}} = \boldsymbol{p}_{\mathrm{cm}}$ and therefore

$$\tilde{g}^{-1} g' \tilde{g} \in \mathrm{LG}(\boldsymbol{p}_{\mathrm{cm}})\,. \tag{2.113}$$

Analogously one also finds

$$\tilde{g} g \tilde{g}^{-1} \in \mathrm{LG}(\tilde{\boldsymbol{p}}) \tag{2.114}$$

for $g \in \mathrm{LG}(\boldsymbol{p}_{\mathrm{cm}})$. The stabilizers of different elements in the orbit are conjugate to each other.

The group element in Eq. (2.114) is known as adjoint representation

$$\mathrm{Ad}_{\tilde{g}}(g) :- \tilde{g} g \tilde{g}^{-1} \tag{2.115}$$

Eq. (2.115) defines the mapping by which the consistent selection of physical rotations for each $\boldsymbol{p} \in \{\, \boldsymbol{p}_{\mathrm{cm}} \,\}$ is ensured.

Let Γ be an irreducible representation of $\mathrm{LG}(\boldsymbol{p}_{\mathrm{cm}})$. If $\tilde{\boldsymbol{p}} \in \{\, \boldsymbol{p}_{\mathrm{cm}} \,\}$, $\mathrm{LG}(\boldsymbol{p}_{\mathrm{cm}}) \cong \mathrm{LG}(\tilde{\boldsymbol{p}})$ and therefore Γ is also an irrep of $\mathrm{LG}(\tilde{\boldsymbol{p}})$. Let $g \in \mathrm{LG}(\tilde{\boldsymbol{p}})$. The representation matrix of g may be defined by

$$D^{\Gamma}(g) = D^{\Gamma}(\mathrm{Ad}_{\tilde{g}}(g))\,. \tag{2.116}$$

By specify the matrix representation of D^{Γ} for the elements of $\mathrm{LG}(\boldsymbol{p}_{\mathrm{cm}})$ it is specified for all congruent little group equivalent little groups as well. The identification of elements from different groups is fixed by the choice of coset representatives.

2.5.3 Projection operator

In Sec.2.3.3 we defined the projection operator

$$\hat{P}^{\Gamma}_{\alpha\beta}(\boldsymbol{d}) = \frac{\dim(\Gamma)}{|\mathrm{LG}(\boldsymbol{d})|} \sum_{g \in \mathrm{LG}(\boldsymbol{d})} D^{\Gamma}(g)^{*}_{\alpha\beta} \hat{R}_g \tag{2.87}$$

where like in Eq. (2.112) $\boldsymbol{d}$ is again connected to the elements of $\{\, \boldsymbol{p}_{\mathrm{cm}} \,\}$ via an irrelevant factor $2\pi/L$. In order to consistently define $\hat{P}^{\Gamma}_{\alpha\beta}(\boldsymbol{d})$ the elements $g \in \mathrm{LG}(\boldsymbol{d})$ must be related for all equivalent directions. With the results from Sec. 2.5.1 and 2.5.2 this is straightforward as the

[7] The little group, not the coset!

needed relation is just the adjoint representation Eq. (2.115). The projection operator becomes

$$\begin{aligned}\hat{P}^{\Gamma}_{\alpha\beta}(\boldsymbol{d}) &= \frac{\dim(\Gamma)}{|\mathrm{LG}(\boldsymbol{d}_{\mathrm{cm}})|}\sum_{g\in\mathrm{LG}(\boldsymbol{d}_{\mathrm{cm}})} D^{\Gamma}(\mathrm{Ad}_{\tilde{g}}(g))^{*}_{\alpha\beta}\hat{R}_{\mathrm{Ad}_{\tilde{g}}(g)} \\ &= \frac{\dim(\Gamma)}{|\mathrm{LG}(\boldsymbol{d}_{\mathrm{cm}})|}\sum_{g\in\mathrm{LG}(\boldsymbol{d}_{\mathrm{cm}})} D^{\Gamma}(g)^{*}_{\alpha\beta}\hat{R}_{\mathrm{Ad}_{\tilde{g}}(g)} \end{aligned} \tag{2.117}$$

where in the last step Eq. (2.116) was used to simplify D^{Γ}. $\boldsymbol{d}_{\mathrm{cm}}$ and $\tilde{g}$ are fixed in defined in Tab. 2.1 by the condition $\boldsymbol{d} = \tilde{g}\cdot\boldsymbol{d}_{\mathrm{cm}}$.

2.6 Extraction of Energy Levels

The final missing link is how to obtain the energy levels k that enter the Lüscher formula Eq. (2.97). The "correlation function"

$$\mathcal{C}(t) = \left\langle \mathcal{O}_{\mathrm{si}}(t)\mathcal{O}^{\dagger}_{\mathrm{so}}(0)\right\rangle , \tag{2.118}$$

in euclidean time serves this purpose. It describes the vacuum expectation value for creating a state at (source) time 0 and annihilating it at (sink) time t. An immediate consequence is that Eq. (2.54) applies, that is it can by estimated with Markov chain algorithms. Furthermore by a simply inserting of a complete set of states and using the time evolution operator one finds

$$\mathcal{C}(t) = \sum_{k} \langle 0|\mathcal{O}_{\mathrm{si}}(0)|k\rangle\ \langle k|\mathcal{O}^{\dagger}_{\mathrm{so}}(0)|0\rangle\, \mathrm{e}^{-tE_k} . \tag{2.119}$$

where E_k is the energy of the k^{th} state in the spectrum. In the limit of large time seperations, the correlation function relaxes into an exponential function of the ground state energy

$$\mathcal{C}(t) \propto \mathrm{e}^{-tE_0}\ \left(1+\mathcal{O}\left(\mathrm{e}^{-t(E_1-E_0)}\right)\right) . \tag{2.120}$$

The contributions from higher states are suppressed by their energy's difference to the ground state. This allows to extract E_0 directly from the correlation function. As the states k are created and annihilated by the operators $\vec{\mathcal{O}}_{si}, \mathcal{O}^{\dagger}_{\mathrm{so}}$, the only states that appear in Eq. (2.119) are those with non-zero overlap to both operators. In reversal this means the ground state energy of a certain channel may be calculated by choosing appropriate operators.

If one is interested in excited states in addition to E_0, they can be extracted from a $N\times N$ correlator matrix

$$\mathcal{C}(t) = \left\langle \vec{\mathcal{O}}(t)\ \vec{\mathcal{O}}^{\dagger}(0)\right\rangle . \tag{2.121}$$

where the N components of $\vec{\mathcal{O}}$ are different operators that couple to a common set of states. With the standard variational method [66, 67], the eigenvalues $\lambda_k(t,t_0)$ of this correlator matrix may be calculated. Here, t_0 is a parameter of the method and will be referred to as "reference time". Very similar to Eq. (2.120) the eigenvalues approach [67]

$$\lambda_k(t,t_0)\ \propto \exp(-E_k(t-t_0)) + \exp(-E_k(T-t+t_0)) + \mathcal{O}(e^{-t(E_k-E_{N+1})})\,. \tag{2.122}$$

when t becomes large enough. While the correction to Eq. (2.120) was dependent on the energy difference to the first excited state, in Eq. (2.122) it becomes is the energy difference to the first state not resolved by the correlation matrix. As this is generally larger, solving a generalized eigenvalue problem (GEVP) not only yields multiple energy levels, but also increases the precision of all but the highest extracted level. For a detailed discussion see Ref. [68].

For the Lüscher formula in moving frames operators that interpolate to the states $|\boldsymbol{p}, \Gamma, \alpha\rangle$ introduced in Sec. 2.4 are required. The explicit construction for the ρ resonance is one main result of this thesis and the topic of section 3. For the moment we assume they have already been found and denote the set by $\vec{\mathcal{O}}^{\alpha}_{\Gamma}(\boldsymbol{p})$.

Let Γ, Γ' be irreps of $\mathrm{LG}(\boldsymbol{p})$ $1 \leq \alpha \leq \dim(\Gamma)$, $\leq \alpha' \leq \dim(\Gamma')$ two of their rows. Because both operators belong to the same group, the correlation function can be shown to behave like

$$\left\langle \mathcal{O}^{\alpha}_{\Gamma}(t, \boldsymbol{p})\, \mathcal{O}^{\alpha'}_{\Gamma'}(0, \boldsymbol{p})^{\dagger} \right\rangle = \frac{1}{\dim(\Gamma)} \delta_{\Gamma\Gamma'} \delta_{\alpha\alpha'} \sum_{\beta,\beta'} \delta_{\beta\beta'} \left\langle \mathcal{O}^{\beta}_{\Gamma}(\boldsymbol{p})\, \mathcal{O}^{\beta'}_{\Gamma'}(\boldsymbol{p})^{\dagger} \right\rangle \tag{2.123}$$

as a consequence of the great orthogonality theorem. Eq. (2.123) states that the correlation function vanishes unless both operators interpolate to the same irrep and row.

Further on it must yield the same value for all rows of Γ. This proofs the statement claimed in Sec. 2.5: The energies extracted from different quantized momenta $\boldsymbol{p}$ of the same momentum sector $\boldsymbol{d}^2$ and rows α of the same irrep Γ are identical up to statistical fluctuations. By already averaging the correlation functions, the susceptibility to statistical noise is reduced. We denote the averaged correlation function by

$$\mathcal{C}_{\Gamma,\boldsymbol{d}^2}(t) \;=\; \frac{1}{|\{\, \boldsymbol{p}_{\mathrm{cm}} \,\}|} \sum_{\boldsymbol{p} \in \{\, \boldsymbol{p}_{\mathrm{cm}} \,\}} \frac{1}{\dim(\Gamma)} \sum_{\alpha=1}^{\dim(\Gamma)} \left\langle \vec{\mathcal{O}}^{\alpha}_{\Gamma}(t, \mathbf{p}) \cdot \vec{\mathcal{O}}^{\alpha}_{\Gamma}(0, \mathbf{p})^{\dagger} \right\rangle . \tag{2.124}$$

CHAPTER 3

Operators for the ρ meson

3.1 The Rho meson

The ρ meson was first measured in [10, 11] and confirmed in [12–14, 69]. A nice summary of the experimental work leading to its discovery is given in [70]. The measurement has since been repeated at ever higher accuracy. In particular [71] tabulates recorded bin data for phase shifts.

It is an vector isovector, i.e. it has quantum numbers

$$I^G J^{PC} = 1^+ 1^{--} \tag{3.1}$$

the ρ decays almost exclusively ($\sim 100\%$) into $\pi\pi$ [38]. In most experiments the favored mechanism was one-pion exchange appearing in $\pi\mathrm{N} \to \pi\pi\mathrm{N}$ [10–14] or $\pi p \to \pi\pi\Delta$ [71] with low momentum transfer to the nucleon / Δ particle. This is enforced by a small-t cut, usually around $3M_\pi$.

As a infrared and collinear safe definition of jets is chronically difficult, the most precise measurements today stem from e^+e^- annihilation and τ decays. The current PDG average [72] for the rho mass and width are

$$M_\rho = 775.26(25)\,\mathrm{MeV} \tag{3.2}$$

$$\Gamma_\rho = 149.1(8)\,\mathrm{MeV}\,. \tag{3.3}$$

At this level of accuracy even effects from isospin violation and $\rho - \gamma$ mixing must be taken into account [73]. As these effects are not mediated by the strong forces, this level of precision cannot be expected from a lattice QCD simulation where all other forces are neglected.

We are going to study the decay $\rho^0 \to \pi^+\pi^-$. The decay $\rho^0 \to \pi^0\pi^0$ is forbidden because two neutral pions cannot be coupled to p-wave. This may be inferred from bose symmetry or by the fact that the Clebsch–Gordan coefficient for $|1,0\rangle_I \otimes |1,0\rangle_I \to |1,0\rangle_I$ is zero.

On the lattice angular momentum is no longer a good quantum number and instead degeneracies are governed by the irreps Γ of little groups $\mathrm{LG}(\boldsymbol{d})$ which depend on the boost direction $\boldsymbol{d}$.

The decomposition of irrep L of the continuum rotation group O(3) may formally be expressed

$\boldsymbol{d}^2$	$\mathrm{LG}(\boldsymbol{d}_{\mathrm{cm}})$	$\mathrm{L}=0$	$\mathrm{L}=1$	$\mathrm{L}=2$
0	$\mathrm{O_h}$	$\mathrm{A_{1g}}$	$\mathrm{T_{1u}}$	$\mathrm{T_{2g}} \oplus \mathrm{E_g}$
1	$\mathrm{C_{4v}}$	$\mathrm{A_1}$	$\mathrm{A_1} \oplus \mathrm{E}$	$\mathrm{A_1} \oplus \mathrm{B_1} \oplus \mathrm{B_2} \oplus \mathrm{E}$
2	$\mathrm{C_{2v}}$	$\mathrm{A_1}$	$\mathrm{A_1} \oplus \mathrm{B_1} \oplus \mathrm{B_2}$	$2\mathrm{A_1} \oplus \mathrm{A_2} \oplus \mathrm{B_1} \oplus \mathrm{B_2}$
3	$\mathrm{C_{3v}}$	$\mathrm{A_1}$	$\mathrm{A_1} \oplus \mathrm{E}$	$\mathrm{A_1} \oplus 2\mathrm{E}$
4	$\mathrm{C_{4v}}$	$\mathrm{A_1}$	$\mathrm{A_1} \oplus \mathrm{E}$	$\mathrm{A_1} \oplus \mathrm{B_1} \oplus \mathrm{B_2} \oplus \mathrm{E}$

Table 3.1: Little groups for all momentum sectors $\boldsymbol{d}^2$ used in this work. Additionally the decomposition of angular momentum irrep for L up to d-wave into irreps of the little group $\mathrm{LG}(\boldsymbol{d}_{\mathrm{cm}})$ is given. [22, 54]

as

$$\mathrm{L} \to \bigoplus_{i=1}^{N_\Gamma} n_i \Gamma_i \,, \qquad \sum_i n_i \cdot \dim(\Gamma_i) = 2l+1 \,. \tag{2.82}$$

Concretely for p-wave and $\boldsymbol{d}^2 \leq 4$ and up to d-wave, the decompositions were for instance given in [22, 54] and are reproduced in Tab. 3.1. It is immediately apparent that for non-zero $\boldsymbol{d}^2$, $\mathrm{A_1}$ receives contributions from all partial waves and depending on the moving frame E or B1 and B2 from p- and d-wave.

For a $\pi\pi$-system in the vector channel however, there are additional symmetries that prevents such partial wave mixing. The only possible quantum numbers are $I^G J^{PC} = 0^+0^{++}, 1^-1^{--}, 2^+0^{++}, 2^+2^{++}$ and therefore mixing of even and odd partial waves is forbidden by isospin, parity and charge conjugation. If QCD is formulated using the twisted mass regularization introduced in Sec. 2.2.1 I and P are no longer good quantum numbers, although violations are suppressed by $\mathcal{O}\left(a^2\right)$ and for the ρ no significant isospin splitting has been observed [74]. However C-symmetry is still exact and therefore mixing of even and odd partial waves is forbidden also with twisted mass. Beyond that, the contributions from f wave have been analysed and found to be negligible [29, 31].

Neglecting highr partial waves is in accordance with the experiments which almost exclusively measured p-wave. For $l = 1$ all multiplicities are simply $n = 1$ and Eq. (2.97) simplifies to

$$\delta_1(k) = \operatorname{arccot} M_{11,11}^{\boldsymbol{d}_{\mathrm{cm}},\Gamma,\alpha}(k) \,. \tag{3.4}$$

The matrix elements for $\boldsymbol{d}_{\mathrm{cm}}$ are calculated from Eq. (2.96) and are listed in Tab. 3.2. Due to the degeneracies of different momenta and rows discussed in Sec. 2.6, the choice of $\boldsymbol{d}_{\mathrm{cm}}$ and α is arbitrary. There are several symmetries of the zeta function $\mathcal{Z}_{lm}^{\vec{d}}$ which we ignored for simplicity. They may be used to simplify the expressions for $M^{\boldsymbol{d},\Gamma,\alpha}$ [22], but the result will be identical up to numeric precision.

3.2 Operator construction

In Sec. 2.6 the existence of operators interpolating to lattice states $|\boldsymbol{p};\Gamma,\alpha\rangle$ was assumed. This chapter illustrates how these operators are constructed in practice. The construction will focus on the ρ operators that are used in this work but the steps to generalize the procedure to other physical processes will be covered as well.

$\boldsymbol{d}_{\mathrm{cm}}$	Γ	α	$M^{\boldsymbol{d}_{\mathrm{cm}},\Gamma,\alpha}_{11,11}$
$(0,0,0)$	T1u	2	$w_{0,0} - w_{2,0} - \frac{3}{\sqrt{6}} w_{2,-2} - \frac{3}{\sqrt{6}} \cdot w_{2,2}$
$(0,0,1)$	A1	1	$w_{0,0} + 2 \cdot w_{2,0}$
$(0,0,1)$	E	1	$w_{0,0} - w_{2,0} + \frac{3i}{\sqrt{6}} \cdot w_{2,-2} - \frac{3i}{\sqrt{6}} \cdot w_{2,2}$
$(1,1,0)$	A1	1	$w_{0,0} - w_{2,0} + \frac{3i}{\sqrt{6}} \cdot w_{2,-2} - \frac{3i}{\sqrt{6}} i \cdot w_{2,2}$
$(1,1,0)$	B1	1	$w_{0,0} + 2 \cdot w_{2,0}$
$(1,1,0)$	B2	1	$w_{0,0} - w_{2,0} - \frac{3i}{\sqrt{6}} \cdot w_{2,-2} + \frac{3i}{\sqrt{6}} \cdot w_{2,2}$
$(1,1,1)$	A1	1	$w_{0,0} + 2 \cdot \frac{1+i}{\sqrt{6}} \cdot w_{2,-1} - 2 \cdot \frac{1-i}{\sqrt{6}} \cdot w_{2,1} + \frac{2i}{\sqrt{6}} \cdot w_{2,-2} - \frac{2i}{\sqrt{6}} \cdot w_{2,2}$
$(1,1,1)$	E	1	$w_{0,0} - \frac{1+i}{\sqrt{6}} \cdot w_{2,-1} + \frac{1-i}{\sqrt{6}} \cdot w_{2,1} - \frac{i}{\sqrt{6}} \cdot w_{2,-2} + \frac{i}{\sqrt{6}} \cdot w_{2,2}$
$(0,0,2)$	A1	1	$w_{0,0} + 2 \cdot w_{2,0}$
$(0,0,2)$	E	1	$w_{0,0} - w_{2,0} + \frac{3i}{\sqrt{6}} \cdot w_{2,-2} - \frac{3i}{\sqrt{6}} \cdot w_{2,2}$

Table 3.2: Matrix elements for all momentum sectors $\boldsymbol{d}^2$ and irreps Γ used in this work. Each momentum sector is represented by a single choise $\boldsymbol{d}_{\mathrm{cm}} \in \{\, \boldsymbol{d} \,\}$ and $1 < \alpha < \dim(\Gamma)$.

Any nontrivial state in a field theory can be created from the vacuum by an appropriate interpolating field operator. In particular one can find an interpolating operator for each basis state of the QCD Hamiltionian in angular momentum space. Let $\mathcal{O}^m_{\mathrm{L}}(\boldsymbol{p})^\dagger$ by such an operator that creates

$$|\boldsymbol{p}, \mathrm{L}, m\rangle = \mathcal{O}^m_{\mathrm{L}}(\boldsymbol{p})^\dagger \, |0\rangle \tag{3.5}$$

where $|0\rangle$ denotes the vacuum. Operators may be used interchangeably with the basis states themselves. This means that the projection discussed in Sec. 2.3.3 and discussion of momentum in Sec. 2.4 also hold for operators.

3.2.1 Continuum operators

The arguably simplest operator that couples to the ρ channel is an antisymmetric quark bilinear [75]

$$\rho(x) = \frac{1}{\sqrt{2}} (\bar{u}(x)^c_\alpha \gamma^\rho_{\alpha\beta} u(x)^c_\beta - \bar{d}(x)^c_\alpha \gamma^\rho_{\alpha\beta} d(x)^c_\beta) \tag{3.6}$$

which resembles the ρ^0. α and β denote spin indices and c colour. It has isospin $|1,0\rangle_I$ and the Dirac matrix γ^ρ must be chosen such that ρ transforms like $J^{PC} = 1^{--}$. Without using derivative operators the only options are $\gamma^\rho \in \{\, \mathrm{i}\gamma_i, \gamma_0\gamma_i \,\}$ and obviously linear combinations of these.

The ρ channel is known to have two low-lying energy levels very close together. The separation of these is obstructed by one of these states coupling only weakly to operators like in Eq. (3.6). In practice, just single-meson operators are not sufficient to disentangle the states. In order to

properly calculate the interacting energy levels, also two-meson operators are necessary. [27, 76] In the rho channel the natural choice are operators composed of two pions. The physical states are separated by solving a generalized eigenvalue problem as explained in Sec. 2.6.

The simplest operator that couples the $\pi^{\pm}$ channel is again a quark bilinear [75]

$$\pi^+(x) = \bar{\psi}_d(x)^c_\alpha \gamma^\pi_{\alpha\beta} \psi_u(x)^c_\beta \text{ or } \qquad \pi^-(x) = \bar{\psi}_u(x)^c_\alpha \gamma^\pi_{\alpha\beta} \psi_d(x)^c_\beta \,, \tag{3.7}$$

this time with definite isospin $|1, \pm 1\rangle_I$ for $\pi^{\pm}$. The Dirac matrix γ^π must again be chosen such that $\pi^{\pm}$ transform like $J^{PC} = 0^{-+}$. In this work we will always use $\gamma^\pi = \mathrm{i}\gamma_5$. Except for operators including derivatives, $\gamma_0\gamma_5$ would also have the right quantum numbers, but a worse signal to noise ratio.

To obtain a two-pion operator that couples to the ρ channel, the $\pi^{\pm}$ operators must be coupled to isospin $|1, 0\rangle$. In analogy to the Clebsch-Gordan decomposition

$$|1,0\rangle = \frac{1}{\sqrt{2}} \left(|1,+1\rangle \otimes |1,-1\rangle - |1,-1\rangle \otimes |1,+1\rangle \right) \tag{3.8}$$

the operator is

$$\begin{aligned} \pi\pi(t, \boldsymbol{x}_1, \boldsymbol{x}_2) &= \frac{1}{\sqrt{2}} \left(\pi^+(t, \boldsymbol{x}_1)\pi^-(t, \boldsymbol{x}_2) - \pi^-(t, \boldsymbol{x}_1)\pi^+(t, \boldsymbol{x}_2) \right) \\ &= \frac{1}{\sqrt{2}} \Big(\bar{\psi}_d(\boldsymbol{x}_1)_\alpha \gamma^\pi_{\alpha\beta} \psi_u(\boldsymbol{x}_1)_\beta \bar{\psi}_u(\boldsymbol{x}_2)_\gamma \gamma^\pi_{\gamma\delta} \psi_d(\boldsymbol{x}_2)_\delta - \\ &\qquad \bar{\psi}_u(\boldsymbol{x}_1)_\alpha \gamma^\pi_{\alpha\beta} \psi_d(\boldsymbol{x}_1)_\beta \bar{\psi}_d(\boldsymbol{x}_2)_\gamma \gamma^\pi_{\gamma\delta} \psi_u(\boldsymbol{x}_2)_\delta \Big) \,. \end{aligned} \tag{3.9}$$

Both pions are created and accordingly annihilated at different spatial lattice sites $\boldsymbol{x}_1$ and $\boldsymbol{x}_2$ but at the same time t. A temporal seperation of particles is possible but tremendously increases the complexity of the calculation without measurable effects on the result.

In order to interpolate to a state $|\boldsymbol{p}, \mathrm{L}, m\rangle$, two more changes need to be implemented. The first is to project the operators to momentum $\boldsymbol{p}$. For the single-meson operators in position space is done via a discrete Fourier transformation

$$\mathcal{O}(t, \boldsymbol{p}) \;=\; \sum_{\boldsymbol{x}} \; \mathcal{O}(t, \boldsymbol{x})\, e^{\mathrm{i}\boldsymbol{x}\boldsymbol{p}} \,. \tag{3.10}$$

For two-meson operators, the Fourier transformation must be applied to each spatial lattice site,

$$\mathcal{O}(t, \boldsymbol{p}_1, \boldsymbol{p}_2) = \sum_{\boldsymbol{x}_1, \boldsymbol{x}_2} \mathcal{O}(t, \boldsymbol{x}_1, \boldsymbol{x}_2)\, e^{\mathrm{i}\boldsymbol{x}_1\boldsymbol{p}_1}\, e^{\mathrm{i}\boldsymbol{x}_2\boldsymbol{p}_2} \,. \tag{3.11}$$

The second change is to project the operators to definite magnetic quantum number m. This is done by using the standard (covariant) spherical instead of the cartesian basis. Our conventions

for Dirac matrices are given in Sec. A.3. The Dirac-matrices used in Eq. (3.6) are

$$\begin{aligned}\gamma^{+1} &= -\frac{\mathrm{i}}{\sqrt{2}}\left(\gamma_1 - \mathrm{i}\gamma_2\right)\\ \gamma^{0} &= \mathrm{i}\gamma_3\\ \gamma^{-1} &= \frac{\mathrm{i}}{\sqrt{2}}\left(\gamma_1 + \mathrm{i}\gamma_2\right)\end{aligned} \tag{3.12}$$

and analogously for $\gamma_0\gamma_i$. For the pseudoscalars in Eq. (3.7), the basis is one-dimensional and therefore the basis change is trivial. For consistency the Dirac matrix is also labelled by m

$$\gamma^0 = \mathrm{i}\gamma_5 \tag{3.13}$$

nevertheless.

3.2.2 Operators in the twisted basis

The chiral transformation to maximal twist might further change the gamma-matrices in Eq. (3.12)-(3.13). In this section a dictionary between the used physical operators and their twisted counterpart is created by explicitly carrying out the transformation.

The quark fields in the twisted basis are connected to the physical basis by (2.41). Inverting the relation yields the back-transformation

$$\psi = \mathrm{e}^{+\mathrm{i}\gamma_5\tau_3\alpha_{\mathrm{tm}}/2}\chi\,. \tag{3.14}$$

We may expand the exponential into sine and cosine to arrive at a much more applicable expression at maximal twist. The general result is

$$\begin{aligned}\mathrm{e}^{-\mathrm{i}\gamma_5\tau_3\alpha_{\mathrm{tm}}/2} &= \sum_{n=0}^{\infty}\frac{1}{(2n)!}\left(\mathrm{i}\gamma_5\tau_3\frac{\alpha_{\mathrm{tm}}}{2}\right)^{2n} + \sum_{n=0}^{\infty}\frac{1}{(2n+1)!}\left(\mathrm{i}\gamma_5\tau_3\frac{\alpha_{\mathrm{tm}}}{2}\right)^{2n+1}\\ &= \sum_{n=0}^{\infty}\left(\frac{1}{(2n)!}(-1)^n\left(\frac{\alpha_{\mathrm{tm}}}{2}\right)^{2n}\right) + \mathrm{i}\sum_{n=0}^{\infty}\left(\frac{1}{(2n+1)!}(-1)^n\left(\frac{\alpha_{\mathrm{tm}}}{2}\right)^{2n+1}\right)\gamma_5\tau_3\\ &= \cos\left(\frac{\alpha_{\mathrm{tm}}}{2}\right) + \mathrm{i}\sin\left(\frac{\alpha_{\mathrm{tm}}}{2}\right)\gamma_5\tau_3\end{aligned}$$

and at maximal twist i.e. $\alpha_{\mathrm{tm}} = \frac{\pi}{2}$ it simplifies to

$$\mathrm{e}^{-i\gamma_5\tau_3\pi/4} = \frac{1}{\sqrt{2}} + \frac{\mathrm{i}}{\sqrt{2}}\gamma_5\tau_3\,. \tag{3.15}$$

Applying this transformation to a doublet of light quarks yields

$$\psi \equiv \begin{pmatrix}\psi_u\\ \psi_d\end{pmatrix} = \left(\frac{1}{\sqrt{2}}\begin{pmatrix}1 & 0\\ 0 & 1\end{pmatrix} + \frac{\mathrm{i}}{\sqrt{2}}\gamma_5\begin{pmatrix}1 & 0\\ 0 & -1\end{pmatrix}\right)\cdot\begin{pmatrix}\chi_u\\ \chi_d\end{pmatrix} = \begin{pmatrix}\left(\frac{1}{\sqrt{2}} + \frac{\mathrm{i}}{\sqrt{2}}\gamma_5\right)\chi_u\\ \left(\frac{1}{\sqrt{2}} - \frac{\mathrm{i}}{\sqrt{2}}\gamma_5\right)\chi_d\end{pmatrix}\,. \tag{3.16}$$

Particle	Physical basis	Twisted basis
$\pi^{\pm}$	$\bar{\psi}_{d/u} i\gamma_5 \psi_{u/d}$	$\bar{\chi}_{d/u} i\gamma_5 \chi_{u/d}$
π^{+}	$\bar{\psi}_{d} \gamma_0\gamma_5 \psi_{u}$	$\bar{\chi}_{d} i\gamma_0 \chi_{u}$
π^{-}	$\bar{\psi}_{u} \gamma_0\gamma_5 \psi_{d}$	- $\bar{\chi}_{u} i\gamma_0 \chi_{d}$
ρ^{0}	$\bar{\psi}_{u} i\gamma_i \psi_{u} - \bar{\psi}_{d} i\gamma_i \psi_{d}$	$\bar{\chi}_{u} i\gamma_i \chi_{u} - \bar{\chi}_{d} i\gamma_i \chi_{d}$
ρ^{0}	$\bar{\psi}_{u} \gamma_0\gamma_i \psi_{u} - \bar{\psi}_{d} \gamma_0\gamma_i \psi_{d}$	$\bar{\chi}_{u} i\gamma_0\gamma_i\gamma_5 \chi_{u} + \bar{\chi}_{d} i\gamma_0\gamma_i\gamma_5 \chi_{d}$

Table 3.3: Juxtaposition of interpolating operators in the physical and twisted basis.

As an example the transformation is carried out for the π^+ operator from Eq. (3.7):

$$\begin{aligned}
\bar{\psi}_d \mathrm{i}\gamma_5 \psi_u &= \mathrm{i}\psi_d^\dagger \gamma_0\gamma_5 \psi_u \\
&= \mathrm{i}\chi_d^\dagger \left(\frac{1}{\sqrt{2}} - \frac{\mathrm{i}}{\sqrt{2}}\gamma_5\right)^\dagger \gamma_0\gamma_5 \left(\frac{1}{\sqrt{2}} + \frac{\mathrm{i}}{\sqrt{2}}\gamma_5\right) \chi_u \\
&= \frac{\mathrm{i}}{2}\chi_d^\dagger \gamma_0\gamma_5 \chi_u + \frac{\mathrm{i}^2}{2}\chi_d^\dagger \gamma_5\gamma_0\gamma_5 \chi_u + \frac{\mathrm{i}^2}{2}\chi_d^\dagger \gamma_0\gamma_5\gamma_5 \chi_u + \frac{\mathrm{i}^3}{2}\chi_d^\dagger \gamma_5\gamma_0\gamma_5\gamma_5 \chi_u \\
&= \frac{\mathrm{i}}{2}\chi_d^\dagger \gamma_0\gamma_5 \chi_u + \frac{1}{2}\chi_d^\dagger \gamma_0 \chi_u - \frac{1}{2}\chi_d^\dagger \gamma_0 \chi_u + \frac{\mathrm{i}}{2}\chi_d^\dagger \gamma_0\gamma_5 \chi_u \\
&= \mathrm{i}\chi_d^\dagger \gamma_0\gamma_5 \chi_u \\
&= \bar{\chi}_d \mathrm{i}\gamma_5 \chi_u \,.
\end{aligned} \tag{3.17}$$

For other operators the calculation works analogously. It should be noted, that the term $1/2\chi_d^\dagger\gamma_0\chi_u$ canceled in the calculation. In general the operators in the twisted basis are linear combinations of multiple different operators in the physical basis. The subsequent calculation must be performed for each term that arises. In the case of the ρ meson it turns out that one term always cancels, such that there is always a one-to-one correspondence between twisted and physical basis, although the relation is not necessarily the identity as the gamma-matrix changes for some operators. The results are summarized in Tab. 3.3. Furthermore isospin is broken by twisted mass and indeed e.g. the neutral π and charged ρ mesons transform differently from their counterparts. For more details on the relation between the physical and the twisted basis, we refer to the original publications [77–79] as well as [80] for a review.

3.3 Projection of operators

In Sec. 2.3.3 the projection operator

$$\hat{P}^{\Gamma}_{\alpha\beta}(\boldsymbol{p}_{\mathrm{cm}}) = \frac{\dim(\Gamma)}{|\mathrm{LG}(\boldsymbol{p}_{\mathrm{cm}})|} \sum_{g\in \mathrm{LG}(\boldsymbol{p}_{\mathrm{cm}})} D^{\Gamma}(g)^*_{\alpha\beta} \hat{R}_g \tag{2.87}$$

was applied to an angular momentum state $|\mathrm{L}, m\rangle$. The result was a linear combination of lattice eigenstates with the subduction coefficients $s^{\Gamma,\alpha,n}_{\mathrm{L},m}$

$$|\Gamma, \alpha, (\mathrm{L}, n)\rangle = \sum_m s^{\Gamma,\alpha,n}_{\mathrm{L},m} |\mathrm{L}, m\rangle \ . \tag{2.90}$$

For the operators in this work the action of Eq. (2.87) on the linear momentum $\boldsymbol{p}$ must be considered as well. In Sec. 2.4 the action of $\hat{R}_g$ on a state with momentum was derived:

$$\begin{aligned}\hat{R}\,|\boldsymbol{p};\mathrm{L},m\rangle &= \hat{R}\,|\boldsymbol{p}\rangle \otimes \hat{R}\,|\mathrm{L},m\rangle \\ &= \left|\hat{R}\,\boldsymbol{p}\right\rangle \otimes \sum_{m'} D^{\mathrm{L}}(R)_{m'm}\ \left|\mathrm{L},m'\right\rangle \\ &= \sum_{m'} D^{\mathrm{L}}(R)_{m'm}\ \left|\hat{R}\,\boldsymbol{p};\mathrm{L},m'\right\rangle .\end{aligned} \tag{2.100}$$

Single meson operator the momentum of a single meson is by definition the CM-momentum of the system. Therefore the only relevant projection is

$$\sum_{\beta}\phi_\beta \sum_{m}\phi_m \hat{P}^{\Gamma}_{\alpha\beta}(\boldsymbol{p}_{\mathrm{cm}})\ \mathcal{O}^{m}_{\mathrm{L}}(\boldsymbol{p}_{\mathrm{cm}})^\dagger \tag{3.18}$$

with the momenta aligned. By definition all rotations in the projection operator are the elements of $\mathrm{LG}(\boldsymbol{p}_{\mathrm{cm}})$ which leave $\boldsymbol{p}_{\mathrm{cm}}$ invariant and thus may be factored out from the projection. Applying the projected operator onto a vacuum state

$$\begin{aligned}\mathcal{O}^{\alpha}_{\Gamma}(\boldsymbol{p}_{\mathrm{cm}})^\dagger\,|0\rangle &\equiv \sum_{\beta}\phi_\beta \sum_{m}\phi_m \hat{P}^{\Gamma}_{\alpha\beta}(\boldsymbol{p}_{\mathrm{cm}})\ \mathcal{O}^{m}_{\mathrm{L}}(\boldsymbol{p}_{\mathrm{cm}})^\dagger\,|0\rangle \\ &= |\boldsymbol{p}_{\mathrm{cm}}\rangle \otimes \sum_{\beta}\phi_\beta \sum_{m}\phi_m \hat{P}^{\Gamma}_{\alpha\beta}(\boldsymbol{p}_{\mathrm{cm}})\,|\mathrm{L},m\rangle \\ &= |\boldsymbol{p}_{\mathrm{cm}}\rangle \otimes \sum_{m} s^{\Gamma,\alpha,n}_{\mathrm{L},m}\,|\mathrm{L},m\rangle \\ &= \sum_{m} s^{\Gamma,\alpha,n}_{\mathrm{L},m}\mathcal{O}^{m}_{\mathrm{L}}(\boldsymbol{p}_{\mathrm{cm}})^\dagger\,|0\rangle\end{aligned} \tag{3.19}$$

one indeed finds a relation in analogy to Eq. (2.90). As the state is arbitrary, Eq. (3.3) leads to the general operator identity

$$\mathcal{O}^{\alpha}_{\Gamma}(\boldsymbol{p}_{\mathrm{cm}})^\dagger = \sum_{m} s^{\Gamma,\alpha,n}_{\mathrm{L},m}\mathcal{O}^{m}_{\mathrm{L}}(\boldsymbol{p}_{\mathrm{cm}})^\dagger \qquad\qquad \mathcal{O}^{\alpha}_{\Gamma}(\boldsymbol{p}_{\mathrm{cm}}) = \sum_{m} s^{\Gamma,\alpha,n*}_{\mathrm{L},m}\mathcal{O}^{m}_{\mathrm{L}}(\boldsymbol{p}_{\mathrm{cm}})\,. \tag{3.20}$$

There is one lattice ρ operator

$$\rho^{\alpha}_{\Gamma\gamma}(\boldsymbol{p}_{\mathrm{cm}})^\dagger = \sum_{m} s^{\Gamma,\alpha,n}_{\mathrm{L},m}\sum_{\boldsymbol{x}} \mathrm{e}^{\mathrm{i}\boldsymbol{x}\boldsymbol{p}}\rho_\gamma(\boldsymbol{x})^\dagger \tag{3.21}$$

for each of $\gamma^\rho \in \{\,\mathrm{i}\gamma_m, \gamma_0\gamma_i\,\}$. For brevity they will be denoted as ρ_m and ρ_{50m} (in the twisted basis).

Two-meson operators For more than one particle the action of the projection operator on momenta becomes non-trivial.

Let $\mathcal{O}^{\dagger}_{\mathrm{L}_1}(\boldsymbol{p}_1), \mathcal{O}^{\dagger}_{\mathrm{L}_2}(\boldsymbol{p}_2)$ be single-meson operators that belong to the L_1- and L_2-irrep of SO(3) respectively and let $\boldsymbol{p}_1$ and $\boldsymbol{p}_2$ be the momenta of the individual pions. The CM momentum is

the sum

$$\boldsymbol{p}_{\mathrm{cm}} = \boldsymbol{p}_1 + \boldsymbol{p}_2 \tag{3.22}$$

of both the particle's individual momenta.

The two-meson operator interpolating to a state with $|\boldsymbol{p}_{\mathrm{cm}}, \mathrm{L}, m\rangle$ is

$$\begin{aligned}\mathcal{O}^{m\dagger}_{\mathrm{L}}(\boldsymbol{p}_1, \boldsymbol{p}_2) &= \mathcal{O}^{m_1\dagger}_{\mathrm{L}_1}(\boldsymbol{p}_1) \otimes \mathcal{O}^{m_2\dagger}_{\mathrm{L}_2}(\boldsymbol{p}_2) \\ &= \sum_{m_1,m_2} \langle l, m \; | l_1, m_1; l_2, m_2\rangle \, \mathcal{O}^{m_1\dagger}_{l_1}(\boldsymbol{p}_1)\mathcal{O}^{m_2\dagger}_{l_2}(\boldsymbol{p}_2)\,.\end{aligned} \tag{3.23}$$

In the last line the operator product was decomposed via Clebsch-Gordan decomposition where $\langle l, m| \; l_1, m_1; l_2, m_2\rangle$ denotes the Clebsch-Gordan coefficient for $l_1 \otimes l_2$ coupling to l.

The individual momenta $\boldsymbol{p}_1$ and $\boldsymbol{p}_2$ no longer have to be aligned to $\boldsymbol{p}_{\mathrm{cm}}$. If they are not, the rotation must be explicitly carried out. It will turn out useful to introduce the (half) momentum transfer

$$\boldsymbol{q} = \frac{1}{2}(\boldsymbol{p}_1 - \boldsymbol{p}_2)\,. \tag{3.24}$$

Together with Eq. (3.22) $\boldsymbol{p}_1$ and $\boldsymbol{p}_2$ may be expressed as

$$\boldsymbol{p}_1 = \frac{1}{2}\boldsymbol{p}_{\mathrm{cm}} + \boldsymbol{q} \qquad \boldsymbol{p}_2 = \frac{1}{2}\boldsymbol{p}_{\mathrm{cm}} - \boldsymbol{q}\,. \tag{3.25}$$

By definition $\boldsymbol{p}_{\mathrm{cm}}$ is invariant under the action of $\mathrm{LG}(\boldsymbol{p}_{\mathrm{cm}})$ and therefore only $\boldsymbol{q}$ transforms under rotations. In this form by choosing different $\boldsymbol{q}$ one obtains different operators all of which interpolate to $|\boldsymbol{p}_{\mathrm{cm}}; \Gamma, \alpha\rangle$. At this point, we reap the benefits of the preparations in Sec. 2.5. Retroactively identifying which values of $\boldsymbol{q}$ are physically equivalent for different $\boldsymbol{p}_{\mathrm{cm}}$ is a tedious task. By proactively using the projector defined in Eq. (2.117) it becomes straightforward. By again applying the projected operator to a vacuum state

$$\begin{aligned}\mathcal{O}^{\alpha\dagger}_{\Gamma}(\boldsymbol{p}_{\mathrm{cm}})\,|0\rangle &= \sum_{\beta}\phi_\beta \sum_{m}\phi_m \hat{P}^{\Gamma,l}_{\alpha\beta}(\boldsymbol{p}_{\mathrm{cm}})\mathcal{O}^{m}_{\mathrm{L}}(\boldsymbol{p}_{\mathrm{cm}})\,|0\rangle \\ &= \sum_{\beta}\phi_\beta \sum_{m}\phi_m \sum_{m_1,m_2} \langle l, m| \; l_1, m_1; l_2, m_2\rangle \\ &\quad \frac{\dim(\Gamma)}{|\mathrm{LG}(\boldsymbol{p}_{\mathrm{cm}})|} \sum_{g\in \mathrm{LG}(\boldsymbol{p}_{\mathrm{cm}})} D^{\Gamma}(R_g)^*_{\alpha\beta} \sum_{\boldsymbol{x}_1,\boldsymbol{x}_2} \exp\Big(\mathrm{i}\boldsymbol{x}_1 \cdot \hat{R}_{\mathrm{Ad}_{\tilde{g}}(g)}\boldsymbol{p}_1 + \mathrm{i}\boldsymbol{x}_2 \cdot \hat{R}_{\mathrm{Ad}_{\tilde{g}}(g)}\boldsymbol{p}_2\Big) \\ &\quad \sum_{m_1'} D^{\mathrm{L}_1}_{m_1' m_1}(R_{\mathrm{Ad}_{\tilde{g}}(g)})\,\mathcal{O}^{m_1'\dagger}_{\mathrm{L}_1}(\boldsymbol{x}_1) \sum_{m_2'} D^{\mathrm{L}_2}_{m_2' m_2}(R_{\mathrm{Ad}_{\tilde{g}}(g)})\,\mathcal{O}^{m_2'\dagger}_{\mathrm{L}_2}(\boldsymbol{x}_2)\,|0\rangle\end{aligned} \tag{3.26}$$

albeit far more complicated than Eq. (3.20) one again finds an operator identity. The global rotation to another $\boldsymbol{p} \in \{\, \boldsymbol{p}_{\mathrm{cm}} \,\}$ now only requires inserting the representative $\tilde{g}$ of another coset.

$\boldsymbol{d}_{\mathrm{cm}}$	Γ	$\boldsymbol{p}_1 \otimes \boldsymbol{p}_2$
$(0,0,0)$	T1u	$(0,0,1)\otimes(0,0,-1)$, $(1,0,1)\otimes(-1,0,-1)$
$(0,0,1)$	A1	$(0,0,1)\otimes(0,0,0)$, $(0,0,2)\otimes(0,0,-1)$, $(1,0,1)\otimes(-1,0,0)$, $(1,1,1)\otimes(-1,-1,0)$
$(0,0,1)$	E	$(0,1,1)\otimes(0,-1,0)$, $(1,1,1)\otimes(-1,-1,0)$
$(1,1,0)$	A1	$(1,1,0)\otimes(0,0,0)$, $(1,1,1)\otimes(0,0,-1)$, $(1,-1,0)\otimes(0,2,0)$
$(1,1,0)$	B1	$(1,1,1)\otimes(0,0,-1)$, $(1,0,1)\otimes(0,1,-1)$
$(1,1,0)$	B2	$(1,0,0)\otimes(0,1,0)$, $(1,0,1)\otimes(0,1,-1)$, $(2,0,0)\otimes(-1,1,0)$
$(1,1,1)$	A1	$(1,1,1)\otimes(0,0,0)$, $(1,0,1)\otimes(0,1,0)$, $(2,0,0)\otimes(-1,1,1)$
$(1,1,1)$	E	$(1,0,1)\otimes(0,1,0)$, $(1,-1,1)\otimes(0,2,0)$
$(0,0,2)$	A1	$(0,0,2)\otimes(0,0,0)$
$(0,0,2)$	E	$(0,1,1)\otimes(0,-1,1)$

Table 3.4: Momentum combinations $\boldsymbol{p}_1 \otimes \boldsymbol{p}_2$ used in Eq. (3.27). We only give one representative CM momentum $\boldsymbol{p}_{\mathrm{cm}} = 2\pi/L\boldsymbol{d}$ for each momentum sector. The other directions may be generated by a global rotation. The momentum combinations depend on the irrep Γ because not all combinations couple to all irreps in which case Eq. (3.27) simply adds up zero.

$\boldsymbol{d}_{\mathrm{cm}}$	Γ	$\boldsymbol{q}$
$(0,0,0)$	T1u	$(0,0,1)$, $(1,0,1)$
$(0,0,1)$	A1	$(0,0,0.5)$, $(0,0,1.5)$, $(1,0,0.5)$, $(1,1,0.5)$
$(0,0,1)$	E	$(0,1,0.5)$, $(1,1,0.5)$
$(1,1,0)$	A1	$(0.5,0.5,0)$, $(0.5,0.5,1)$, $(0.5,-1.5,0)$
$(1,1,0)$	B1	$(0.5,0.5,1)$, $(0.5,-0.5,1)$
$(1,1,0)$	B2	$(0.5,-0.5,0)$, $(0.5,-0.5,1)$, $(1.5,-0.5,0)$
$(1,1,1)$	A1	$(0.5,0.5,0.5)$, $(0.5,-0.5,0.5)$, $(1.5,-0.5,-0.5)$
$(1,1,1)$	E	$(0.5,-0.5,0.5)$, $(0.5,-1.5,0.5)$
$(0,0,2)$	A1	$(0,0,1)$
$(0,0,2)$	E	$(1,0,0)$

Table 3.5: Same as 3.4 but expressed by $\boldsymbol{q}$ via Eq. (3.24).

Reexpressing the momenta with Eq. (3.25) we may write

$$
\begin{aligned}
&\mathcal{O}^{\alpha\dagger}_{\Gamma\boldsymbol{q}}(\boldsymbol{p}_{\mathrm{cm}}) \equiv \mathcal{O}^{\alpha}_{\Gamma}(\boldsymbol{p}_1,\boldsymbol{p}_2) \\
&\quad= \sum_{\beta}\phi_\beta \sum_{m}\phi_m \sum_{m_1,m_2} \langle l,m|\ l_1,m_1;l_2,m_2\rangle \,\frac{\dim(\Gamma)}{|\mathrm{LG}(\boldsymbol{p}_{\mathrm{cm}})|} \sum_{g\in \mathrm{LG}(\boldsymbol{p}_{\mathrm{cm}})} D^{\Gamma}(R_g)^*_{\alpha\beta} \\
&\qquad \sum_{\boldsymbol{x}_1,\boldsymbol{x}_2} \exp\!\left(\mathrm{i}\boldsymbol{x}_1\cdot\left(\frac{1}{2}\boldsymbol{p}_{\mathrm{cm}} + \hat{R}_{\mathrm{Ad}_{\tilde{g}}(g)}\boldsymbol{q}\right) + \mathrm{i}\boldsymbol{x}_2\cdot\left(\frac{1}{2}\boldsymbol{p}_{\mathrm{cm}} - \hat{R}_{\mathrm{Ad}_{\tilde{g}}(g)}\boldsymbol{q}\right)\right) \\
&\qquad \sum_{m_1'} D^{\mathrm{L}_1}_{m_1' m_1}(R_{\mathrm{Ad}_{\tilde{g}}(g)})\,\mathcal{O}^{m_1'\dagger}_{\mathrm{L}_1}(\boldsymbol{x}_1) \sum_{m_2'} D^{\mathrm{L}_2}_{m_2' m_2'}(R_{\mathrm{Ad}_{\tilde{g}}(g)})\,\mathcal{O}^{m_2'\dagger}_{\mathrm{L}_2}(\boldsymbol{x}_2)\,.
\end{aligned}
\tag{3.27}
$$

If two values $\boldsymbol{q}$ and $\boldsymbol{q}'$ are connected by a rotation $\hat{R}_g\boldsymbol{q} = \boldsymbol{q}'$ for some $g \in \mathrm{LG}(\boldsymbol{p}_{\mathrm{cm}})$, the summands are only reordered due to the sum over all elements of $\mathrm{LG}(\boldsymbol{p}_{\mathrm{cm}})$. Up to a possible phase the resulting operators are ambiguous. In Tab. 3.4 we give our lists of momentum combinations $\boldsymbol{p}_1 \otimes \boldsymbol{p}_2$ for one representative combinations of each momentum sector. In Tab. 3.5

we give the same lists but reexpressed by $\boldsymbol{q}$ using Eq. (3.24).

Two-pion operator The $\pi\pi$ operator is a special case as both single-meson operators are (pseudo-)scalar and therefore invariant under rotations.[1] The sums over m_1' and m_2' in Eq. (3.27) drop out and the operator simplifies to

$$\begin{aligned}\pi^+\pi^-{}^{\alpha\dagger}_{\Gamma\boldsymbol{q}}(\boldsymbol{p}_{\mathrm{cm}}) = \sum_\beta \phi_\beta \sum_m \phi_m \sum_{m_1,m_2} \langle l,m|\ l_1,m_1;l_2,m_2\rangle \frac{\dim(\Gamma)}{|\mathrm{LG}(\boldsymbol{p}_{\mathrm{cm}})|} \sum_{g\in\mathrm{LG}(\boldsymbol{p}_{\mathrm{cm}})} D^\Gamma(R_g)^*_{\alpha\beta} \\ \sum_{\boldsymbol{x}_1,\boldsymbol{x}_2} \exp\!\left(\mathrm{i}\boldsymbol{x}_1\cdot\left(\frac{1}{2}\boldsymbol{p}_{\mathrm{cm}} + \hat{R}_{\mathrm{Ad}_{\bar{g}}(g)}\boldsymbol{q}\right) + \mathrm{i}\boldsymbol{x}_2\cdot\left(\frac{1}{2}\boldsymbol{p}_{\mathrm{cm}} - \hat{R}_{\mathrm{Ad}_{\bar{g}}(g)}\boldsymbol{q}\right)\right) \\ \pi^+(\boldsymbol{x}_1)\,\pi^-(\boldsymbol{x}_2)\,.\end{aligned} \tag{3.28}$$

Finally the isospin projection Eq. (3.9) gives

$$\begin{aligned}\pi\pi^{\alpha\dagger}_{\Gamma\boldsymbol{q}}(\boldsymbol{p}_{\mathrm{cm}}) &= \frac{1}{\sqrt{2}}\left(\pi^+\pi^-{}^{\alpha\dagger}_{\Gamma\boldsymbol{q}}(\boldsymbol{p}_{\mathrm{cm}}) - \pi^-\pi^+{}^{\alpha\dagger}_{\Gamma\boldsymbol{q}}(\boldsymbol{p}_{\mathrm{cm}})\right) \\ &= \frac{1}{\sqrt{2}}\sum_\beta \phi_\beta \sum_m \phi_m \sum_{m_1,m_2} \langle l,m|\ l_1,m_1;l_2,m_2\rangle \frac{\dim(\Gamma)}{|\mathrm{LG}(\boldsymbol{p}_{\mathrm{cm}})|} \sum_{g\in\mathrm{LG}(\boldsymbol{p}_{\mathrm{cm}})} D^\Gamma(R_g)^*_{\alpha\beta} \\ &\quad \sum_{\boldsymbol{x}_1,\boldsymbol{x}_2} \exp\!\left(\mathrm{i}\boldsymbol{x}_1\cdot\left(\frac{1}{2}\boldsymbol{p}_{\mathrm{cm}} + \hat{R}_{\mathrm{Ad}_{\bar{g}}(g)}\boldsymbol{q}\right) + \mathrm{i}\boldsymbol{x}_2\cdot\left(\frac{1}{2}\boldsymbol{p}_{\mathrm{cm}} - \hat{R}_{\mathrm{Ad}_{\bar{g}}(g)}\boldsymbol{q}\right)\right) \\ &\quad \left(\pi^{+\dagger}(\boldsymbol{x}_1)\,\pi^{-\dagger}(\boldsymbol{x}_2) - \pi^{-\dagger}(\boldsymbol{x}_1)\,\pi^{+\dagger}(\boldsymbol{x}_2)\right)\,.\end{aligned} \tag{3.29}$$

3.3.1 Set of ρ operators

To sum up the results of this chapter in Eq. (3.21) and Eq. (3.29) we found operators that coupled to the ρ channel. They form the set of operators $\vec{\mathcal{O}}^\alpha_\Gamma(\boldsymbol{p})$ from Sec. 2.6. We use two ρ operators which differ by the choice of γ^ρ and a number of $\pi\pi$ operators that are labeled by different $\boldsymbol{q}$. The exact number of which is different for each moving frame and irreducible representation and can be extracted from Tab. 3.5.

The correlation functions $\left\langle \vec{\mathcal{O}}^\alpha_\Gamma(\boldsymbol{p})\vec{\mathcal{O}}^\alpha_\Gamma(\boldsymbol{p})^\dagger\right\rangle_F$ are bilinear and may be therefore expressed in terms of the continuum operators $\rho_\gamma(\boldsymbol{x})$ and $\pi^+(\boldsymbol{x}_1)\pi^-(\boldsymbol{x}_2)$. This task boils down to factorizing lengthy analytical expressions. This was carried out automatically with a Python implementation.[2]

With this we reduced the correlation functions for all different moving frames and irreducible representations to a linear combination of just three terms. Namely, the ρ correlator $\left\langle\rho(y)\rho(x)^\dagger\right\rangle_F$, the $\pi\pi$ correlator $\left\langle\pi\pi(y,y')\pi\pi(x,x')^\dagger\right\rangle_F$ and the cross-term $\left\langle\pi\pi(y,y')\rho(x)^\dagger\right\rangle_F$.[3] All three are continuum quantities and live in position space. Their analytic calculation is the subject of the following chapter.

[1] Strictly speaking they obtain a factor (-1) under improper rotations but it always enters to the power of two and therefore cancels

[2] https://github.com/HISKP-LQCD/sLapH-projection

[3] The cross term is hermitian. Therefore specifying one of $\left\langle\pi\pi\ \rho^\dagger\right\rangle_F$ and $\left\langle\rho^\dagger\pi\pi^\dagger\right\rangle_F$ is sufficient.

CHAPTER 4

Wick contractions

4.1 Wick contractions

At this point we can conclude the discussion that started with the path integral in Sec. 2.2.2. We successfully seperated the fermionic from the gluonic degrees of freedom but deferred the calculation of fermionic expection values

$$\left\langle \mathcal{O}[\psi_1, \bar{\psi}_1, \dots \psi_{N_f}, \bar{\psi}_{N_f}, U] \right\rangle_F \tag{4.1}$$

by making use of Wick's theorem

$$\left\langle \eta_{i_1} \bar{\eta}_{j_1} \dots \eta_{i_n} \bar{\eta}_{j_n} \right\rangle_F = \sum_{\sigma \in \mathrm{S}_n} \mathrm{sign}(\sigma)\ D^{-1}_{i_1 j_{\sigma(1)}}\ D^{-1}_{i_2 j_{\sigma(2)}} D^{-1}_{i_n j_{\sigma(n)}} \,. \tag{2.52}$$

In the remainder of this thesis, the twisted basis is adopted. For ease of notation we adopt the shorthand notation

$$\chi_f(x)^c_\alpha \equiv f(x)_\alpha \tag{4.2}$$

where f denotes the quark flavor, the greek index is the Dirac component and the roman color index is suppressed as there is no color change in mesons.

To demonstrate Wick's theorem and introduce notation, the euclidean correlation function of a pion annihilation operator $\pi^+(x)$ and a pion creation operator $\pi^{+\dagger}(y) = \pi^-(y)$ is calculated. The pion operators introduced in Eq. (3.7) take the following shorthand form:

$$\pi^+(x) = \bar{d}(x)_\alpha \gamma_{\alpha\beta} u(x)_\beta \text{ or } \qquad \pi^-(x) = \bar{u}(x)_\alpha \gamma_{\alpha\beta} d(x)_\beta \,. \tag{4.3}$$

where repeated indices are summed over.

The correlation function therefore is the vacuum expectation value

$$\mathcal{C}_{\pi^+}(x|y) = \left\langle \pi^+(y)\ \pi^+(x)^\dagger \right\rangle_F = \left\langle \bar{d}(y)_\alpha \gamma_{\alpha\beta} u(y)_\beta \bar{u}(x)_\gamma \gamma_{\gamma\delta} d(x)_\delta \right\rangle_F \,. \tag{4.4}$$

The expectation value factorizes in flavor space. Therefore we group spinor and antispinors with

the same flavor together and obtain

$$\begin{aligned}
&\Big\langle \bar{d}(y)_\alpha \gamma_{\alpha\beta} u(y)_\beta \bar{u}(x)_\gamma \gamma_{\gamma\delta} d(x)_\delta \Big\rangle_F \\
&\quad = \gamma_{\alpha\beta}\gamma_{\gamma\delta} \left\langle u(y)_\beta \bar{u}(x)_\gamma \right\rangle_u (-)^3 \left\langle d(x)_\delta \bar{d}(y)_\alpha \right\rangle_d \\
&\quad = \gamma_{\alpha\beta}\gamma_{\gamma\delta} \left\langle u(y)_\beta \bar{u}(x)_\gamma \right\rangle_u (-)^3 \left\langle d(x)_\delta \bar{d}(y)_\alpha \right\rangle_d \\
&\quad = -\operatorname{tr}\left(\gamma D_u^{-1}(y|x)\gamma D_d^{-1}(x|y)\right) , \qquad (4.5)
\end{aligned}$$

where the trace acts only in Dirac space and we introduced the quark propagator for flavor f

$$D_f^{-1}(x|y) = f(x)\bar{f}(y) . \qquad (4.6)$$

The minus signs in Eq. (4.5) stem from anticommuting Grassmann numbers in position and flavor space. The square brackets are a convenient notation for the permutation $\sigma \in \mathrm{S}_n$ and indicate which quark fields are merged into a propagator. While for the charged pion only one permuation contributes, in general Wick's theorem yields a sum of multiple terms with very similar structure. All these terms consist of traces of propagators and operators. Calculations like in Eq. (4.5) are usually referred to as "Wick contraction" They can be visualized with quark

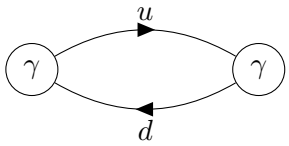

Figure 4.1: Quark line diagram for a charged pion correlation function.

flow diagrams. An operator is represented by a circle at some spacetime point and a propagator by a line connecting to different spacetime points and therefore operators. Pictorially Wick's theorem states, that the correlation function is the sum of all closed quark flow diagrams. The quark line diagram for Eq. (4.5) is depicted in Fig. 4.1.

4.1.1 Wick contractions for the ρ^0 meson

The result of the Wick contractions for the ρ channel are qualitatively different for different number of mesons involved. As explained in Sec. 3.3.1, the correlation functions in the Gevp belong to one of three classes: $\left\langle \rho\ \rho^\dagger \right\rangle$, $\left\langle \rho\ \pi\pi^\dagger \right\rangle$ and $\left\langle \pi\pi\ \pi\pi^\dagger \right\rangle$. According to the number of mesons involved, they will be named 2-point, 3-point and 4-point function respectively.[1] The purpose of this section is to perform the Wick contractions relevant for the ρ^0 meson and express the result in terms of quark line diagrams. In Chapter 3.2 the operators interpolating to ρ- and $\pi\pi$-states where presented. These constitute correlation functions.

[1] These terms are usually used for current insertion diagrams with operators at intermediate times $t_{\mathrm{so}} < t_{\mathrm{c}} < t_{\mathrm{si}}$. This is explicitly different here as two pions always are created or annihilated at the same time.

2-point function $\left\langle \rho\ \rho^\dagger \right\rangle$ The correlation function for creating and annihilating a ρ^0 meson is given by

$$\begin{aligned}
&\left\langle \rho(y)\rho(x)^\dagger \right\rangle_F \\
&= \frac{1}{2}\langle(\bar{u}(y)_\alpha \gamma^\rho_{\alpha\beta} u(y)_\beta - \bar{d}(y)_\alpha \gamma^\rho_{\alpha\beta} d(y)_\beta)(\bar{u}(x)_\gamma \gamma^\rho_{\gamma\delta} u(x)_\delta - \bar{d}(x)_\gamma \gamma^\rho_{\gamma\delta} d(x)_\delta)\rangle_F \\
&= \frac{1}{2}\Big(\langle \bar{u}(y)_\alpha \gamma^\rho_{\alpha\beta} u(y)_\beta \bar{u}(x)_\gamma \gamma^\rho_{\gamma\delta} u(x)_\delta\rangle_F - \langle \bar{u}(y)_\alpha \gamma^\rho_{\alpha\beta} u(y)_\beta \bar{d}(x)_\gamma \gamma^\rho_{\gamma\delta} d(x)_\delta\rangle_F \\
&\quad - \langle \bar{d}(y)_\alpha \gamma^\rho_{\alpha\beta} d(y)_\beta \bar{u}(x)_\gamma \gamma^\rho_{\gamma\delta} u(x)_\delta\rangle_F + \langle \bar{d}(y)_\alpha \gamma^\rho_{\alpha\beta} d(y)_\beta \bar{d}(x)_\gamma \gamma^\rho_{\gamma\delta} d(x)_\delta\rangle_F\Big)
\end{aligned} \tag{4.7}$$

According to Wick's theorem, this expression may be rewritten as the sum of all possible contractions. It suffices to calculate all contractions of the first two terms. The results for the third and forth term can be obtained from the former two by interchanging $u \leftrightarrow d$.

The first term has two non-vanishing contractions. The first one is

$$\begin{aligned}
&\gamma_{\alpha\beta}\gamma^\rho_{\gamma\delta}\langle \underbrace{\bar{u}(y)_\alpha u(y)_\beta}\, \underbrace{\bar{u}(x)_\gamma u(x)_\delta}\rangle_F \\
&= \gamma^\rho_{\alpha\beta}\gamma^\rho_{\gamma\delta}(-)\langle u(y)_\beta \bar{u}(y)_\alpha\rangle_F (-)\langle u(x)_\delta \bar{u}(x)_\gamma\rangle_F \\
&= \gamma^\rho_{\alpha\beta}\gamma^\rho_{\gamma\delta} D_u^{-1}(y|y)_{\beta\alpha} D_u^{-1}(x|x)_{\delta\gamma} \\
&= \mathrm{tr}\Big(\gamma^\rho D_u^{-1}(y|y)\Big)\cdot \mathrm{tr}\Big(\gamma^\rho D_u^{-1}(x|x)\Big)\,.
\end{aligned} \tag{4.8}$$

This is called a "disconnnected contribution". The origin of this term becomes clear when

Figure 4.2: Quark line diagram the disconnected piece of a ρ correlation function.

looking at the quark flow diagram depicted in Fig. 4.2. There are no quark lines connecting the source to the sink site.[2]

The second contraction is the "connecting contribution". The calculation is analog to the derivation of Eq. (4.5). The connected piece is

$$\begin{aligned}
&\gamma_{\alpha\beta}\gamma^\rho_{\gamma\delta}\langle \underbrace{\bar{u}(y)_\alpha \underbrace{u(y)_\beta \bar{u}(x)_\gamma}\, u(x)_\delta}\rangle_F \\
&= -\,\mathrm{tr}\Big(\gamma^\rho D_u^{-1}(y|x)\gamma^\rho D_u^{-1}(x|y)\Big)\,.
\end{aligned} \tag{4.9}$$

For the remaining contractions intermediate steps will be omitted and only the final results given. While all calculations were performed by hand, they where verified with the QCT quark contraction tool implemented in Mathematica.[81]

[2] A more precise term would be fermionic disconnected as the sites are of course still connected by the gluon field

Conjoined, Wick's theorem for the first term of Eq. (4.7) reads

$$\begin{aligned}&\langle \bar{u}(y)_\alpha \gamma^\rho_{\alpha\beta} u(y)_\beta \bar{u}(x)_\gamma \gamma^\rho_{\gamma\delta} u(x)_\delta \rangle_F \\ &\quad = \mathrm{tr}\Big(\gamma^\rho D_u^{-1}(y|y)\Big)\,\mathrm{tr}\Big(\gamma^\rho D_u^{-1}(x|x)\Big) - \mathrm{tr}\Big(\gamma^\rho D_u^{-1}(y|x)\gamma^\rho D_u^{-1}(x|y)\Big)\,.\end{aligned} \tag{4.10}$$

The second term of Eq. (4.7) only has one non-vanishing Wick contraction

$$\begin{aligned}&\langle \bar{u}(y)_\alpha \gamma^\rho_{\alpha\beta} u(y)_\beta \bar{d}(x)_\gamma \gamma^\rho_{\gamma\delta} d(x)_\delta \rangle_F \qquad (4.11)\\ &\quad = \gamma_{\alpha\beta}\gamma^\rho_{\gamma\delta} \langle \bar{u}(y)_\alpha \underbrace{u(y)_\beta \bar{d}(x)_\gamma} d(x)_\delta \rangle_F \\ &= \mathrm{tr}\Big(\gamma^\rho D_u^{-1}(y|y)\Big)\cdot \mathrm{tr}\Big(\gamma^\rho D_d^{-1}(x|x)\Big)\,. \qquad (4.12)\end{aligned}$$

Because the light flavors are degenerate in the action Eq. (2.45), γ_5-hermiticity holds and the d-quark propagators may be expressed by

$$D_d^{-1}(y|x) = \gamma_5 D_u^{-1}(x|y)^\dagger \gamma_5 \tag{4.13}$$

and Eq. (4.12) becomes

$$\langle \bar{u}(y)_\alpha \gamma_{\alpha\beta} u(y)_\beta \bar{d}(x)_\gamma \gamma_{\gamma\delta} d(x)_\delta \rangle_F = \mathrm{tr}\Big(\gamma^\rho D_u^{-1}(y|y)\Big)\cdot \mathrm{tr}\Big(\gamma^\rho \gamma_5 D_u^{-1}(x|x)^\dagger \gamma_5\Big) \tag{4.14}$$

which is the same as Eq. (4.8) up to a possible sign.

Using Eq. (4.8) - Eq. (4.14) the complete correlation function may be expressed as

$$\begin{aligned}&\langle \rho(y)\rho(x)^\dagger \rangle_F \\ &\quad = -\frac{1}{2}\Big(\mathrm{tr}\Big(\gamma^\rho D_u^{-1}(x|x)\Big) - \mathrm{tr}\Big(\gamma^\rho\gamma_5 D_u^{-1}(x|x)^\dagger\gamma_5\Big)\Big)\Big(\mathrm{tr}\Big(\gamma^\rho D_u^{-1}(y|y)\Big) - \mathrm{tr}\Big(\gamma^\rho\gamma_5 D_u^{-1}(y|y)^\dagger\gamma_5\Big)\Big) \\ &\qquad + \frac{1}{2}\Big(\mathrm{tr}\Big(\gamma^\rho\gamma_5 D_u^{-1}(y|x)^\dagger\gamma_5\gamma^\rho\gamma_5 D_u^{-1}(x|y)^\dagger\gamma_5\Big) + \mathrm{tr}\Big(\gamma^\rho D_u^{-1}(y|x)\gamma^\rho D_u^{-1}(x|y)\Big)\Big)\end{aligned} \tag{4.15}$$

The correlation function may be further simplified for a fixed choice for γ^ρ. Let $\gamma^\rho = \gamma^m$ as defined in Eq. (3.12). Then

$$\gamma_5 \gamma^m \gamma_5 = -\gamma^m$$

and because $\gamma^{m\dagger} = \gamma^m$ the terms in Eq. (4.15) become complex conjugates.

$$\begin{aligned}\Big\langle \rho(y)\ \rho(x)^\dagger \Big\rangle_F &= \frac{1}{2}\,\mathrm{tr}\Big(\gamma^m \cdot D_u^{-1}(y|x)^\dagger \cdot \gamma^m \cdot D_u^{-1}(x|y)^\dagger\Big) \\ &\qquad + \frac{1}{2}\,\mathrm{tr}\Big(\gamma^m \cdot D_u^{-1}(y|x) \cdot \gamma^m \cdot D_u^{-1}(x|y)\Big) \\ &= \frac{1}{2}\Big(\mathrm{tr}\Big(\gamma^m \cdot D_u^{-1}(y|x) \cdot \gamma^m \cdot D_u^{-1}(x|y)\Big) + \text{h. c.}\Big) \\ &= \mathrm{Re}\,\mathrm{tr}\Big(\gamma^m \cdot D_u^{-1}(y|x) \cdot \gamma^m \cdot D_u^{-1}(x|y)\Big) \qquad (4.16)\\ &= \mathrm{Re}\{(\text{C2n})\} \qquad (4.17)\end{aligned}$$

where disconnected diagrams where neglected.

The term C2n introduced in the end is a short hand notation for the connected 2-point function with identical flavors. For different ρ operators the quark flow will be the same and only the Dirac struct must be replaced. More on the different types of quark flow diagrams can be found in Sec. A.4.

For ρ_{50m} and cross correlators, the calculations are analog, but as

$$\gamma_5\gamma_5\gamma_0\gamma^m\gamma_5 = +\gamma_5\gamma_0\gamma^m$$

several signs changes must be taken into account. The result is:

$$\langle\rho_{50m}(y)\rho_{50m}(x)^\dagger\rangle_F = \mathrm{Re(C2n)} \tag{4.18}$$

$$\langle\rho_{50m}(y)\rho_m(x)^\dagger\rangle_F = \mathrm{Im(C2n)} \tag{4.19}$$

$$\langle\rho_m(y)\rho_{50m}(x)^\dagger\rangle_F = -\mathrm{Im(C2n)} \tag{4.20}$$

3-point function $\left\langle \pi\pi\ \rho^\dagger \right\rangle$ With the two-pion operator from Eq. (3.9) the correlation function is

$$\begin{aligned}
&\left\langle \pi\pi(y,y')\rho(x)^\dagger \right\rangle_F \\
&= \frac{1}{2}\Big\langle \Big(\bar d(y)_\alpha\gamma^\pi_{\alpha\beta}u(y)_\beta\bar u(y')_\gamma\gamma^\pi_{\gamma\delta}d(y')_\delta - \bar u(y)_\alpha\gamma^\pi_{\alpha\beta}d(y)_\beta\bar d(y')_\gamma\gamma^\pi_{\gamma\delta}u(y')_\delta\Big) \\
&\qquad \Big(\bar u(x)_\varepsilon\gamma^\rho_{\varepsilon\zeta}u(x)_\zeta - \bar d(x)_\varepsilon\gamma^\rho_{\varepsilon\zeta}d(x)_\zeta\Big)\Big\rangle_F \\
&= \frac{1}{2}\Big(\Big\langle \bar d(y)_\alpha\gamma^\pi_{\alpha\beta}u(y)_\beta\bar u(y')_\gamma\gamma^\pi_{\gamma\delta}d(y')_\delta\bar u(x)_\varepsilon\gamma^\rho_{\varepsilon\zeta}u(x)_\zeta\Big\rangle_F \\
&\qquad - \Big\langle \bar d(y)_\alpha\gamma^\pi_{\alpha\beta}u(y)_\beta\bar u(y')_\gamma\gamma^\pi_{\gamma\delta}d(y')_\delta\bar d(x)_\varepsilon\gamma^\rho_{\varepsilon\zeta}d(x)_\zeta\Big\rangle_F \\
&\qquad - \Big\langle \bar u(y)_\alpha\gamma^\pi_{\alpha\beta}d(y)_\beta\bar d(y')_\gamma\gamma^\pi_{\gamma\delta}u(y')_\delta\bar u(x)_\varepsilon\gamma^\rho_{\varepsilon\zeta}u(x)_\zeta\Big\rangle_F \\
&\qquad + \Big\langle \bar u(y)_\alpha\gamma^\pi_{\alpha\beta}d(y)_\beta\bar d(y')_\gamma\gamma^\pi_{\gamma\delta}u(y')_\delta\bar d(x)_\varepsilon\gamma^\rho_{\varepsilon\zeta}d(x)_\zeta\Big\rangle_F\Big)
\end{aligned} \tag{4.21}$$

where we already inserted γ^5 for the pion operators. The Wick contractions for the first term again yield a disconnected and a connected part. The disconnected diagram is

$$\begin{aligned}
&\gamma^\pi_{\alpha\beta}\gamma^\pi_{\gamma\delta}\gamma^\rho_{\varepsilon\zeta}\Big\langle \underbrace{\bar d(y)_\alpha}\,\underbrace{u(y)_\beta}\,\underbrace{\bar u(y')_\gamma}\,\underbrace{d(y')_\delta}\,\underbrace{\bar u(x)_\varepsilon}\,\underbrace{u(x)_\zeta}\Big\rangle_F \\
&\qquad = \mathrm{tr}\Big(\gamma^\pi D_u^{-1}(y|y')\gamma^\pi D_d^{-1}(y'|y)\Big)\,\mathrm{tr}\Big(\gamma^\rho D_u^{-1}(x|x)\Big)
\end{aligned} \tag{4.22}$$

and the connected

$$\begin{aligned}
&\gamma^\pi_{\alpha\beta}\gamma^\pi_{\gamma\delta}\gamma^\rho_{\varepsilon\zeta}\Big\langle \underbrace{\bar d(y)_\alpha}\,\underbrace{u(y)_\beta}\,\underbrace{\bar u(y')_\gamma}\,\underbrace{d(y')_\delta}\,\underbrace{\bar u(x)_\varepsilon}\,\underbrace{u(x)_\zeta}\Big\rangle_F \\
&\qquad = -\,\mathrm{tr}\Big(\gamma^\pi D_u^{-1}(y|x)\gamma^\rho D_u^{-1}(x|y')\gamma^\pi D_d^{-1}(y'|y)\Big)\,.
\end{aligned} \tag{4.23}$$

Similar to the 2-point function the Wick contractions for all other terms can be obtained from the first term by interchanging $u \leftrightarrow d$, $y \leftrightarrow y'$ or both. The complete correlation function (neglecting disconnected contributions) is

$$\begin{aligned}
&\left\langle \pi\pi(y,y')\rho(x)^\dagger \right\rangle_F \\
&\quad = -\frac{1}{2}\Big(\mathrm{tr}\Big(\gamma^\pi D_u^{-1}(y|x)\gamma^\rho D_u^{-1}(x|y')\gamma^\pi D_d^{-1}(y'|y)\Big) \\
&\qquad - \mathrm{tr}\Big(\gamma^\pi D_d^{-1}(y'|x)\gamma^\rho D_d^{-1}(x|y)\gamma^\pi D_u^{-1}(y|y')\Big) \\
&\qquad - \mathrm{tr}\Big(\gamma^\pi D_u^{-1}(y'|x)\gamma^\rho D_u^{-1}(x|y)\gamma^\pi D_d^{-1}(y|y')\Big) \\
&\qquad + \mathrm{tr}\Big(\gamma^\pi D_d^{-1}(y|x)\gamma^\rho D_d^{-1}(x|y')\gamma^\pi D_u^{-1}(y'|y)\Big)\Big)
\end{aligned} \tag{4.24}$$

This expression can again be simplified with γ_5-hermiticity upon choosing a Dirac structure. With $\gamma^\pi = \mathrm{i}\gamma^5$ the result is

$$\left\langle \pi\pi(y,y')\rho_m(x)^\dagger \right\rangle_F \tag{4.25}$$

$$= -\frac{1}{2}\Big(\mathrm{tr}\Big(\mathrm{i}\gamma^5 D_u^{-1}(y|x)\gamma^m D_u^{-1}(x|y')\mathrm{i}\gamma^5\gamma_5 D_u^{-1}(y|y')^\dagger\gamma_5\Big) - \text{h. c.} \tag{4.26}$$

$$- \mathrm{tr}\Big(\mathrm{i}\gamma^5 D_u^{-1}(y'|x)\gamma^m D_u^{-1}(x|y)\mathrm{i}\gamma^5\gamma_5 D_u^{-1}(y'|y)^\dagger\gamma_5\Big) + \text{h. c.} \tag{4.27}$$

$$= \mathrm{i}\,\mathrm{Im}(\mathrm{C3c}(y,\gamma^5;x,\gamma^m;y',\gamma^5)) - \mathrm{i}\,\mathrm{Im}(\mathrm{C3c}(y',\gamma^5;x,\gamma^m;y,\gamma^5)) \tag{4.28}$$

for ρ_m and

$$\left\langle \pi\pi(y,y')\rho_{50m}(x)^\dagger \right\rangle_F \tag{4.29}$$

$$= -\,\mathrm{Re}(\mathrm{C3c}(y,\gamma^5;x,\gamma^5\gamma^0\gamma^m;y',\gamma^5)) + \mathrm{Re}(\mathrm{C3c}(y',\gamma^5;x,\gamma^5\gamma^0\gamma^m;y,\gamma^5)) \tag{4.30}$$

for ρ_{50m}.

4-point function $\left\langle \pi\pi\ \pi\pi^\dagger \right\rangle$ The correlation function for creating and subsequently annihilating two pions has four terms.

$$\begin{aligned}
&\left\langle \pi\pi(y,y')\pi\pi(x,x')^\dagger \right\rangle_F \\
&\quad = \frac{1}{2}\Big(\left\langle \pi^+\pi^-(y,y')\pi^+\pi^-(x,x')^\dagger \right\rangle_F - \left\langle \pi^+\pi^-(y,y')\pi^+\pi^-(x',x)^\dagger \right\rangle_F \\
&\qquad - \left\langle \pi^+\pi^-(y',y)\pi^+\pi^-(x,x')^\dagger \right\rangle_F + \left\langle \pi^+\pi^-(y',y)\pi^+\pi^-(x',x)^\dagger \right\rangle_F\Big)
\end{aligned} \tag{4.31}$$

Again all contractions may be generated from the first by substituting $x \leftrightarrow x'$, $y \leftrightarrow y'$ or both. Expressed by quark fields, the first term is

$$\begin{aligned}
&\left\langle \pi^+\pi^- \right\rangle (y,y')\ \pi^+\pi^-(x,x')^\dagger\rangle_F \\
&\quad = \left\langle \bar d(y)_\alpha \mathrm{i}\gamma^5_{\alpha\beta} u(y)_\beta \bar u(y')_\gamma \mathrm{i}\gamma^5_{\gamma\delta} d(y')_\delta \bar u(x)_\varepsilon \mathrm{i}\gamma^5_{\varepsilon\zeta} d(x)_\zeta \bar d(x')_\eta \mathrm{i}\gamma^5_{\eta\vartheta} u(x')_\vartheta \right\rangle_F \\
&\quad = \gamma^5_{\alpha\beta}\gamma^5_{\gamma\delta}\gamma^5_{\varepsilon\zeta}\gamma^5_{\eta\vartheta} \left\langle \bar d(y)_\alpha u(y)_\beta \bar u(y')_\gamma d(y')_\delta \bar u(x)_\varepsilon d(x)_\zeta \bar d(x')_\eta u(x')_\vartheta \right\rangle_F
\end{aligned} \tag{4.32}$$

where again γ^5 was already assumed.

Due to the increased number of quark fields, there are four non-vanishing Wick contractions. They are

$$\begin{aligned}
&\gamma^5_{\alpha\beta}\gamma^5_{\gamma\delta}\gamma^5_{\varepsilon\zeta}\gamma^5_{\eta\vartheta}\,\Big\langle \bar{d}(y)_\alpha u(y)_\beta \bar{u}(y')_\gamma d(y')_\delta \bar{u}(x)_\varepsilon d(x)_\zeta \bar{d}(x')_\eta u(x')_\vartheta \Big\rangle_F \\
&\quad = -\operatorname{tr}\Big(\gamma^5 D_u^{-1}(y|y')\gamma^5 D_d^{-1}(y'|x')\gamma^5 D_u^{-1}(x'|x)\gamma^5 D_d^{-1}(x|y)\Big) \\
&\quad = -\operatorname{tr}\Big(\gamma^5 D_u^{-1}(y|y')\gamma^5\gamma^5 D_u^{-1}(x'|y')^\dagger\gamma^5\gamma^5 D_u^{-1}(x'|x)\gamma^5\gamma^5 D_u^{-1}(y|x)^\dagger\gamma^5\Big)\,,
\end{aligned} \tag{4.33}$$

$$\begin{aligned}
&\gamma^5_{\alpha\beta}\gamma^5_{\gamma\delta}\gamma^5_{\varepsilon\zeta}\gamma^5_{\eta\vartheta}\,\Big\langle \bar{d}(y)_\alpha u(y)_\beta \bar{u}(y')_\gamma d(y')_\delta \bar{u}(x)_\varepsilon d(x)_\zeta \bar{d}(x')_\eta u(x')_\vartheta \Big\rangle_F \\
&\quad = \operatorname{tr}\Big(\gamma^5 D_u^{-1}(y|x)\gamma^5 D_d^{-1}(x|y)\Big)\cdot\operatorname{tr}\Big(\gamma^5 D_u^{-1}(x'|y')\gamma^5 D_d^{-1}(y'|x')\Big) \\
&\quad = \operatorname{tr}\Big(\gamma^5 D_u^{-1}(y|x)\gamma^5\gamma^5 D_u^{-1}(y|x)^\dagger\gamma^5\Big)\cdot\operatorname{tr}\Big(\gamma^5 D_u^{-1}(x'|y')\gamma^5\gamma^5 D_u^{-1}(x'|y')^\dagger\gamma^5\Big)\,,
\end{aligned} \tag{4.34}$$

$$\begin{aligned}
&\gamma^5_{\alpha\beta}\gamma^5_{\gamma\delta}\gamma^5_{\varepsilon\zeta}\gamma^5_{\eta\vartheta}\,\Big\langle \bar{d}(y)_\alpha u(y)_\beta \bar{u}(y')_\gamma d(y')_\delta \bar{u}(x)_\varepsilon d(x)_\zeta \bar{d}(x')_\eta u(x')_\vartheta \Big\rangle_F \\
&\quad = \operatorname{tr}\Big(\gamma^5 D_u^{-1}(y|y')\gamma^5 D_d^{-1}(y'|y)\Big)\cdot\operatorname{tr}\Big(\gamma^5 D_u^{-1}(x'|x)\gamma^5 D_d^{-1}(x|x')\Big) \\
&\quad = \operatorname{tr}\Big(\gamma^5 D_u^{-1}(y|y')\gamma^5\gamma^5 D_u^{-1}(y|y')^\dagger\gamma^5\Big)\cdot\operatorname{tr}\Big(\gamma^5 D_u^{-1}(x'|x)\gamma^5\gamma^5 D_u^{-1}(x'|x)^\dagger\gamma^5\Big)
\end{aligned} \tag{4.35}$$

and

$$\begin{aligned}
&\gamma^5_{\alpha\beta}\gamma^5_{\gamma\delta}\gamma^5_{\varepsilon\zeta}\gamma^5_{\eta\vartheta}\,\Big\langle \bar{d}(y)_\alpha u(y)_\beta \bar{u}(y')_\gamma d(y')_\delta \bar{u}(x)_\varepsilon d(x)_\zeta \bar{d}(x')_\eta u(x')_\vartheta \Big\rangle_F \\
&\quad = -\operatorname{tr}\Big(\gamma^5 D_u^{-1}(y|x)\gamma^5 D_d^{-1}(x|x')\gamma^5 D_u^{-1}(x'|y')\gamma^5 D_d^{-1}(y'|y)\Big) \\
&\quad = -\operatorname{tr}\Big(\gamma^5 D_u^{-1}(y|x)\gamma^5\gamma^5 D_u^{-1}(x'|x)^\dagger\gamma^5\gamma^5 D_u^{-1}(x'|y')\gamma^5\gamma^5 D_u^{-1}(y|y')^\dagger\gamma^5\Big)\,.
\end{aligned} \tag{4.36}$$

When all terms in Eq. (4.31) are combined in addtition to the complex hermitian conjugate, also the transpose and complex conjugate appear for each of the terms Eq. (4.33)-(4.36). The latter two topologically give the same quark flow diagrams but the sites are permuted. Eq. (4.35) is a disconnected contribution and will be again neglected. Furthermore Eq. (4.33) and Eq. (4.36)

are already hermitian conjugates, they give the same contribution. The final result is

$$\begin{aligned}
&\Big\langle \pi\pi(y,y')\ \pi\pi(x,x')^\dagger \Big\rangle_F \\
&\quad= \frac{1}{2}\Big(\mathrm{tr}\Big(\gamma^5 D_u^{-1}(y|x)\gamma^5\gamma^5 D_u^{-1}(y|x)^\dagger\gamma^5\Big)\cdot \mathrm{tr}\Big(\gamma^5 D_u^{-1}(x'|y')\gamma^5\gamma^5 D_u^{-1}(x'|y')^\dagger\gamma^5\Big) + \text{h. c.} \\
&\qquad - 2\Big(\mathrm{tr}\Big(\gamma^5 D_u^{-1}(y|x)\gamma^5\gamma^5 D_u^{-1}(x'|x)^\dagger\gamma^5\gamma^5 D_u^{-1}(x'|y')\gamma^5\gamma^5 D_u^{-1}(y|y')^\dagger\gamma^5\Big) + \text{h. c.}\Big) \\
&\qquad + \mathrm{tr}\Big(\gamma^5 D_u^{-1}(y'|x)\gamma^5\gamma^5 D_u^{-1}(y'|x)^\dagger\gamma^5\Big)\cdot \mathrm{tr}\Big(\gamma^5 D_u^{-1}(x'|y)\gamma^5\gamma^5 D_u^{-1}(x'|y)^\dagger\gamma^5\Big) + \text{h. c.} \\
&\qquad - 2\Big(\mathrm{tr}\Big(\gamma^5 D_u^{-1}(y'|x)\gamma^5\gamma^5 D_u^{-1}(x'|x)^\dagger\gamma^5\gamma^5 D_u^{-1}(x'|y)\gamma^5\gamma^5 D_u^{-1}(y'|y)^\dagger\gamma^5\Big) + \text{h. c.}\Big)\Big) \\
&\quad= 2\,\mathrm{Re}(\mathrm{C4cD}(y,\gamma^5;x,\gamma^5;x',\gamma^5;y',\gamma^5)) - 4\,\mathrm{Re}(\mathrm{C4cB}(y,\gamma^5;x,\gamma^5;x',\gamma^5;y',\gamma^5)) \\
&\qquad + 2\,\mathrm{Re}(\mathrm{C4cD}(y',\gamma^5;x,\gamma^5;x',\gamma^5;y,\gamma^5)) - 4\,\mathrm{Re}(\mathrm{C4cB}(y',\gamma^5;x,\gamma^5;x',\gamma^5;y,\gamma^5))
\end{aligned} \tag{4.37}$$

4.1.2 Thermal states

If at least two particles are involved, certain terms in the spectral decomposition pose non-negligible artifacts even though they vanish in the infinite-T limit. These are called "thermal states".

A correlation function may generally be expressed as

$$C(t) = \Big\langle \mathcal{O}_{\mathrm{si}}(t)\ \mathcal{O}_{\mathrm{so}}(0)^\dagger \Big\rangle = \sum_{m,n} \mathrm{e}^{-E_n T}\mathrm{e}^{-(E_m-E_n)t}\ \langle n|\mathcal{O}_{\mathrm{si}}(0)|m\rangle\ \langle m|\mathcal{O}_{\mathrm{so}}(0)^\dagger|n\rangle \tag{4.38}$$

by inserting of a complete set of states and using the time evolution operator. Higher asymptotic states n are usually neglected as all but $|n\rangle = |0\rangle$ vanish in the limit $T \to \infty$. In this case E_n is simply the vacuum energy and on arrives at Eq. (2.120).

For the $\pi\pi$ operators defined in Eq. (3.9) however, this assumption is no longer justified. The lightest states n may assume are $|\ \pi\rangle$ and $|\ \pi\pi\rangle$. On the ensembles of Tab. 5.1 states involving at least three pions in the initial or final state are so much suppressed by the factor $\exp(-E_n T)$ that they may still be safely neglected. As we already argued in Chap. 3 the lattice operator Eq. (3.29) may be decomposed into linear combinations of continuum operators. Therefore the calculation may be tremendously simplified by looking at the non-isospin projected continuum operator in momentum space. The lowest orders of Eq. (4.38) for $\mathcal{O}_{\mathrm{si}} = \pi^+\pi^-(t;\boldsymbol{p}_1,\boldsymbol{p}_2)$ and

$\mathcal{O}_{\text{so}} = \pi^+\pi^-(t; \boldsymbol{p}_1', \boldsymbol{p}_2')^\dagger$ are

$$\begin{aligned} C(t) = \sum_m \Big(& \mathrm{e}^{-E_0 T}\mathrm{e}^{-(E_m - E_0)t} \langle 0 \mid \pi^+(\boldsymbol{p}_1')\pi^-(\boldsymbol{p}_2') \mid m\rangle \langle m \mid \pi^+(\boldsymbol{p}_2)\pi^-(\boldsymbol{p}_1) \mid 0\rangle \\ & + \mathrm{e}^{-E_\pi T}\mathrm{e}^{-(E_m - E_\pi)t} \left\langle \pi^+ \,\middle|\, \pi^+(\boldsymbol{p}_1')\pi^-(\boldsymbol{p}_2') \,\middle|\, m \right\rangle \left\langle m \,\middle|\, \pi^+(\boldsymbol{p}_2)\pi^-(\boldsymbol{p}_1) \,\middle|\, \pi^+ \right\rangle \\ & + \mathrm{e}^{-E_\pi T}\mathrm{e}^{-(E_m - E_\pi)t} \left\langle \pi^- \,\middle|\, \pi^+(\boldsymbol{p}_1')\pi^-(\boldsymbol{p}_2') \,\middle|\, m \right\rangle \left\langle m \,\middle|\, \pi^+(\boldsymbol{p}_2)\pi^-(\boldsymbol{p}_1) \,\middle|\, \pi^- \right\rangle \\ & + \mathrm{e}^{-E_{\pi\pi} T}\mathrm{e}^{-(E_m - E_{\pi\pi})t} \left\langle \pi^+\pi^+ \,\middle|\, \pi^+(\boldsymbol{p}_1')\pi^-(\boldsymbol{p}_2') \,\middle|\, m \right\rangle \left\langle m \,\middle|\, \pi^+(\boldsymbol{p}_2)\pi^-(\boldsymbol{p}_1) \,\middle|\, \pi^+\pi^+ \right\rangle \\ & + \mathrm{e}^{-E_{\pi\pi} T}\mathrm{e}^{-(E_m - E_{\pi\pi})t} \left\langle \pi^+\pi^- \,\middle|\, \pi^+(\boldsymbol{p}_1')\pi^-(\boldsymbol{p}_2') \,\middle|\, m \right\rangle \left\langle m \,\middle|\, \pi^+(\boldsymbol{p}_2)\pi^-(\boldsymbol{p}_1) \,\middle|\, \pi^+\pi^- \right\rangle \\ & + \mathrm{e}^{-E_{\pi\pi} T}\mathrm{e}^{-(E_m - E_{\pi\pi})t} \left\langle \pi^-\pi^- \,\middle|\, \pi^+(\boldsymbol{p}_1')\pi^-(\boldsymbol{p}_2') \,\middle|\, m \right\rangle \left\langle m \,\middle|\, \pi^+(\boldsymbol{p}_2)\pi^-(\boldsymbol{p}_1) \,\middle|\, \pi^-\pi^- \right\rangle \Big) \\ & + \mathcal{O}(3\pi) \end{aligned} \tag{4.39}$$

The exponentials e^{-ET} serve as a suppression factor. Terms within the spectral composition with at least three particles are completely negligible. The same is true for terms with involve at least two pions in both the asymptotic and intermediate state. The functional behavior when $\mid n\rangle = \mid m\rangle = \left\mid \pi^\pm\pi^\pm \right\rangle$ is the same as from $\mid n\rangle = \mid m\rangle = \left\mid \pi^\pm \right\rangle$ barring an additional spectator pion. This causes a suppression by $\mathrm{e}^{-M_\pi T}$ which is in the order of 10^{-3}.

From Eq. (4.39) four relevant terms remain. In this work the exact form of the amplitude is not relevant and therefore not given explicitly.

The first term of Eq. (4.39) behaves like

$$\begin{aligned} & \sum_m \mathrm{e}^{-E_0 T}\mathrm{e}^{-(E_m - E_0)t} \langle 0 \mid \pi^+(\boldsymbol{p}_1')\pi^-(\boldsymbol{p}_2') \mid m\rangle \langle m \mid \pi^+(\boldsymbol{p}_2)\pi^-(\boldsymbol{p}_1) \mid 0\rangle \\ & \qquad \propto 2\mathrm{e}^{-E_0 T} + \mathrm{e}^{-E_0 T} \sum_m \mathrm{e}^{-(E_{\pi\pi}^m - E_0)t} \delta_{\boldsymbol{p}_1\boldsymbol{p}_1'} \delta_{\boldsymbol{p}_2\boldsymbol{p}_2'} \end{aligned} \tag{4.40}$$

The first term vacuum expectation value and cancels in the projection to definite isospin. The second term is often called "physical contribution" as it is the only one to survive in the limit $\lim_{T\to\infty}$.

The second and third term of Eq. (4.39) are almost identical.

$$\begin{aligned} & \sum_m \mathrm{e}^{-E_\pi T}\mathrm{e}^{-(E_m - E_\pi)t} \left\langle \pi^+ \,\middle|\, \pi^+(\boldsymbol{p}_1')\pi^-(\boldsymbol{p}_2') \,\middle|\, m \right\rangle \left\langle m \,\middle|\, \pi^+(\boldsymbol{p}_2)\pi^-(\boldsymbol{p}_1) \,\middle|\, \pi^+ \right\rangle \\ & \qquad \propto \mathrm{e}^{-E_\pi(\boldsymbol{p}_1)T}\mathrm{e}^{-(E_\pi(\boldsymbol{p}_2) - E_\pi(\boldsymbol{p}_1))t} \delta_{\boldsymbol{p}_1\boldsymbol{p}_1'} \delta_{\boldsymbol{p}_2\boldsymbol{p}_2'} + \mathcal{O}(3\pi) \end{aligned} \tag{4.41}$$

$$\begin{aligned} & \sum_m \mathrm{e}^{-E_\pi T}\mathrm{e}^{-(E_m - E_\pi)t} \left\langle \pi^- \,\middle|\, \pi^+(\boldsymbol{p}_1')\pi^-(\boldsymbol{p}_2') \,\middle|\, m \right\rangle \left\langle m \,\middle|\, \pi^+(\boldsymbol{p}_2)\pi^-(\boldsymbol{p}_1) \,\middle|\, \pi^- \right\rangle \\ & \qquad \propto \mathrm{e}^{-E_\pi(\boldsymbol{p}_2)T}\mathrm{e}^{-(E_\pi(\boldsymbol{p}_1) - E_\pi(\boldsymbol{p}_2))t} \delta_{\boldsymbol{p}_1\boldsymbol{p}_1'} \delta_{\boldsymbol{p}_2\boldsymbol{p}_2'} + \mathcal{O}(3\pi) \end{aligned} \tag{4.42}$$

The only difference is the sign of the second exponential as the momenta are interchanged. The projection to definite isospin Eq. (3.9) contains both permutations. As one might suspect the charge of the pion has no influence on the thermal state in theory with degenerate charged pions.

The forth and sixth term of Eq. (4.39) both require at least two pions in the intermediate

state. Therefore the final relevant term is

$$\begin{aligned}\sum_m \mathrm{e}^{-E_{\pi\pi}T}\mathrm{e}^{-(E_m-E_{\pi\pi})t}\left\langle \pi^+\pi^- \,\middle|\, \pi^+(\boldsymbol{p}_1')\pi^-(\boldsymbol{p}_2') \,\middle|\, m\right\rangle\left\langle m \,\middle|\, \pi^+(\boldsymbol{p}_2)\pi^-(\boldsymbol{p}_1) \,\middle|\, \pi^+\pi^-\right\rangle \\ \propto 2\mathrm{e}^{-(E_\pi(\boldsymbol{p}_1')+E_\pi(\boldsymbol{p}_1))T} + \sum_m \mathrm{e}^{-E^m_{\pi\pi}T}\mathrm{e}^{-(E_0-E^m_{\pi\pi})t}\delta_{\boldsymbol{p}_1\boldsymbol{p}_1'}\delta_{\boldsymbol{p}_2\boldsymbol{p}_2'} + \mathcal{O}(2\pi)\end{aligned} \tag{4.43}$$

Like in Eq. (4.40) the first term is a vacuum expectation value that cancels in the projection to definite isospin. The second term structurally very much resembles the physical contribution. Because the lattice has periodic boundary conditions in time there is no restriction for the propagator to only run forward in time. The second term is the "backpropagating part".

In one-particle correlation functions states like Eq. (4.41)-Eq. (4.42) do not appear. In this case Eq. (4.43) may be accounted for analytically. Together with the physical contribution the functional dependence may be expressed as

$$C(t) \propto 2\mathrm{e}^{-(E^0_{\pi\pi}-E_0)T/2}\cosh\Big((E^0_{\pi\pi}-E_0)(T/2-t)\Big)\,. \tag{4.44}$$

For small t the cosh is dominated by a single exponential. Around $T/2$ however, the backpropagating part is starting to become more relevant and for large t the cosh is again dominated by a single exponential with positive sign. The contributions are (anti-)symmetrical under $t \leftrightarrow T/2-t$. Therefore we average the forward and backward parts to gain statistics. The trait that the single exponential must be altered only at $t \approx T/2$ i.e. the end of the signal is typical of thermal states.

The final operator in Eq. (3.29) was projected to definite isospin as well a certain moving frame momentum $\boldsymbol{p}_{\mathrm{cm}}$ and irrep Γ thereof. That certain terms cancel in the projection to definite isospin has already been mentioned above. Additionally there is a dependence of the thermal states on $\boldsymbol{p}_{\mathrm{cm}}$ and Γ because the momentum combinations $\boldsymbol{p}_1, \boldsymbol{p}_2$ listed in Tab. 3.5 survive the projection are not projected to 0. With the momenta also $E_\pi(\boldsymbol{p}_1), E_\pi(\boldsymbol{p}_2)$ and therefore the thermal states are different for each $\boldsymbol{p}^2_{\mathrm{cm}}$ and Γ.

4.1.3 Weighting and Shifting

There are multiple ways to account for the lattice artifacts from thermal states [21, 82]. We will show numerically in Sec. 6.2 that

$$\varepsilon_t(t, \boldsymbol{p}_1, \boldsymbol{p}_2) \;\propto\; \mathrm{e}^{-E_\pi(\boldsymbol{p}_1)T}\mathrm{e}^{-(E_\pi(\boldsymbol{p}_2)-E_\pi(\boldsymbol{p}_1))t} + \mathrm{e}^{-E_\pi(\boldsymbol{p}_2)T}\mathrm{e}^{-(E_\pi(\boldsymbol{p}_1)-E_\pi(\boldsymbol{p}_2))t}\,. \tag{4.45}$$

is the leading thermal state. In the center-of-mass frame $\boldsymbol{p}_1 = \boldsymbol{p}_2$ and the time dependence drops out. Without loss of generality let $E_\pi(\boldsymbol{p}_2) > E_\pi(\boldsymbol{p}_1)$. It is sufficient to consider the exponentially decreasing term in Eq. (4.45). This is sufficient because the signal in the relevant correlator matrices is subject to exponential error growth. Therefore, we will only extract the signal at relatively small t-values where the second term in ε_t is not yet relevant.

To remove the thermal pollution we will apply the so-called "weighting and shifting" procedure [82]. which condenses into the transformation

$$\tilde{\mathcal{C}}(t) \;=\; \mathrm{e}^{-\Delta E\, t}\left(\mathcal{C}(t)\mathrm{e}^{\Delta E\, t} - \mathcal{C}(t+1)\mathrm{e}^{\Delta E\,(t+1)}\right)\,, \tag{4.46}$$

with $\Delta E = E_\pi(\boldsymbol{p}_2) - E_\pi(\boldsymbol{p}_1)$. It is straightforward to see that this transformation leaves the

leading, physical exponential dependence unchanged, while the leading thermal pollution is removed. We have investigated subleading thermal pollutions thoroughly in [83]. As we will also see in Sec. 6.2, the procedures were not applicable in this work signal to noise ratio increased too fast to analyze the signal at large enough t-values.

CHAPTER 5

Numerical Setup

5.1 Numerical Setup

The gauge in this work are generated with Wilson twisted mass fermions and the Iwasaki gauge action. We use the $N_f = 2 + 1 + 1$ ensembles generated by the ETM Collaboration with a range of pion masses, three values of the lattice spacing and multiple volumes. the action contains a dynamical strange and charm sector in addition to two degenerate light flavor. The details are not relevant for the light quantities discussed in this work. They are described in [35, 36, 84].

In Tab. 5.1 we compile the parameters used during the ensemble generation. The inverse gauge coupling $\beta = 6/g^2$ controls the renormalization group flow and therefore the β-values 1.90, 1.95 and 2.10 correspond to different regularization cutoffs and therefore different lattice spacings. The bare values light quark mass μ_ℓ corresponds to μ in Eq.(2.45) for the quark mass parameters. For completeness μ_σ and μ_δ for the strange and charm sector are also given. Because the determinant in Eq. (2.53) is extremely costly to compute and becomes worse conditioned the lower μ_ℓ is, the given parameters correspond to unphysically high pion masses in the range $M_\pi = 230 - 510$ MeV. Beyond the numerical cost this also has the advantage, that at these pion masses other decay channels such as $\rho \to 4\pi$ or $\rho \to K\overline{K}$ that are expected to be negligible from experiment are actually energetically ruled out as the threshold moves above the ρ mass. Finally, Tab. 5.1 contains the spatial and temporal lattice extent in units of a and the number of gauge configurations used to estimate our results.

5.1.1 Scale Setting

The scale setting for the $N_f = 2 + 1 + 1$ twisted mass ensembles has been done in [85]. On these ensembles the Sommer parameter was determined to

$$r_0 = 0.474(11) \text{ fm} \tag{5.1}$$

in physical units. r_0/a was used as an intermediate quantity to determine the lattice spacings from the experimental values of the pion mass and decay constant. The results as well as the values of r_0/a for each β can be found in Tab. 5.3.

To translate lattice results to physical units in this work the Sommer parameter is used as intermediate lattice scale as well. Beyond r_0 in physical units, the physical pion mass value is

Ensemble	β	$a\mu_\ell$	$a\mu_\sigma$	$a\mu_\delta$	$(L/a)^3 \times T/a$	N_{conf}
A30.32	1.90	0.0030	0.150	0.190	$32^3 \times 64$	623
A40.20	1.90	0.0040	0.150	0.190	$20^3 \times 48$	531
A40.24	1.90	0.0040	0.150	0.190	$24^3 \times 48$	997
A40.32	1.90	0.0040	0.150	0.190	$32^3 \times 64$	493
A60.24	1.90	0.0060	0.150	0.190	$24^3 \times 48$	618
A80.24	1.90	0.0080	0.150	0.190	$24^3 \times 48$	611
A100.24	1.90	0.0100	0.150	0.190	$24^3 \times 48$	307
B25.32	1.95	0.0025	0.135	0.170	$32^3 \times 64$	197
B35.32	1.95	0.0035	0.135	0.170	$32^3 \times 64$	493
B35.48	1.95	0.0035	0.135	0.170	$48^3 \times 96$	265
B55.32	1.95	0.0055	0.135	0.170	$32^3 \times 64$	613
B85.24	1.95	0.0085	0.135	0.170	$24^3 \times 48$	586
D15.48	2.10	0.0015	0.120	0.1385	$48^3 \times 96$	304
D30.48	2.10	0.0030	0.120	0.1385	$48^3 \times 96$	241
D45.32	2.10	0.0045	0.0937	0.1077	$32^3 \times 64$	588

Table 5.1: The gauge ensembles used in this study. The label is a letter for β followed by $a\mu_\ell \cdot 10^4$, a dot and L/a. In addition to the input parameters relevant for the ensemble generation, we give the spatial and temporal lattice extent as well as the number of evaluated gauge configurations

needed as input. Like [85] we use

$$\overline{M}_\pi \;=\; 134.8(3)\ \text{MeV} \tag{5.2}$$

determined with chiral perturbation theory [4, 86] in the isospin symmetric limit.

The quantities in this work were determined on a different set of gauge configurations than was used to determine r_0/a Therefore, we use the values and errors given in Tab. 5.3 and use re-sampling. To reflect the statistical error the χ^2-function needs to be augmented by a prior.

$$\sum_\beta \left(\frac{p_{r_0/a}(\beta) - P_{r_0/a}(\beta)}{\Delta r_0/a(\beta)} \right)^2 \tag{5.3}$$

where $P_{r_0/a}(\beta)$ are the values from Tab. 5.3 and $p_{r_0/a}(\beta)$ and $\Delta r_0/a(\beta)$ are fit parameters.

The same procedure is applied to $\overline{M}_\pi$ and the errors on $\overline{M}_\pi$ are likewise included in the fits via a prior.

5.2 sLapH method

5.2.1 Laplacian Heaviside smearing

While the excited atates of the correlation function are exponentially suppressed by Eq. (2.120), the signal decays as well and at some time slice disappears under statistical noise. If operators that have high overlap with the ground state i.e. a large ground state amplitude the excited states are suppressed further and therefore negligible earlier. The probably most useful technique

ensemble	L[fm]	a[fm]	M_π[MeV]
A30.32	2.752	0.086	284
A40.20	1.720	0.086	342
A40.24	2.064	0.086	332
A40.32	2.752	0.086	324
A60.24	2.064	0.086	396
A80.24	2.064	0.086	456
A100.24	2.064	0.086	511
B25.32	2.496	0.078	273
B35.32	2.496	0.078	318
B35.48	3.744	0.078	313
B55.32	2.496	0.078	392
B85.24	1.872	0.078	490
D15.48	2.928	0.061	225
D30.48	2.928	0.061	316
D45.32	1.952	0.061	391

Table 5.2: The gauge ensembles used in this study. The label is a letter for β followed by $a\mu_\ell \cdot 10^4$, a dot and L/a. The most important features are replicated from [35, 36] in physical units.

β	a [fm]	r_0/a
1.90	0.0885(36)	5.31(8)
1.95	0.0815(30)	5.77(6)
2.10	0.0619(18)	7.60(8)

Table 5.3: Values of the Sommer parameter r_0/a and the lattice spacing a at the three values of β. See Ref. [85] for more details.

to achieve this improvement is gauge field smearing.

Because short range modes only insignificantly contribute to the spectrum at low energies, on can improve the overlap with the ground state emphasizing long distance modes. In this work we apply the stochastic Laplacian-Heaviside smearing described in [87]. Therein space is approximated by the span of the lowest eigenmodes of a Laplace operator applied to the quark field [88]. It is much smaller and therefore calculating the propagators Eq. (4.6) is significantly less expensive. In fact one big differentiator of the sLapH smearing is that storing propagators to hard disk and thus reusing them for more than one correlation function becomes feasible.

The short range / high energy modes are described by the large eigenvalues of the gauge invariant Laplace operator

$$\Delta(x,y;U) = \sum_{k=1}^{3} U_{\hat{k}}(x)\delta(x+\hat{k},y) + U_{\hat{k}}(x-\hat{k})^\dagger\delta(x-\hat{k},y) - 2\delta(x,y) \tag{5.4}$$

The Laplace operator acts on quark field only in spatial directions. As usual the temporal component is exempt, because the time dependence Eq. (2.120) would be obscured. The smearing

L	N_{ev}
20	66
24	120
32	220
48	660

Table 5.4: Choices for number of eigenmodes in dependence of spatial volume

is done by replacing the quark fields with

$$\psi(x)_\alpha \to \theta\left(\sigma_s^2 + \Delta(x,y)\psi(y)_\alpha\right) \tag{5.5}$$

where θ is the Heaviside step function and the positive real number σ_s^2 is a cutoff parameter for the eigenvalues of Δ. It is tuned such that the number of eigenvectors is the same for each L. The density of eigenvalues scales with $L^{\breve{g}}$ [88]. Therefore we our parameters are chosen such that $N_{\text{ev}}(L)$ scales like L^3 as well. The values are given in Tab. 5.4. As discussed in Sec. 2.2.3 the estimates from a finite Markov chain of gauge configurations are subject to gauge noise. The number of eigenvalues N_{ev} is chosen such that the approximation causes no noticable impediment of signal quality given the gauge noise. More details on the parameter choices can be found in [89, 90].

We introduce the matrices $V(x^0)$ whose columns are the lowest N_{ev} eigenvectors of the quark fields at a given time t.Because the Laplace operator acts in color space as well, V is a matrix with $T \cdot N_{\text{ev}}$ columns and $T \cdot L^3 \cdot N_c$ rows. The space composed of time, eigenvectors and Dirac space will below be referred to as "LapH space".[1] The eigenvectors $V^\dagger$ act like projectors

$$V^\dagger(t) : L^3 \times N_c \times N_d \to N_{\text{LapH}} \tag{5.6}$$

from full space (with color and Dirac) to LapH space on each given timeslice.

Instead of directly calculating the inverse of the dirac kernel $D_f^{-1}(x|y)$ for all spacetime-points$x$, y, one may use V to reduce the problem into the much smaller LapH-space

$$\mathcal{P}_f(x|y) = V(x)^\dagger D_f^{-1} V(y)\,. \tag{5.7}$$

The projected inverted kernel $\mathcal{P}_f(x|y)$ is called "perambulator". Its rank is several orders of magnitude lower than the rank of D. Not only thus this significantly lower the computation cost, but it also becomes feasible to save perambulators to hard disk and reuse them to "assemble" correlation functions for other physical processes. Using V again, the propagator can be estimated by projecting back to full space

$$D_f^{-1}(x|y) \approx V(x)\mathcal{P}_f(x|y)V(y)^\dagger\,. \tag{5.8}$$

Although numerical cost for calculating quark line estimates is considerably lower than for the full propagators, the number of inversions is still proportional proportional to N_{LapH}. Because $N_{\text{LapH}} \propto N_{\text{ev}} \propto L^3$, the cost of the LapH method increases rapidly for larger volumes.

[1] Because the Laplacian is diagonal in Dirac space, the Dirac separated from the LapH space in [87]. It is however very convenient to include it.

5.2.2 Stochastic Estimation

Above we argued that an exact calculation of the propagator is unnecessary as the correlation function is in any case subject to gauge noises. This argument may be extended by also approximating the perambulator $\mathcal{P}_f$ while making sure the error has not measurable impact on the correlation function. For this purpose random noise and dilution were proposed to estimate the perambulator stochastically [87].

Random Noise Vectors Let $\{\,\boldsymbol{\rho}_r,\ 1 \leq r \leq N_\mathrm{r}\,\}$ be a set of N_r Z_2-random noise vectors in LapH space where the index r denotes different random seeds. Empirically using Z_2-random vectors leads to comparatively low variance [87].

The expectation value of each random vector vanishes individually

$$\frac{1}{N_\mathrm{r}} \sum_r \boldsymbol{\rho}_r = 0 \tag{5.9}$$

and the vectors are mutually orthogonal

$$\frac{1}{N_\mathrm{r}} \sum_r \frac{1}{N_\mathrm{s}} \sum_s \boldsymbol{\rho}_r \rho_s^\dagger = \delta_{r,s} \mathbb{1}_\mathrm{LapH}\,. \tag{5.10}$$

These properties permit to perform the inversion of the Dirac matrix on a few random sources rather than all unit vectors. Consider the the linear system of equations

$$A(\boldsymbol{x}_r) = (\boldsymbol{\rho}_r)$$

Let $i, j \in \{1, \ldots, N_\mathrm{LapH}\}$. With Eq. (5.11) one finds

$$\frac{1}{N_\mathrm{r}} \sum_r \boldsymbol{x}_r^i \boldsymbol{\rho}_r^{j*} = \frac{1}{N_\mathrm{r}} \sum_r A^{-1}_{i,k} \boldsymbol{\rho}_r^k \boldsymbol{\rho}_r^{j*} = \frac{1}{N_\mathrm{r}} \sum_r A^{-1}_{i,k} \boldsymbol{\rho}_r^k \boldsymbol{\rho}_r^{j*} = A^{-1}_{i,k} \frac{1}{N_\mathrm{r}} \sum_r \boldsymbol{\rho}_r^k \boldsymbol{\rho}_r^{j*} = A^{-1}_{i,k} \delta_{k,j} = A^{-1}_{i,j}\,. \tag{5.11}$$

The matrix elements of A^{-1} are estimated by the expectation value of $\boldsymbol{x}_r^i \boldsymbol{\rho}_r^{j*}$. This means that the perambulator can be estimated by

$$\mathcal{P}_f \approx \frac{1}{N_\mathrm{r}} \sum_{r=1}^{N_\mathrm{r}} \boldsymbol{x}_r \boldsymbol{\rho}_r^\dagger$$

The variance of this estimate behaves like the variance of $\boldsymbol{\rho}\boldsymbol{\rho}^\dagger$. Therefore a large number of random sources would be necessary to uphold the signal quality. By using dilution, the variance and therefore the number of required random vectors may be considerably reduced.

Dilution Using dilution, reasonable statistical errors can be achieved with $N_\mathrm{r} = \mathcal{O}(1)$ random vectors.[2] In Eq. (5.10) the off-diagonal elements are basically noise with a zero expectation value. Dilution joins several components of the random vectors together and forces the off-diagonal elements to the other to exact zeros. This improves the approximation to the unit matrix and

[2] The lower bound is four random vectors all quarklines correlation function must be indepependent to avoid bias and there are four quarklines in $\left\langle \pi\pi\, \pi\pi^\dagger \right\rangle$.

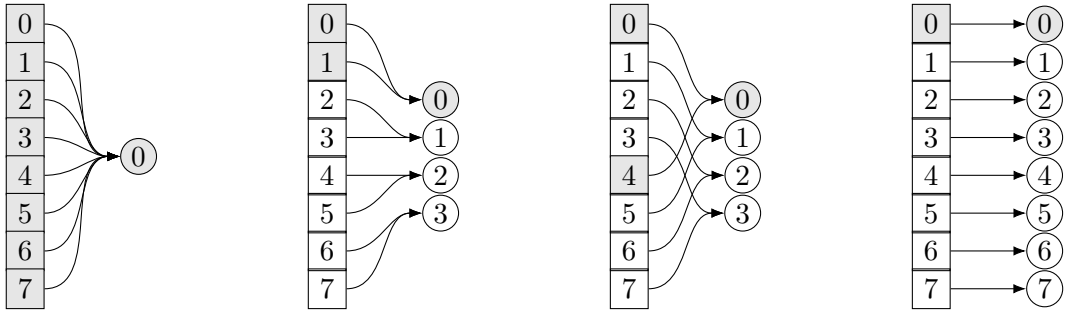

(a) No dilution (b) Block dilution (c) Interlace dilution (d) Full dilution

Figure 5.1: Visualization of different dilution schemes. Figure courtesy of Martin Ueding

L	b_T	b_D	b_E
20	B2	F	I6
24	B2	F	I6
32	B2	F	I4
48	B3	F	I4

Table 5.5: Dilution schemes used in this work for value L of the spatial volume.

thereby the variance. There are different "dilution schemes" which differ by which components of the random vectors are joined. They are visualized in Fig. 5.1.

We denote dilution projectors by $P^{(b)}$ where b is a shorthand for the dilution scheme. The common dilution schemes are

No dilution: $P^{(b)}_{ij} = \delta_{ij}$

Block-J (BJ) dilution: $P^{(b)}_{ij} = \delta_{ij}\delta_{b\lfloor J \cdot i/N \rfloor}$

Interlace-J (IJ) dilution: $P^{(b)}_{ij} = \delta_{ij}\delta_{bi \mod J}$

Full (F) dilution: $P^{(b)}_{ij} = \delta_{ij}\delta_{bi}$

where N is the dimension of the undiluted space. No dilution and full dilution can be interpreted as the special cases B1/ IN and BN/ I1 respectively.

In the extreme case of full dilution the diluted space has the same dimension as the undiluted one and all off-diagonal elements are exactly zero. For all other schemes there is still random noise on some offdiagonal elements, but the dimension of the diluted space is reduced.

For objects in LapH-space like the perambulator Eq. (5.8) the dilution acts in time, Dirac and eigenspace. The dilution projector factorizes to

$$P^{(b)}_{t\alpha v,t'\alpha' v'} = P^{(b_T)}_{t,t'} P^{(b_D)}_{\alpha,\alpha'} P^{(b_{\mathrm{ev}})}_{v,v'} \,.$$

where $t, t' \in \{1, \dots T\}$, $\alpha, \alpha' \in \{1, \dots 4\}$ and $v, v' \in \{1, \dots, N_{\mathrm{Ev}}\}$. b_T, b_d and b_{ev} are the respective dilution schemes. Like N_{ev} they depend on the spatial volumes. Our choices are also discussed in [89, 90] and summarized in Tab. 5.5.

The blocksizes required in the dilution scheme are largely independent of the volume. Therefore the projected LapH-spaces dimension is largely constant as well. When the dilution is applied at the source time this property is bequested to the required number of inversions. This is the reason the stochastic extension to the LapH-method facilitates the use of larger volumes.

The perambulator introduced in Eq. (5.7) now has an additional noise vector and dilution projector.

$$\mathcal{P}^{(b)}_{f;r}(x|y) = V^\dagger(x) D_f^{-1}(x|y) V(y) P^{(b)} \boldsymbol{\rho}_r \tag{5.12}$$

The same modification applies to the propagator estimate Eq. (5.8) which becomes

$$D_f^{-1}(x|y) = \frac{1}{N_r} \sum_r V(x) \mathcal{P}^{(b)}_{f;r}(x|y) \left(V(y) P^{(b)} \boldsymbol{\rho}_r \right)^\dagger . \tag{5.13}$$

This approximation is also called "Quark line estimate".

Like $V^\dagger(t)$ in Eq. (5.6), $(V(t)P^{(b)}\boldsymbol{\rho}_r)^\dagger$ projects from full spacetime to a smaller space whose dimension is given by the number of blocks the dilution scheme maps to. Compared to the undiluted LapH method the projected spaces dimension is further reduced by several orders of magnitudes.

5.3 Correlation functions with Quarkline estimates

The correlation functions of Chap. 4 were expressed in terms of propagators with the help of Wick's theorem. Replacing propagators by quarkline estimates has consequences that are exemplary discussed for the pion correlation function Eq. (4.5).

In the pion correlation function the propagator D_u^{-1} for an u-quark appears alongside its counterpart for the d quark. In Sec. 4.1.1 γ_5-hermiticity

$$D_d^{-1}(y|x) = \gamma_5 D_u^{-1}(x|y)^\dagger \gamma_5 \tag{4.13}$$

has already been used to simplify the final results for the ρ meson.

Successively inserting Eq. (4.13) and (5.13) into the pion correlation function Eq. (4.5) and using the cyclic property of the trace yields

$$\begin{aligned}
C_{\pi^+}(x|y) &= -\frac{1}{N_r N_s} \sum_{\substack{r,s \\ r\neq s}} \operatorname{tr} \Big(\gamma^\pi V(y) V^\dagger(y) D_u^{-1}(y|x) (V(x) P^{(b_r)} \rho_r)(V(x) P^{(b_r)} \rho_r)^\dagger \\
&\qquad \gamma^\pi \gamma_5 \left(V(y) V^\dagger(y) D_u^{-1}(y|x) (V(x) P^{(b_s)} \rho_s)(V(x) P^{(b_s)} \rho_s)^\dagger \right)^\dagger \gamma_5 \Big) \\
&= -\frac{1}{N_r N_s} \sum_{\substack{r,s \\ r\neq s}} \operatorname{tr} \Big(\gamma^\pi V(y) \mathcal{P}^{(b_r)}_{u;r}(y|x) (V(x) P^{(b_r)} \rho_r)^\dagger \\
&\qquad \gamma^\pi \gamma_5 (V(x) P^{(b_s)} \rho_s) \mathcal{P}^{(b_s)}_{u;s}(y|x)^\dagger V(y)^\dagger \gamma_5 \Big) \\
&= -\frac{1}{N_r N_s} \sum_{\substack{r,s \\ r\neq s}} \operatorname{tr} \Big(\left(\mathcal{P}^{(b_s)}_{u;s}(y|x)^\dagger \left(V(y)^\dagger \gamma_5 \gamma^\pi V(y) \right) \mathcal{P}^{(b_r)}_{u;r}(y|x) \right) \\
&\qquad \left((V(x) P^{(b_r)} \rho_r)^\dagger \gamma^\pi \gamma_5 (V(x) P^{(b_s)} \rho_s) \right) \Big) .
\end{aligned} \tag{5.14}$$

The condition $r \neq s$ was imposed to avoid bias. In the last steps the terms were parenthesized in a way that allows a numerically efficient computations. Because only the source is projected to LapH space the peramubulators are non-square in contrast to the Dirac matrices. Matrix multiplication scales with the third power of matrix size, The execution order defined by the parentheses in Eq. (5.14) is chosen so that the most frequent multiplications run over the smallest matrices.

Momentum space So far the Wick contractions were performed in position space. Yet, for the Lüscher method in moving frames energy levels and therefore operators in momentum space are required. The projection to definite (linear) momentum may be done by a Fourier transformation as explained in Eq. (3.10). This Fourier factor can simply be factored out. The correlation function in momentum space it becomes

$$\begin{aligned} C_{\pi^+}(t,\boldsymbol{p}|0,\boldsymbol{q}) &= \left\langle \pi^+(t,\boldsymbol{p})\ \pi^+(0,\boldsymbol{q})^\dagger \right\rangle_F \\ &= \frac{1}{L^6}\sum_{\boldsymbol{x},\boldsymbol{y}} \mathrm{e}^{\mathrm{i}(\boldsymbol{p}\boldsymbol{x}-\boldsymbol{q}\boldsymbol{y})} \left\langle \pi^+(x)\ {\pi^+}^\dagger(y) \right\rangle_F \\ &= \frac{1}{L^6}\sum_{\boldsymbol{x},\boldsymbol{y}} \mathrm{e}^{\mathrm{i}(\boldsymbol{p}\boldsymbol{x}-\boldsymbol{q}\boldsymbol{y})} C_{\pi^+}(x|y) \\ &= -\frac{1}{L^6}\sum_{\boldsymbol{x},\boldsymbol{y}} \mathrm{e}^{\mathrm{i}(\boldsymbol{p}\boldsymbol{x}-\boldsymbol{q}\boldsymbol{y})} \frac{1}{N_r N_s} \sum_{\substack{r,s \\ r\neq s}} \mathrm{tr}\left(\left(\mathcal{P}^{(b_s)}_{u;s}(y|x)^\dagger \left(V(y)^\dagger \gamma_5 \gamma^\pi V(y) \right) \mathcal{P}^{(b_r)}_{u;r}(y|x) \right) \right. \\ &\qquad \left. \left((V(x)P^{(b_r)}\rho_r)^\dagger \gamma^\pi \gamma_5 (V(x)P^{(b_s)}\rho_s) \right) \right) \end{aligned} \tag{5.15}$$

where in the last step Eq. (5.14) was inserted.

The generalization to two particles is straightforward. The steps to express the correlation function in terms of quarkline estimates in position space stay the same. Like in Eq. (3.11) the fourier transformation is then just applied to each spatial index. More details may be found in [91].

In the special case $\boldsymbol{p} = \boldsymbol{q} = \boldsymbol{0}$, the exponentials become 1 for all $\boldsymbol{x}, \boldsymbol{y}$. Because the eigenvectors of spanning LapH space are orthogonal, $V^\dagger V = \mathbb{1}$ and Eq. (5.15) simplifies to Eq. (5.14)

Apart from Dirac matrices and scalars for the momenta the final expression Eq. (5.15) only consists of sLapH-eigenvectors V, perambulators $\mathcal{P}$ and randomvectors ρ. These same constituents form every correlation function discussed in Chap. 4 and many more. Therefore the numeric calculation of correlation functions given V, $\mathcal{P}$ and ρ is essentially a tensor contractions. Within this thesis, an optimzied code to perform such tensor contractions was written.[3] For more details, a full documentation is available online[4]. A list of all implemented correlation functions and the corresponding quark flow diagrams are given in Sec. A.4.

[3] https://github.com/maowerner/sLapH-contractions
[4] http://hiskp-lqcd.github.io/sLapH-contractions/

CHAPTER 6

Results

In this chapter our results are presented. They are published in [1].

6.1 Pion Dispersion Relation

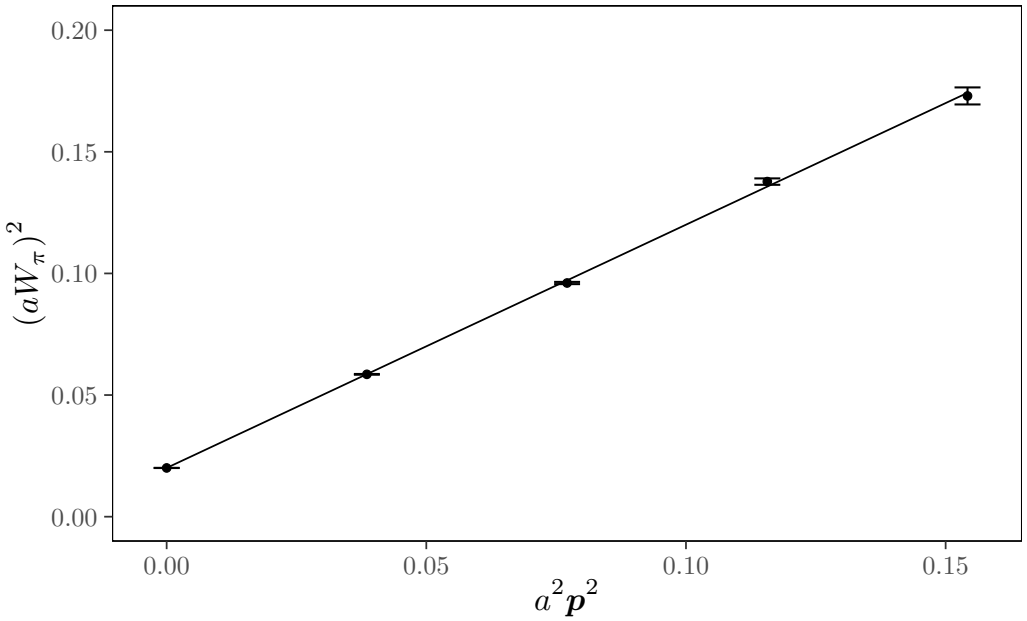

Figure 6.1: Dispersion relation of the pion for ensemble A40.32.

In Sec. 2.3.2 the Lüscher formula was extended to moving reference frames. This was done by boosting the system to center-of-mass with the relativistic dispersion relation

$$W_{\mathrm{L}} = \sqrt{\boldsymbol{p}_{\mathrm{cm}}^2 + E_{\mathrm{CM}}^2}\,. \tag{2.73}$$

The first step before calculating the energy shifts k that enter the Lüscher formula Eq. (2.97) is checking the dispersion relation. This is usually done by computing the pion mass in moving

reference frames and comparing to the value predicted from the zero momentum mass via

$$E_\pi(\boldsymbol{p}) = \sqrt{\boldsymbol{p}^2 + M_\pi^2}\,. \tag{6.1}$$

Note that in our formulation we have $M_{\pi^+} = M_{\pi^-}$. An exemplary result for the A40.32 ensemble is depicted in Figure 6.1. The values agree within errors is observed up to $\boldsymbol{d}^2 = 4$. This makes us confident that using the dispersion relation is safe.

Furthermore the values $E_\pi(\boldsymbol{p})$ determined with the continuum dispersion relation are used as an input for the weighting and shifting transformation Eq. (4.46).

6.2 Energy Levels

The next step is computing the energy spectrum in the presence of strong interaction. The desired energy levels are directly obtainable from suitable correlation functions in the limit of large time separation. Which correlation function are required specifically for the ρ channel has been addressed in Chap. 3 and 4.

In practice the step from correlation functions to energy levels is subject to two major error sources. The first major uncertainty has already been discussed in Sec. 4.1.2: Pollution from thermal states. The other major uncertainty stems from the use of regression to determine the energy levels. Higher states in the spectrum only decay exponentially when the time separation increases whereas thermal states become relevant at large time separations. The fit range must start late and end early enough to avert systematic errors caused the excited as well as thermal states while still containing enough data to retain statistical significance. The fit range effectively becomes a hyperparameter that must be controlled as well.

Thermal states

In Sec. 4.1.3 we already preempted the leading thermal state out of Eq. (4.40)-(4.43) is

$$\mathrm{e}^{-E_\pi(\boldsymbol{p}_1)T}\mathrm{e}^{-(E_\pi(\boldsymbol{p}_2)-E_\pi(\boldsymbol{p}_1))t} \tag{6.2}$$

assuming that $E_\pi(\boldsymbol{p}_2) > E_\pi(\boldsymbol{p}_1)$. This is based on a numerical comparison with the values for $E_\pi(\boldsymbol{p})$ determined from the continuum dispersion relation as in Sec. 6.1. For the comparison we assumed all states to have the same amplitude and neglected the energy shift by replacing $E_{\pi\pi}(\boldsymbol{p}_1, \boldsymbol{p}_2) \approx E_\pi(\boldsymbol{p}_1) + E_\pi(\boldsymbol{p}_2)$. In the same manner we arrived at the conclusion that pollutions with two pions in the asymptotic and intermediate state or three pions in either are neglible.

The leading pollution was subtracted by weighting and shifting as described in Sec. 4.1.3.

To verify the procedure worked as intended we compared the weighted and shifted correlation function with the original one. For the case of two pions with maximal isospin the thermal pollutions and therefore the effect of the weighting and shifting is clearly visible [89]. However, due to a much larger signal-to-noise ratio, this is not the case for the correlation functions investigated in this work. Between the principal correlators $\lambda(t, t_0)$ derived from the original correlation functions $\mathcal{C}(t, t_0)$ and $\tilde{\lambda}(t, t_0)$ derived from $\tilde{\mathcal{C}}(t, t_0)$ there is no qualitative difference visible.

The extracted energy showed a strong dependence on the fit interval. To judge whether thermal state removal worked we need to do this comparison keeping control over fit interval and t_0 for the Gevp because it heavily influences the two-state fit.

Fit range selection

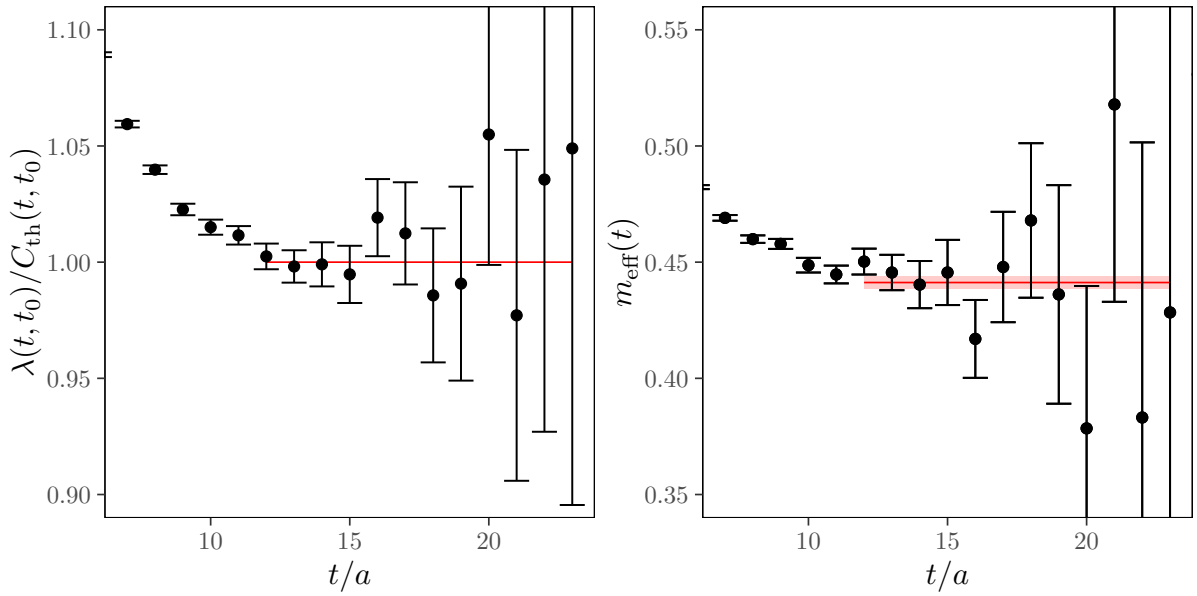

Figure 6.2: In the left panel we show $\lambda(t,t_0)/C_{\mathrm{th}}(t,t_0)$ as a function of t/a for the ground state energy level in irrep E. The reference time for the GEVP was set to $t_0/a = 3$ and the ensemble is A40.32. The horizontal line with error band indicates the fitted energy value with statistical uncertainty. The extent of the line indicates the fit range. In the right panel we show the effective mass as a function of t/a and the same fitted energy value for reference.

We perform the fitting to the principal correlator $\lambda(t,t_0)$ (and $\tilde{\lambda}$) by surveying multiple fit ranges $[t_{\mathrm{min}}, t_{\mathrm{max}}]$ and selecting a representative one. We enforce a plateau length of at least four points, which must be compatible within errors and have relative errors below 50%. Additionally we require no significant dependence on t_{max} as this would be a consequence of residual thermal pollution. The dependence on t_{min} is very pronounced when t_{min} is in a region, where excited states are still relevant. We increase t_{min} until this dependence vanishes. A p-value above 0.05 was preferred to ascertain that the data in the chosen range are described by our fit. In the rare cases where multiple fit ranges gave competing and equally likely results, we chose an intermediate range. The influence of varying t_0 from 1 to the onset of the plateau was checked and found to be negligible. Therefore, we chose $t_0 = 3$ on the coarser two and $t_0 = 4$ on the finest lattice spacing, corresponding to approximately 0.25 fm in physical units. Finally, all other qualities being equal, we preferred larger t_{max}.

In Figure 6.2 we show an example for the fit range chosen for ensemble A40.32 where $d^2 = 1$ and irrep $\Gamma = \mathrm{E}$ without weighting and shifting. In the left panel, we show the ratio of principal correlator $\lambda(t,t_0)$ and the single exponential fit model $\mathcal{C}_{\mathrm{th}}(t,t_0) = \exp(-W(t-t_0))$. Compared to the effective mass, the ratio is more robust numerically. By definition the error band is centred around 1. The error band has a conic shape because the error of the fit result is constant, while the value of the correlator decreases exponentially. In the right panel we show for illustration the result of the correlator fit as a red band along with the effective mass

$$m_{\mathrm{eff}}(t) = \log \frac{\mathcal{C}(t)}{\mathcal{C}(t+1)} \,.$$

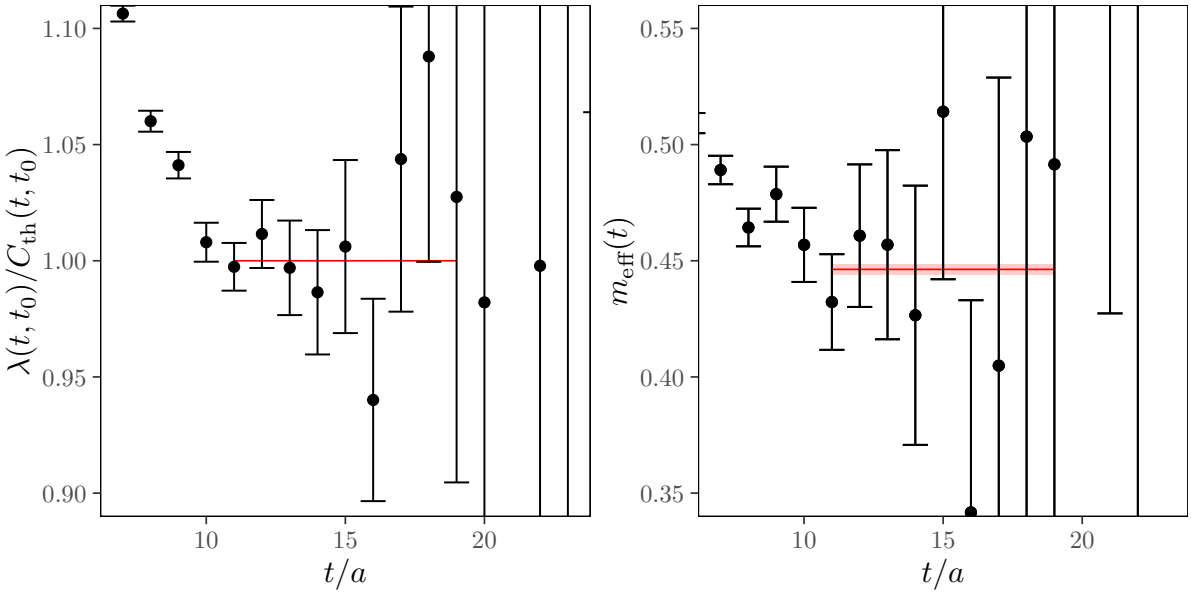

Figure 6.3: the same as Figure 6.2, but for weighted and shifted $\tilde{\lambda}$.

As mentioned above, the effects of thermal states are not visible here. The energy level was determined as $aW = 0.4412(26)$.

In Figure 6.3 we show the same plots but this time with weighting and shifting. The size of error bars is increased compared to without weighting and shifting, which can be explained by the reduced correlation of neighbouring timeslices. For very large t, points are not depicted because they were compatible with zero. For this reason, t_{max} was chosen smaller compared to before. The fit model was modified as described in Eq. (4.46) and the calculation of the effective mass in the right panel was changed accordingly. The fit result increased by roughly one standard deviation to $aW = 0.4463(23)$.

It remains unclear whether this difference is caused by small but barely significant thermal states or is only the result from the independent choice of a fit range. In Figure 6.4 we show all energy levels aE_{CM} for all irreps Γ and boosts $\boldsymbol{d}^2$ exemplary for ensemble A40.32. The red circles are with weighting and shifting, the blue triangles without. The two kaon upper and two pion lower thresholds are indicated by the dashed horizontal lines. For all $\boldsymbol{d}^2$-value and irrep combinations, apart from two, we have two energy levels below the two kaon inelastic threshold.

Comparing energy levels with and without thermal state removal, we observe good agreement. Statistical uncertainties are in general larger with weighting and shifting. However the difference between energy levels can be statistically significant in some cases. Therefore, we perform the full analysis with and without weighting and shifting. The result we quote will be the weighted mean of both these results. We are confident that this way we keep control over both major sources of systematic uncertainties.

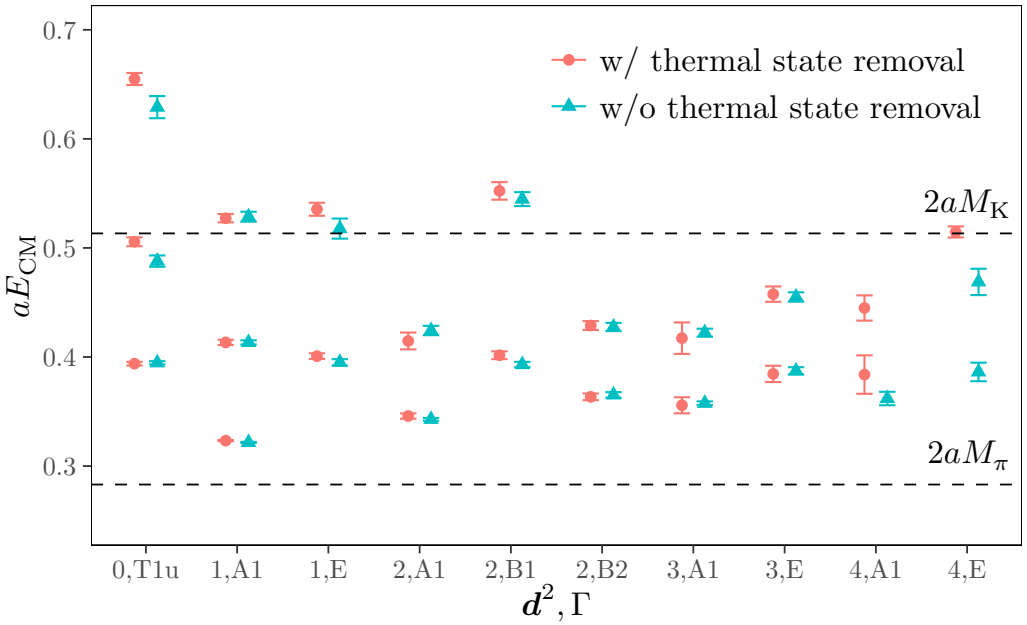

Figure 6.4: Example of all energy levels in lattice units for ensemble A40.32 for irrep Γ and $\boldsymbol{p}_{\mathrm{cm}}$ labeled by $\boldsymbol{d}^2$. The two kaon and and two pion thresholds are indicated by the two dashed horizontal lines. The two colours and symbols distinguish the estimate of E_{CM} with and without thermal state removal.

6.3 Phase Shift Determination

The relation between energy levels and scattering momentum was defined in Eq. (2.59). For the concrete energy levels above it reads

$$ak^2 \;=\; \frac{(aW)^2}{4} - (aM_\pi)^2\,. \tag{6.3}$$

With the help of Eq. (2.97) the phase shift values at each energy level may be determined. It is worth noting, that the Lüscher ζ-function exhibits poles in the γ-q plane where noninteracting energy levels are located. The data for γ and q is comprised by samples drawn from the Monte-Carlo history of gauge configurations. It obeys a statistical distribution with a finite width. A case that can numerically appear, but is physically impossible, is this distribution crossing a pole. This is easiest demonstrated by the infinite-statics limit. The width of the distribution is the error of the mean and approaches zero the more statistic becomes available. Even if the distribution crosses at some finite statistics it will cease to do so at larger statistics. Changing a systems relative position to a pole is might go as far as changing the sign of the interaction. For this reason we require each distributions to be contained in a sector between two poles and disregard points where this requirement is not met.

This requirement created problems when generating samples with the bootstrap procedure introduced in Sec. 2.2.3. The standard deviation of the bootstrap distribution is the standard error of the mean of the original data. Especially on the smallest lattice spacing the distribution is too broad and by enforcing our requirement up to 80% of the points would have to be disregarded. As explained in Sec. 2.2.3 the jackknife distribution narrower compared to bootstrap because by the inverse of the number of samples. For this reasons we chose the jackknife procedure to draw

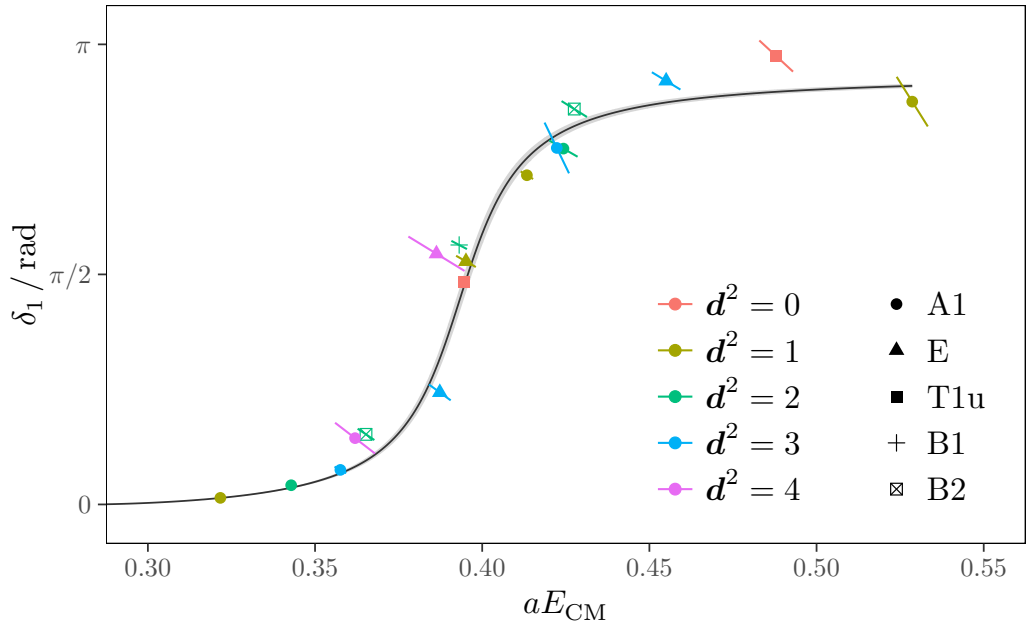

Figure 6.5: Phase shift δ_1 as a function of E_{CM} in lattice units for ensemble A40.32. The solid line with error band represents the fit result of Eq. (6.7) to all the data w/ thermal state removal. Colours encode the different $\boldsymbol{d}^2$-values, while symbols distinguish the irreps.

samples which satisfy our requirement in almost all cases. Due to the non-linear nature of the Lüscher formula one might be concerned that the sample error might not be estimated correctly with the jackknife procedure. This was addressed by comparing the final error estimate of the phase shift for bootstrap and jackknife [1]. We found the numbers to be compatible and therefore the jackknife procedure trustworthy in this case.

As discussed in Sec. 2.1.3, in the presence of a resonance like the ρ the phase shift δ_1 as a function of the centre-of-mass energy aE_{CM} is expected so follow a characteristic S-shape.

To obtain a parametrization of the phase shift, the non-resonant background is usually approximated by the effective range expansion (ERE) [92]. Expanding the $\pi\pi$ scattering amplitude from current algebra into partial waves yields the P-wave phase shift δ_1

$$\mathrm{e}^{\mathrm{i}\delta_1} \sin\delta_1 = \frac{M_\rho \Gamma_\rho \left(\frac{p}{p_\rho}\right)^3 \frac{M_\rho}{\sqrt{s}}}{M_\rho^2 - s - \mathrm{i} M_\rho \Gamma_\rho \left(\frac{p}{p_\rho}\right)^3 \frac{M_\rho}{\sqrt{s}}} \,. \tag{6.4}$$

where

$$p = \sqrt{s/4 - M_\pi^2}\,, \qquad p_\rho = p\,|_{s=M_\rho} \tag{6.5}$$

[1] for the on the points that survived the disregarding criterium

and the width is related to the coupling constant $g_{\rho\pi\pi}$ via

$$\Gamma_\rho = \frac{2}{3}\frac{g^2_{\rho\pi\pi}}{4\pi}\frac{p^3_\rho}{M^2_\rho}\,. \tag{6.6}$$

Because the channel contains only one resonance and all other thresholds are kinematically suppressed or open at far higher energies, Γ_ρ is approximately constant. Inserting Eq. (6.6) into Eq. (6.4) and a few lines of algebra yield

$$\tan\delta_1 = \frac{g^2_{\rho\pi\pi}}{6\pi}\frac{p^3}{\sqrt{s}(M^2_\rho - s)}\,. \tag{6.7}$$

We remark that Eq. (6.7) contains several approximations. $\tan\delta_1$ has a pole at $\sqrt{s} = M_\rho$ which was rewritten as by a rational function where the denominator is a first-order polynomial in k^2. For $M_\rho = 775$ MeV the width predicted by Eq. (6.4) is $\Gamma_\rho \simeq 130$ MeV; underestimating the experimental width in Eq. (3.3). For the current level of experimental accuracy it is insufficient because no form factor corrections were applied in the derivation of Eq. (6.6) and $\omega\rho\pi$-mixing is neglected as well 3-body-forces, inelasticities and partial wave mixing. Nevertheless, Eq. (6.7) has successfully been used in lattice calculations [21]. For higher-than-physical pion masses the phase space shrinks and thus the width of the ρ^0 meson decreases. With the modification Eq. (6.6) that ascribes an energy dependence to the width, a Breit-Wigner function yields a reasonable description of the resonance region. The resonance must be isolated and narrow and E_{CM} may not be at threshold. Additional modifications such as barrier terms, have been observed to slightly improve fit quality, but had no significant effect on the final results [27, 28, 32].

In Figure 6.5 the phase shift for ensemble A40.32 is shown along with the two-parameter fit of Eq. (6.7) to our data. Different moving frames $\boldsymbol{d}^2$ and irreps Γ are distinguished by different colors and shapes respectively. Because δ_1 is negatively correlated with aE_{CM}, showing conventional x-y-errorbars would be misleading. To reflect the correlation x- and y-errors are added vectorially, i.e. the length of the slanted error bars is the sum of x- and y-error added in quadrature. The resulting errorbars are slanted. The slope is indicative of the strength of the correlation and its negative sign reflects the negative correlation.

We have performed the fit to the phase shift data in several different ways.

To test whether the result is biased by our selection of moving frame momenta the fits were done on the subset of all points for which $\boldsymbol{d}^2 \leq k$ with $k = 1, 2, 3$. While obviously the statistical uncertainty changed, an Anova confirmed that there was no significant change of the sample mean.

Sec. 6.2 already explained the necessity to perform the full analysis with (w/) and without (w/o) thermal state removal. Indeed the fit parameters, in particular M_ρ differed by up to 4 standard deviations w/ and w/o thermal state removal. We quote the weighted mean over results w/o and w/ thermal state removal as our final results. In addition we include the difference ΔQ_Y between the weighted mean and w/o and w/ thermal state removal as systematic uncertainty in our error budget. In order to carry this uncertainty through the following chiral and continuum extrapolation, it is folded into the bootstrap distribution like we already did in [83]. This is

implemented by rescaling the bootstrap distribution with a factor

$$s = \sqrt{\frac{(\Delta x)^2 + \sum_Y (\Delta Q_Y)^2}{(\Delta x)^2}}\,. \tag{6.8}$$

where Δx is the statistical uncertainty of the weighted mean and $Y \in \{\mathrm{w/o}, \mathrm{w/}\}$.

All results for M_ρ and $g_{\rho\pi\pi}$ determined by this procedure w/ and w/o thermal state removal are compiled in Tab. 6.1. The width Γ_ρ computed via Eq. (6.6) is tabulated in Tab. 6.2. In the latter table we also give the reduced χ^2-values of the Breit-Wigner fits and the values for the (charged) pion mass in lattice units aM_π.

Ensemble	$aM_\rho^{\mathrm{w/o}}$	$aM_\rho^{\mathrm{w/}}$	aM_ρ^{av}	$g_{\rho\pi\pi}^{\mathrm{w/o}}$	$g_{\rho\pi\pi}^{\mathrm{w/}}$	$g_{\rho\pi\pi}^{\mathrm{av}}$
A30.32	0.3906(11)	0.3968(15)	0.3929(32)	6.0(2)	5.8(2)	6.0(2)
A40.24	0.4010(15)	0.4084(14)	0.4051(38)	5.7(1)	4.9(2)	5.4(4)
A40.32	0.3957(12)	0.3971(13)	0.3964(11)	5.7(1)	5.5(2)	5.6(1)
A60.24	0.4134(12)	0.4170(12)	0.4153(20)	5.4(1)	5.4(1)	5.4(1)
A80.24	0.4265(11)	0.4314(14)	0.4282(26)	5.3(1)	5.0(3)	5.2(2)
A100.24	0.4512(11)	0.4521(12)	0.4516(09)	4.7(2)	5.0(2)	4.9(2)
B25.32	0.3527(30)	0.3608(40)	0.3556(47)	6.3(3)	5.9(6)	6.2(4)
B35.32	0.3554(17)	0.3582(17)	0.3568(18)	6.3(2)	5.4(3)	6.0(5)
B35.48	0.3617(15)	0.3609(26)	0.3615(13)	5.8(2)	6.6(5)	6.0(4)
B55.32	0.3709(09)	0.3739(09)	0.3722(16)	5.6(1)	6.1(1)	5.8(3)
D15.48	0.2751(35)	-	0.2751(35)	6.5(7)	-	6.5(7)
D30.48	0.2747(16)	0.2926(22)	0.2811(91)	5.3(4)	5.1(5)	5.2(3)
D45.32	0.2866(09)	0.2948(14)	0.2890(42)	5.8(2)	4.6(5)	5.6(6)

Table 6.1: ρ mass aM_ρ and coupling $g_{\rho\pi\pi}$ for all ensembles w/ and w/o thermal state removal and the weighted average including the systematic uncertainty as explained in the text.

In both these tables from the list $N_f = 2 + 1 + 1$ ensembles Tab. 5.2 the ensembles A40.20 and B85.25 were left out because the fits did not converge. A40.20 and B85.24 have the smallest physical volume of all our ensembles. We conclude that the spatial extent should at least be ≈ 2 fm in order to determine scattering properties.

In order to quantify the residual finite volume effects in our results for M_ρ and Γ_ρ. we have two groups of ensembles with all identical parameters apart from the volume. These are ensembles A40.24 and A40.32 as well as B35.32 and B35.48.

In Figure 6.6 we directly compare the phase shift for the different volumes. In the left panel the phase shift points for A40.24 (blue) with the ones for A40.32 (red), in the right panel B35.48 (red) with B35.32 (blue). Even though the Breit-Wigner fits happen to result in slightly different values for the resonance parameters, the differences are below two standard deviations and do not show a systematic ordering as one would expect from finite volume effects.

Thus, the weighted average with error including the systematic uncertainty from thermal state removal should also safely include residual effects from finite volume.

Finally there are a few ensembles apart from A40.20 and B85.24 where the Breit-Wigner type fits to the phase shift points are problematic. On the one hand this is the case for ensemble with the heaviest pion mass A100.24. The width approaches zero, which leaves the fits little

Ensemble	aM_π	K_{M_π}	$a\Gamma_\rho^{\mathrm{w/o}}$	$a\Gamma_\rho^{\mathrm{w/}}$	$a\Gamma_\rho^{\mathrm{av}}$	$\chi^2_{\mathrm{w/o}}$	$\chi^2_{\mathrm{w/}}$
A30.32	0.12392(13)	1.0081(52)	0.0435(23)	0.0427(30)	0.0432(19)	2.66	2.79
A40.24	0.14154(12)	1.0206(95)	0.0312(14)	0.0243(15)	0.0279(36)	1.77	1.43
A40.32	0.14429(20)	1.0039(28)	0.0287(15)	0.0271(18)	0.0280(14)	1.81	1.49
A60.24	0.17314(19)	1.0099(49)	0.0133(07)	0.0139(07)	0.0136(06)	2.53	1.11
A80.24	0.19909(17)	1.0057(29)	0.0036(03)	0.0040(05)	0.0037(03)	1.72	0.54
A100.24	0.22236(23)	1.0037(19)	0.0003(01)	0.0004(01)	0.0004(01)	0.41	8.14
B25.32	0.10850(32)	1.0136(60)	0.0454(50)	0.0427(89)	0.0447(46)	1.05	0.56
B35.32	0.12380(10)	1.0069(32)	0.0340(20)	0.0260(26)	0.0309(43)	0.97	0.90
B35.48	0.12486(14)	-	0.0316(24)	0.0397(56)	0.0328(46)	1.35	0.88
B55.32	0.15551(12)	1.0027(14)	0.0123(05)	0.0156(07)	0.0136(17)	1.30	0.93
D15.48	0.07067(15)	1.0081(22)	0.0491(114)	-	0.0491(114)	0.68	-
D30.48	0.09754(14)	1.0021(07)	0.0179(25)	0.0206(40)	0.0187(25)	1.03	2.79
D45.32	0.12046(19)	1.0047(14)	0.0102(06)	0.0079(15)	0.0098(13)	1.17	0.93

Table 6.2: We give aM_π, the finite size correction factor K_{M_π}, the ρ width $a\Gamma_\rho$ computed from aM_ρ and $g_{\rho\pi\pi}$ using Eq. (6.6) w/ and w/o thermal state removal, and the weighted average as explained in the text. In addition we give the reduced χ^2-values of the corresponding fits to the phase shift data.

freedom; a fact reflected by the untrustworthy χ^2.

On the other hand, unfortunately the fit on D15.48, our most chiral ensemble, is difficult, however, for different reasons. For D15.48 statistical uncertainties on the energy levels are quite large. As a consequence, the Breit-Wigner fit for the case w/ thermal state removal is not converging. The fit for the case w/o thermal state removal gives large uncertainties. Combined with the rather low lying inelastic threshold at $2M_K$, we do not consider this ensemble as trustworthy for this calculation.

6.4 Pion Mass Dependence

In Ref. [93] the pion mass dependence of the ρ-meson mass has been computed using effective field theory with infrared regularisation. Up to $\mathcal{O}(M_\pi^3)$ plus the non-analytic term of order M_π^4, the dependence reads

$$M_\rho(M_\pi^2) \;=\; M_\rho^0 + c_1 M_\pi^2 + c_2 M_\pi^3 + c_3 M_\pi^4 \ln\left(\frac{M_\pi^2}{M_\rho^2}\right) + \mathcal{O}(M_\pi^4)\,. \tag{6.9}$$

To this order the formula contains four unknown parameters, the ρ mass in the chiral limit M_ρ^0 and the parameters c_1, c_2 and c_3. Using this mass dependence of M_ρ and the KSFR relation [94, 95], we can try to relate $g_{\rho\pi\pi}$ to M_π up to order M_π^3 using Eq. (6.9) and the SU(2) chiral perturbation theory formula for f_π [4]

$$g_{\rho\pi\pi}(M_\pi^2) \;\approx\; \frac{M_\rho}{f_\pi} \approx \frac{1}{f_0}\left[M_\rho^0 + M_\pi^2\left(c_1 + \frac{2}{16\pi^2 f_0^2}(\log\xi_\ell - \bar{\ell}_4 - \ell_\pi)\right) + c_2 M_\pi^3\right] + \mathcal{O}(M_\pi^4)\,. \tag{6.10}$$

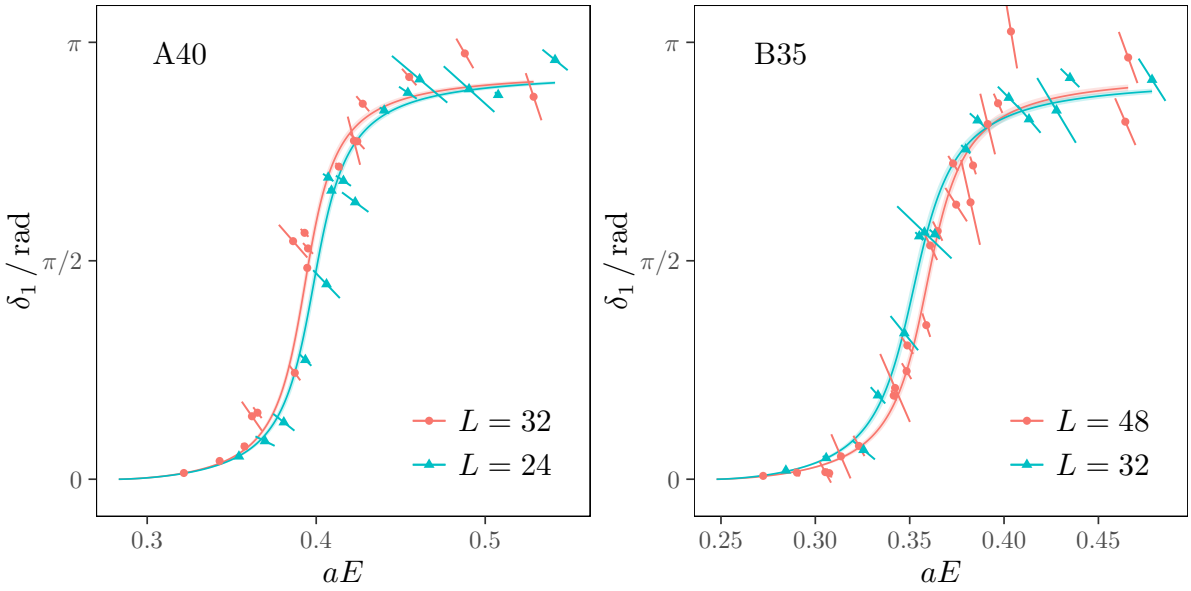

Figure 6.6: We show the phaseshift δ_1 as a function of E_{CM} in lattice units. Left we compare A40.24 (blue) with A40.32 (red) and right B35.48 (red) with B35.32 (blue). The lines with error bars represent the corresponding fits with Eq. (6.7) to the data.

Here, f_π is the pion decay constant, f_0 its value in the chiral limit and the parameters M_ρ^0 and c_i are the ones from Eq. (6.9). Note that we follow the convention with $f_\pi \approx 130$ MeV [38]. In addition we have used the definitions

$$\ell_\pi \;=\; \log\left(\frac{\overline{M}_{\pi^+}}{4\pi f_0}\right)^2, \quad \xi_\ell \;=\; \frac{M_\pi^2}{16\pi^2 f_0^2}$$

and the usual low energy constant $\bar{\ell}_4$. Values for f_0 and $\bar{\ell}_4$ have been computed on the ensembles used here in Ref. [85]

$$f_0 \;=\; 121.1(2)\ \mathrm{MeV}\,, \qquad \bar{\ell}_4 \;=\; 4.7(1)\,.$$

In nature the KSFR relation [94, 95] $g_{\rho\pi\pi} \approx M_\rho/f_\pi$ is fulfilled to very good approximation. However, it is not clear at all whether it can be extended beyond leading order in the pion mass.

In Ref. [96, 97], the pion mass dependence of the ρ-meson mass and width has been calculated with the complex mass renormalisation scheme from an effective field theory with explicit contributions corresponding to the ω-meson. It is based on the assumption of vector meson dominance and, thus, model dependent; see also Ref. [98] for details on the model. However, its advantage is that mass and width can be extrapolated in a combined fit. The squared pole position of the ρ resonance, $Z = \left(M_\rho - \mathrm{i}/2\ \Gamma_\rho\right)^2$ has the following pion mass dependence

$$Z = Z_\chi + c_\chi M_\pi^2 - \frac{g_{\omega\rho\pi}^2}{24\pi} Z_\chi^{1/2} M_\pi^3 + \mathcal{O}\left(M_\pi^4\right), \tag{6.11}$$

where Z_χ is the pole position in the chiral limit and c_χ, $g_{\omega\rho\pi}$ are coupling constants. Higher order corrections in M_π are known in principle, which also include logarithmic terms. The

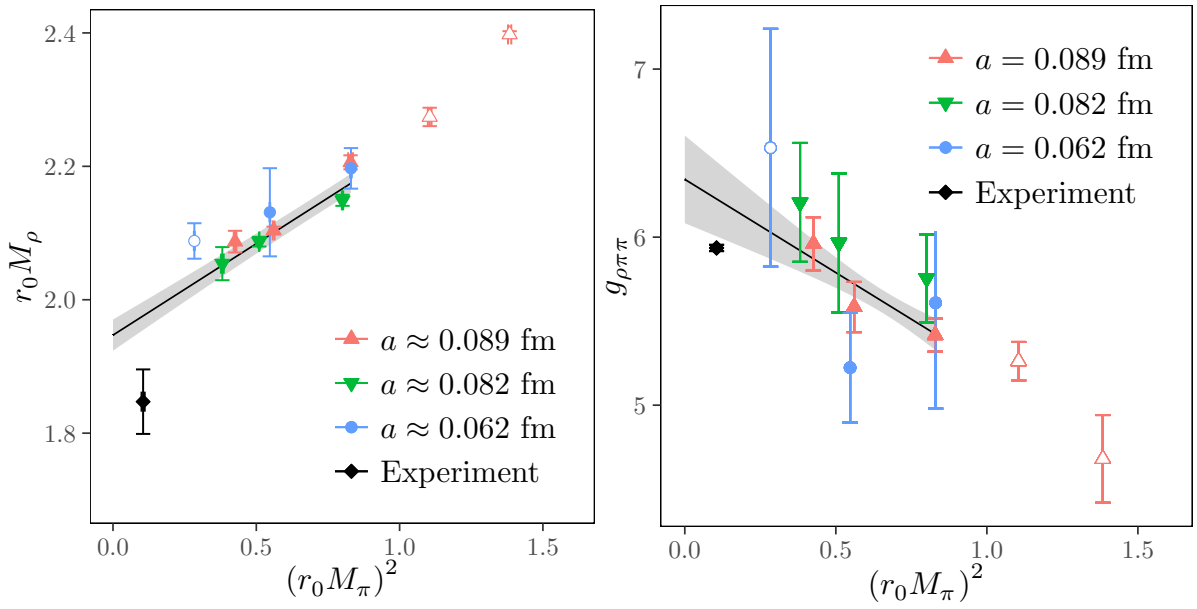

Figure 6.7: In the left panel we show $r_0 M_\rho^{\mathrm{av}}$ as a function of $(r_0 M_\pi)^2$. Open symbols are not included in the fit. In the right panel $g_{\rho\pi\pi}^{\mathrm{av}}$ is shown also as a fucntion of $(r_0 M_\pi)^2$. The lines with error bands represent independent fits to the data.

non-analytic structure in M_ρ is identical to the one of Eq. (6.9).

In order to apply this formula to our lattice data, we re-express it in units of the Sommer parameter r_0

$$r_0^2 Z = r_0^2 Z_\chi + C_\chi (r_0 M_\pi)^2 - \frac{g_{\omega\rho\pi}^2}{24\pi r_0^2} (r_0^2 Z_\chi)^{1/2} (r_0 M_\pi)^3 + \frac{p_{a^2}}{r_0^2} a^2 \tag{6.12}$$

and add an a^2 term, which represents the leading lattice artefacts for the twisted mass formulation at maximal twist. p_{a^2} is an unknown complex parameter.

We first consider M_ρ and $g_{\rho\pi\pi}$. In the left panel of Figure 6.7 we show $r_0 M_\rho^{\mathrm{av}}$, in the right one $g_{\rho\pi\pi}^{\mathrm{av}}$, both as a function of $(r_0 M_\pi)^2$. Note that the error on r_0/a is not included in the plot, because it is 100% correlated for all data points of the same β-value. Colours and symbols encode the three lattice spacing values. The black diamonds represent the corresponding experimental values. The first observation is that lattice artefacts are not resolvable given our current level of statistical uncertainty. Overall, M_ρ appears to show a rather linear dependence on M_π^2, a bit less so $g_{\rho\pi\pi}$. The values for aM_π can be found in Tab. 6.2. For the following extrapolations we correct aM_π for finite size effects by applying a correction factor K_{M_π} computed in Ref. [85], which can also be found in Tab. 6.2.

Next we have tried to fit the pion mass dependence of M_ρ^{av} and $g_{\rho\pi\pi}^{\mathrm{av}}$ combining Eqs. (6.9) and (6.10) up to the order M_π^3. However, such a fit did not result in convincing results. Even though the chiral log in $g_{\rho\pi\pi}^{\mathrm{av}}$ stemming from f_π somewhat compensates the term $c_1 M_\pi^2$, a satisfactory description of the data for both the mass and the coupling could not be achieved.

Therefore, we show in Figure 6.7 independent linear extrapolations for both M_ρ and $g_{\rho\pi\pi}$ in M_π^2. As visible, the extrapolation overestimates both the ρ mass and the coupling at the physical point compared to experiment.

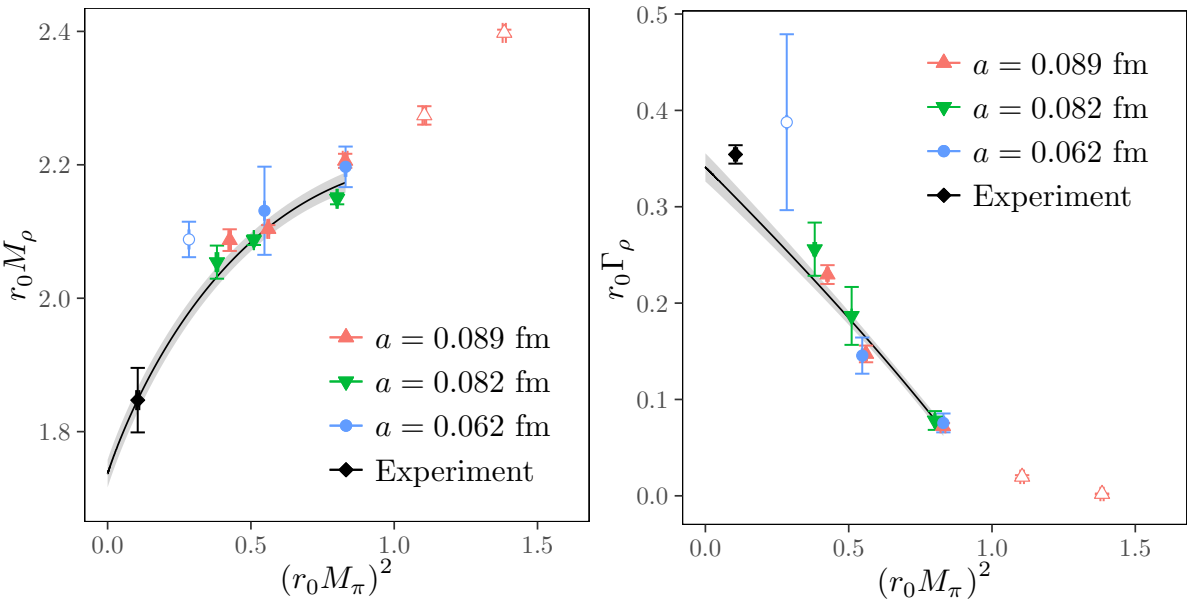

Figure 6.8: Chiral extrapolation of M_ρ and Γ_ρ as a function of M_π^2, all in units of the Sommer parameter r_0. The lattice spacing is colour and symbol coded, the experimental values are shown as black diamonds. The lines with error bands represent combined fits according to Eq. (6.13) to the data of M_ρ and Γ_ρ. Data points with open symbols are not included in the fit.

Therefore, we turn now to fits of mass and width using Eq. (6.12) for the complex valued variable Z. We extrapolate M_ρ and Γ_ρ to the physical point combined in $r_0^2 Z = r_0^2 (M_\rho + \mathrm{i}\Gamma_\rho/2)^2$. As the number of configurations is different for each ensemble, they can not be combined directly. The error analysis for this fit is performed using the parametric bootstrap procedure maintaining the correlation among M_ρ, Γ_ρ and M_π. The parameters are the result of the jackknife analysis. The values for r_0/a for the different lattice spacings were also resampled from the values compiled in Tab. 5.3. As N_{boot} 1500 samples were chosen.

The actual fit function reads

$$a^2 Z = p_{r_0/a}^{-2} \left((p_1 + ip_2) + p_3 \left(p_{r_0/a} a M_\pi \right)^2 - p_4 \sqrt{p_1 + ip_2} \left(p_{r_0/a} a M_\pi \right)^3 + (p_5 + ip_6)\, p_{r_0/a}^{-2} \right) . \tag{6.13}$$

The fit parameters are the following: p_1 and p_2 represent the real and imaginary parts of $r_0^2 Z_\chi$ and p_3 represents C_χ, furthermore $p_4 \equiv g^2_{\omega\rho\pi}/(24\pi r_0^2)$ and p_5 and p_6 parametrise the real and imaginary part of the a^2 lattice artefacts. $p_{r_0/a}$ is one fit parameter per lattice spacing value for r_0/a accompanied by a corresponding prior $P_{r_0/a}$. Thus, we have in total 6 real-valued free fit parameters.

In the fit we include only the ensembles with the largest volume per pion mass value, i.e. A40.24 and B35.32 are not included in the fit. We do not include ensemble D15.48 in the fit, for reasons mentioned above. Moreover, we include only data points with $M_\pi \leq 420$ MeV, which excludes ensembles A80.24 and A100.24.

The best fit parameters can be found in Tab. 6.3 together with the reduced χ^2-value. We give the best fit parameters for fits with and without lattice artefacts included. Clearly, p_5 and p_6,

which parametrise the a^2 effects in Z are compatible with zero. Also, the remaining parameters do not change significantly with and without a^2 artefact included in the fit.

Parameter	incl. a^2	excl. a^2
p_1	3.14(28)	2.99(07)
p_2	-0.631(61)	-0.592(26)
p_3	4.75(24)	4.79(08)
p_4	0.936(80)	0.991(34)
p_5	-5(10)	-
p_6	1.3(1.8)	-
χ^2/d.o.f.	2.35	2.40

Table 6.3: Best fit parameters of the combined chiral fit in terms of Z with and without lattice artefacts included in the fit.

The χ^2-values for these fits are all a bit too large, indicating a tension in the data in particular between M_ρ and Γ_ρ. It basically is a consequence of the invisible curvature in the data for M_ρ.

The result of the fit can be seen in Figure 6.8, where we show in the left panel $r_0 M_\rho$ and in the right panel $r_0 \Gamma_\rho$ both as functions of $(r_0 M_\pi)^2$. Note that the error on r_0/a is not included in the plot, because it is 100% correlated for all data points of the same β-value. The best fit to the data is indicated by the solid lines with error bands. Data points with open symbols are excluded from the fit. The fit range is indicated by the extent of the solid lines. The experimental values are included in both plots as black diamonds, but not included in the fit.

Our final result for M_ρ and Γ_ρ taken from the fit without a a^2 effects included reads

$$M_\rho \;=\; 769(19)\ \text{MeV}\,, \qquad \Gamma_\rho \;=\; 129(7)\ \text{MeV}\,, \tag{6.14}$$

corresponding to

$$g_{\rho\pi\pi} \;=\; 5.5(1)\,. \tag{6.15}$$

In addition we find

$$\begin{aligned} M_\rho^0 \;&=\; 723(20)\ \text{MeV}\,, \\ \Gamma_\rho^0 \;&=\; 142(7)\ \text{MeV}\,, \\ |g_{\omega\rho\pi}| \;&=\; 20.8(7)\ \text{GeV}^{-1} \end{aligned} \tag{6.16}$$

from our chiral and continuum fits.

6.5 Discussion

The final result for M_ρ and Γ_ρ we quote in Eq. (6.14) can be compared to the corresponding PDG values [38] for mass and full width

$$M_\rho^{\text{exp}} = 775.26(25)\,\text{MeV} \tag{3.2}$$

$$\Gamma_\rho^{\text{exp}} = 149.1(8)\,\text{MeV}\,. \tag{3.3}$$

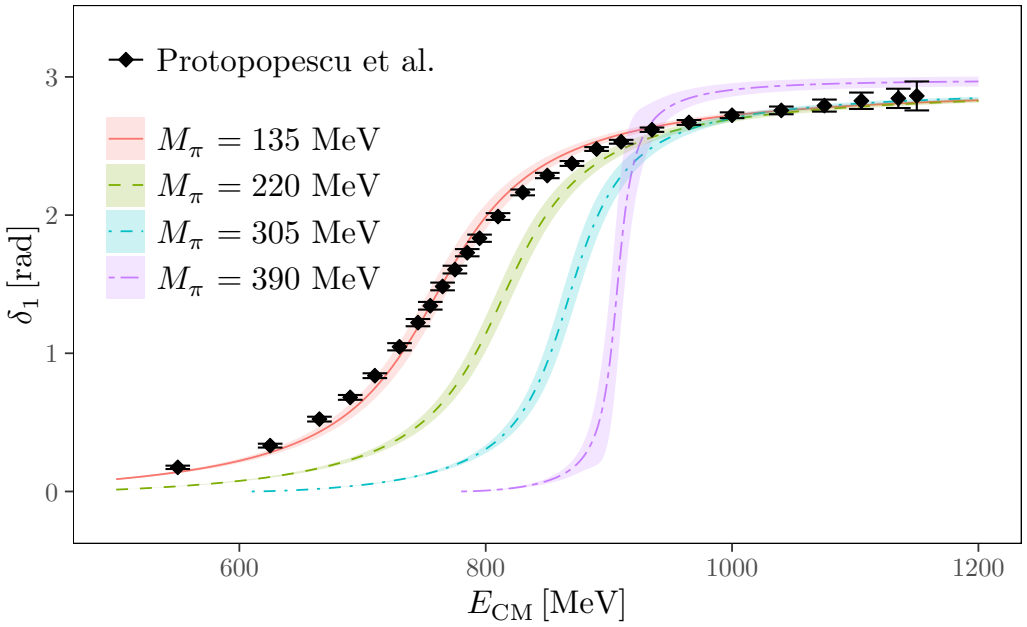

Figure 6.9: Comparison of experimental phase shift data from Ref. [15] to the phase shift curve extracted from our final results for M_ρ and Γ_ρ shown as red solid line. For illustration purposes we also show the phase shift curve in a world with $M_\pi = 220$ MeV as green dashed line, with $M_\pi = 305$ MeV as blue dot-dashed line and with 390 MeV as a purple two-dashed line.

While M_ρ agrees rather well, the width is slightly too low. This is also visible in Figure 6.9, where we plot the experimental phase shifts from Ref. [15] and compare them to the phase shift curve we obtain by evaluating Eq. (6.7) at the final values Eq. (6.14).

However, this good agreement should be taken with caution. First of all our extrapolation form for M_ρ and Γ_ρ is not model independent. This is in particular important, because the curvature needed to obtain an M_ρ-value close to the experimental one comes from constrains due to Γ_ρ. This, as discussed earlier, manifests itself also in a bit too large χ^2-values in the chiral and continuum fits. Moreover, the ensemble with the lightest pion mass included in the fit is B35.48 with a pion mass of about 300 MeV. Thus, the extrapolation to the physical point is quite long. In addition we have assumed that we can perform a Breit-Wigner type fit to all the phase shift data, which is an approximation. This might also be the reason for the too low value of Γ_ρ compared to experiment. Our fitted value for $g_{\omega\rho\pi}$ Eq. (6.16) is in the right ballpark, when compared to the numbers given in Refs. [96, 97], where 16 GeV^{-1} is quoted. From Refs. [9, 99] one finds $g_{\omega\rho\pi} = \pm 20.7$ GeV^{-1} in very good agreement with our value.

Finally, our determinations of mass and width rest on the assumption that all partial waves apart from $\ell = 1$ are negligible. This assumption is supported by previous lattice investigations of the ρ meson, but has not been checked by us yet.

On the other hand, this work is the first consistent extrapolation to the physical point and to the continuum limit. Due to the comparatively high number of ensembles used in this work, we were able to fully take into account lattice artifacts and partially evaluate the influence of finite volume effects. We found no statistically significant evidence for a dependence on the lattice spacing in our results. Furthermore we found reason to argue that finite volume effects are not a dominant source of uncertainty in our results either.

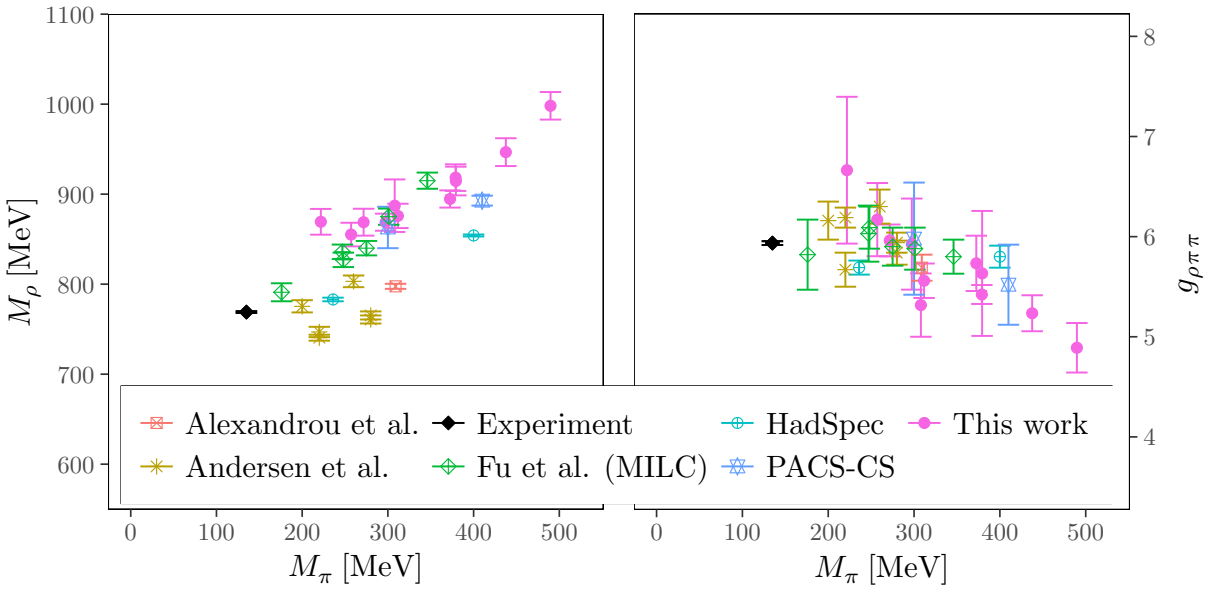

Figure 6.10: Comparison of lattice results for M_ρ (left) and $g_{\rho\pi\pi}$ (right) as a function of M_π. We compare with all available results that had a dynamic strange quark: Alexandrou et al. [32], Andersen et al. [33], Fu et al. [30], HadSpec [27, 29], PACS-CS [26] as well as the experimental value [38].

In Figure 6.10 we compare results for M_ρ and $g_{\rho\pi\pi}$ from various lattice collaborations with $N_f = 2 + 1$ or $N_f = 2 + 1 + 1$ dynamical quark flavours. We observe that there are probably lattice artefacts in some of the results for M_ρ, in particular in the results from Andersen et *al.* [33] and from the Hadron Spectrum Collaboration [27]. For $g_{\rho\pi\pi}$ uncertainties are in general larger and within these large uncertainties the agreement among different lattice collaborations is reasonable.

CHAPTER 7

Summary

In this thesis the ρ-meson properties were investigated using lattice QCD with $N_f = 2 + 1 + 1$ Wilson twisted mass quarks at maximal twist. The ρ-meson is one of the lightest and arguably the simplest resonance in the standard model of particle physics and experimentally known to very high precision. Nevertheless or maybe for this very reason reproducing the experimental results is an important milestone on the way to investigate other resonances with lattice QCD.

The investigation of resonances entails several technical challenges. Utilizing arbitrary moving frames causes a nontrivial splitting of spin multiplets. While this effect has been discussed before, this work adds a group theoretical perspective and detailed derivations that hopefully prove useful for future generalizations.

The phase shift curves have been determined applying Lüscher's method using moving frames up to $\boldsymbol{d}^2 = 4$ and all available lattice irreducible representations. With three values of the lattice spacing and a range of pion mass values we could perform chiral and continuum extrapolations of ρ-meson mass M_ρ and width Γ_ρ with better control than previously possible. Under the assumption that partial waves with $l \geq 3$ are negligible these two quantities have been determined on our ensembles using a Breit-Wigner type fit to phase shift data.

From a combined continuum and chiral extrapolation of M_ρ and Γ_ρ the final results

$$M_\rho \;=\; 769(19)\ \text{MeV}\,, \qquad g_{\rho\pi\pi} \;=\; 5.5(1)\,, \qquad \Gamma_\rho \;=\; 129(7)\ \text{MeV}$$

have been determined.

Systematic errors from thermal state pollutions, the chiral and the continuum extrapolation were carefully examined and should be covered by the error we quote. M_ρ is very close to its experimental value but the width is about two sigma too low. The agreement of our data for M_ρ with previously published lattice results is satisfactory.

To further improve the calculation of resonances with lattice QCD, more work needs to be done to better estimate the width. It likely suffers from e.g. the use of a Breit-Wigner type fit to the phase shift data. More sophisticated models such as the inverse amplitude method [100–104] would be capable to directly describe the pion mass dependence of the phase shift curves. This will be the next step to alleviate systematic uncertainties in our current analysis and therefore allow performing the chiral extrapolation even more reliably.

Bibliography

[1] M. Werner et al.,
Hadron-Hadron Interactions from $N_f = 2 + 1 + 1$ Lattice QCD: The ρ-resonance, (2019), arXiv: 1907.01237 [hep-lat].

[2] F. Jegerlehner, *Muon g – 2 theory: The hadronic part*,
EPJ Web Conf. **166** (2018) p. 00022, arXiv: 1705.00263 [hep-ph].

[3] S. Weinberg, *Phenomenological Lagrangians*, Physica **A96** (1979) p. 327.

[4] J. Gasser and H. Leutwyler, *Chiral Perturbation Theory to One Loop*,
Ann. Phys. **158** (1984) p. 142.

[5] J. Gasser and H. Leutwyler,
Chiral Perturbation Theory: Expansions in the Mass of the Strange Quark,
Nucl. Phys. **B250** (1985) p. 465.

[6] G. Colangelo, J. Gasser, and H. Leutwyler, *$\pi\pi$ scattering*,
Nucl.Phys. **B603** (2001) p. 125, arXiv: hep-ph/0103088 [hep-ph].

[7] R. Garcia-Martin et al., *Precise determination of the f0(600) and f0(980) pole parameters from a dispersive data analysis*, Phys. Rev. Lett. **107** (2011) p. 072001, arXiv: 1107.1635 [hep-ph].

[8] K. G. Wilson, *Confinement of Quarks*, Phys. Rev. **D10** (1974) p. 2445, [,319(1974)].

[9] U.-G. Meißner,
Low-Energy Hadron Physics from Effective Chiral Lagrangians with Vector Mesons,
Phys. Rept. **161** (1988) p. 213.

[10] A. R. Erwin et al., *Evidence for a $\pi - \pi$ Resonance in the $I = 1$, $J = 1$ State*,
Phys. Rev. Lett. **6** (1961) p. 628.

[11] A. R. Erwin et al., *Erratum: Evidence for a $\pi - \pi$ Resonance in the $I = 1$, $J = 1$ State*,
Phys. Rev. Lett. **7** (1961) p. 39.

[12] E. Pickup, D. K. Robinson, and E. O. Salant,
$\pi\pi$ Resonance in $\pi^- - p$ Interactions at 1.25 Bev, Phys. Rev. Lett. **7** (1961) p. 192.

[13] E. Pickup, D. K. Robinson, and E. O. Salant,
Erratum: $\pi - \pi$ Resonance in $\pi^- - p$ Interactions at 1.25 Bev,
Phys. Rev. Lett. **7** (1961) p. 472.

[14] D. Stonehill et al., *Pion-Pion Interaction in Pion Production by $\pi^+ - p$ Collisions*,
Phys. Rev. Lett. **6** (1961) p. 624.

[15] S. D. Protopopescu et al., *Pi pi Partial Wave Analysis from Reactions pi+ p —> pi+ pi- Delta++ and pi+ p —> K+ K- Delta++ at 7.1-GeV/c*, Phys. Rev. **D7** (1973) p. 1279.

[16] M. Lüscher, *Volume Dependence of the Energy Spectrum in Massive Quantum Field Theories. 1. Stable Particle States*, Commun.Math.Phys. **104** (1986) p. 177.

[17] M. Lüscher, *Volume Dependence of the Energy Spectrum in Massive Quantum Field Theories. 2. Scattering States*, Commun.Math.Phys. **105** (1986) p. 153.

[18] M. Lüscher, *Two particle states on a torus and their relation to the scattering matrix*, Nucl.Phys. **B354** (1991) p. 531.

[19] R. A. Briceño, J. J. Dudek, and R. D. Young, *Scattering processes and resonances from lattice QCD*, Rev. Mod. Phys. **90** (2018) p. 025001, arXiv: 1706.06223 [hep-lat].

[20] K. Rummukainen and S. A. Gottlieb, *Resonance scattering phase shifts on a nonrest frame lattice*, Nucl.Phys. **B450** (1995) p. 397, arXiv: hep-lat/9503028 [hep-lat].

[21] X. Feng, K. Jansen, and D. B. Renner, *Resonance Parameters of the rho-Meson from Lattice QCD*, Phys. Rev. **D83** (2011) p. 094505, arXiv: 1011.5288 [hep-lat].

[22] M. Göckeler et al., *Scattering phases for meson and baryon resonances on general moving-frame lattices*, Phys.Rev. **D86** (2012) p. 094513, arXiv: 1206.4141 [hep-lat].

[23] C. McNeile and C. Michael, *Hadronic decay of a vector meson from the lattice*, Phys. Lett. **B556** (2003) p. 177, arXiv: hep-lat/0212020 [hep-lat].

[24] C. Michael, *Hadronic decays from the lattice*, Eur. Phys. J. **A31** (2007) p. 793, arXiv: hep-lat/0609008 [hep-lat].

[25] C. B. Lang et al., *Coupled channel analysis of the rho meson decay in lattice QCD*, Phys. Rev. **D84** (2011) p. 054503, [Erratum: Phys. Rev.D89,no.5,059903(2014)], arXiv: 1105.5636 [hep-lat].

[26] S. Aoki et al., *ρ Meson Decay in 2+1 Flavor Lattice QCD*, Phys. Rev. **D84** (2011) p. 094505, arXiv: 1106.5365 [hep-lat].

[27] J. J. Dudek, R. G. Edwards, and C. E. Thomas, *Energy dependence of the ρ resonance in $\pi\pi$ elastic scattering from lattice QCD*, Phys. Rev. **D87** (2013) p. 034505, [Erratum: Phys. Rev.D90,no.9,099902(2014)], arXiv: 1212.0830 [hep-ph].

[28] G. S. Bali et al., *ρ and K^* resonances on the lattice at nearly physical quark masses and $N_f = 2$*, Phys. Rev. **D93** (2016) p. 054509, arXiv: 1512.08678 [hep-lat].

[29] D. J. Wilson et al., *Coupled $\pi\pi, K\bar{K}$ scattering in P-wave and the ρ resonance from lattice QCD*, Phys. Rev. **D92** (2015) p. 094502, arXiv: 1507.02599 [hep-ph].

[30] Z. Fu and L. Wang, *Studying the ρ resonance parameters with staggered fermions*, Phys. Rev. **D94** (2016) p. 034505, arXiv: 1608.07478 [hep-lat].

[31] D. Guo et al., *Rho resonance parameters from lattice QCD*, Phys. Rev. **D94** (2016) p. 034501, arXiv: 1605.03993 [hep-lat].

[32] C. Alexandrou et al., *P-wave $\pi\pi$ scattering and the ρ resonance from lattice QCD*, Phys. Rev. **D96** (2017) p. 034525, arXiv: 1704.05439 [hep-lat].

[33] C. Andersen et al., *The $I = 1$ pion-pion scattering amplitude and timelike pion form factor from $N_{\mathrm{f}} = 2 + 1$ lattice QCD*, Nucl. Phys. **B939** (2019) p. 145, arXiv: 1808.05007 [hep-lat].

[34] J. J. Dudek, R. G. Edwards, and C. E. Thomas, *Energy dependence of the ρ resonance in $\pi\pi$ elastic scattering from lattice QCD*, Phys. Rev. D **87** (2013), ISSN: 15507998, arXiv: arXiv:1212.0830v1.

[35] R. Baron et al., *Light hadrons from lattice QCD with light (u,d), strange and charm dynamical quarks*, JHEP **06** (2010) p. 111, arXiv: 1004.5284 [hep-lat].

[36] R. Baron et al., *Computing K and D meson masses with N_f = 2+1+1 twisted mass lattice QCD*, Comput.Phys.Commun. **182** (2011) p. 299, arXiv: 1005.2042 [hep-lat].

[37] S. Weinberg, *The Quantum theory of fields. Vol. 1: Foundations*, Cambridge University Press, 2005, chap. 3, ISBN: 9780521670531, 9780511252044.

[38] M. Tanabashi et al., *Review of Particle Physics*, Phys. Rev. **D98** (2018) p. 030001.

[39] C. Gattringer and C. Lang, *Quantum chromodynamics on the lattice: an introductory presentation*, vol. 788, Springer Science & Business Media, 2009.

[40] Y. Iwasaki and T. Yoshie, *Renormalization Group Improved Action for SU(3) Lattice Gauge Theory and the String Tension*, Phys. Lett. **143B** (1984) p. 449.

[41] H. B. Nielsen and M. Ninomiya, *No Go Theorem for Regularizing Chiral Fermions*, Phys. Lett. **105B** (1981) p. 219.

[42] S. Sint, "Lattice QCD with a chiral twist", *Perspectives In Lattice QCD*, World Scientific, 2008 p. 169.

[43] R. Frezzotti et al., *Lattice QCD with a chirally twisted mass term*, J. High Energy Phys. **2001** (2001) p. 58, ISSN: 10298479, arXiv: 0101001 [hep-lat], URL: http://arxiv.org/abs/hep-lat/0101001.

[44] C. Pena et al., *Chirally improving Wilson fermions 1. O(a) improvement*, J. High Energy Phys. **2004** (2004) p. 007.

[45] G. Herdoiza et al., *Determination of Low-Energy Constants of Wilson Chiral Perturbation Theory*, JHEP **05** (2013) p. 038, arXiv: 1303.3516 [hep-lat].

[46] N. Metropolis et al., *Equation of state calculations by fast computing machines*, The journal of chemical physics **21** (1953) p. 1087.

[47] S. Duane et al., *Hybrid monte carlo*, Physics letters B **195** (1987) p. 216.

[48] L. Maiani and M. Testa, *Final state interactions from euclidean correlation functions*, Phys. Lett. B **245** (1990) p. 585, ISSN: 03702693.

[49] K. Polejaeva and A. Rusetsky, *Three particles in a finite volume*, Eur.Phys.J. **A48** (2012) p. 67, arXiv: 1203.1241 [hep-lat].

[50] R. A. Briceño, M. T. Hansen, and S. R. Sharpe,
Three-particle systems with resonant subprocesses in a finite volume,
Phys. Rev. **D99** (2019) p. 014516, arXiv: 1810.01429 [hep-lat].

[51] F. Romero-López, A. Rusetsky, and C. Urbach,
Two- and three-body interactions in φ^4 theory from lattice simulations,
Eur. Phys. J. **C78** (2018) p. 846, arXiv: 1806.02367 [hep-lat].

[52] J.-Y. Pang et al., *Energy shift of the three-particle system in a finite volume*,
Phys. Rev. **D99** (2019) p. 074513, arXiv: 1902.01111 [hep-lat].

[53] M. T. Hansen and S. R. Sharpe, *Lattice QCD and Three-particle Decays of Resonances*,
(2019), arXiv: 1901.00483 [hep-lat].

[54] V. Bernard et al., *Resonance properties from the finite-volume energy spectrum*,
JHEP **0808** (2008) p. 024, arXiv: 0806.4495 [hep-lat].

[55] S. Altmann and P. Herzig, *Point-group theory tables*, Oxford, 1994.

[56] A. Schoenflies, *Krystallsysteme und Krystallstructur*,
Druck und Verlag von BG Teubner, 1891.

[57] R. C. Johnson, *ANGULAR MOMENTUM ON A LATTICE*,
Phys. Lett. **114B** (1982) p. 147.

[58] J. E. Mandula and E. Shpiz,
Doubled Valued Representations of the Four-dimensional Cubic Lattice Rotation Group,
Nucl. Phys. **B232** (1984) p. 180.

[59] J. E. Mandula, G. Zweig, and J. Govaerts, *Representations of the Rotation Reflection Symmetry Group of the Four-dimensional Cubic Lattice*, Nucl. Phys. **B228** (1983) p. 91.

[60] D. C. Moore and G. T. Fleming,
Angular momentum on the lattice: The Case of non-zero linear momentum,
Phys. Rev. **D73** (2006) p. 014504, [Erratum: Phys. Rev.D74,079905(2006)],
arXiv: hep-lat/0507018 [hep-lat].

[61] D. C. Moore and G. T. Fleming,
Multiparticle States and the Hadron Spectrum on the Lattice,
Phys. Rev. **D74** (2006) p. 054504, arXiv: hep-lat/0607004 [hep-lat].

[62] M. Hamermesh, *Group theory and its application to physical problems*,
Courier Corporation, 2012.

[63] L. P. Bouckaert, R. Smoluchowski, and E. Wigner,
Theory of Brillouin zones and symmetry properties of wave functions in crystals,
Physical Review **50** (1936) p. 58.

[64] S. L. Altmann and A. P. Cracknell, *Lattice Harmonics I. Cubic Groups*,
Rev. Mod. Phys. **37** (1965) p. 19, ISSN: 0034-6861,
URL: https://link.aps.org/doi/10.1103/RevModPhys.37.19.

[65] Wikipedia contributors, *Plagiarism — Wikipedia, The Free Encyclopedia*,
[Online; accessed 26-June-2019], 2019,
URL: https://en.wikipedia.org/w/index.php?title=Plagiarism&oldid=5139350.

[66] C. Michael and I. Teasdale, *Extracting Glueball Masses From Lattice QCD*,
Nucl. Phys. **B215** (1983) p. 433.

[67] M. Lüscher and U. Wolff, *How to Calculate the Elastic Scattering Matrix in Two-dimensional Quantum Field Theories by Numerical Simulation*, Nucl. Phys. **B339** (1990) p. 222.

[68] B. Blossier et al., *On the generalized eigenvalue method for energies and matrix elements in lattice field theory*, JHEP **04** (2009) p. 094, arXiv: 0902.1265 [hep-lat].

[69] B. C. Maglić et al., *Evidence for a $T = 0$ Three-Pion Resonance*, Phys. Rev. Lett. **7** (1961) p. 178.

[70] D. L. Stonehill and H. L. Kraybill, *Pion-Pion Interactions in $\pi^+ - p$ Collisions*, Rev. Mod. Phys. **34** (1962) p. 503.

[71] S. D. Protopopescu et al., *$\pi\pi$ Partial-Wave Analysis from Reactions $\pi^+ p \to \pi^+\pi^+\Delta^{++}$ and $\pi^+ p \to K^+K^-\Delta^{++}$ at $7.1 GeV/c$*, Phys. Rev. D **7** (1973) p. 1279.

[72] M. Tanabashi et al., *Review of particle physics*, Physical Review D **98** (2018) p. 030001.

[73] F. Jegerlehner and R. Szafron, *$\rho^0 - \gamma$ mixing in the neutral channel pion form factor F_π^e and its role in comparing e^+e^- with τ spectral functions*, Eur. Phys. J. **C71** (2011) p. 1632, arXiv: 1101.2872 [hep-ph].

[74] C. Michael and C. Urbach, *Neutral mesons and disconnected diagrams in Twisted Mass QCD*, PoS **LATTICE2007** (2007) p. 122, arXiv: 0709.4564 [hep-lat].

[75] F. Halzen and A. D. Martin, *Quark & Leptons: An Introductory Course In Modern Particle Physics*, John Wiley & Sons, 2008.

[76] S. Aoki et al., *Lattice QCD Calculation of the rho Meson Decay Width*, Phys. Rev. **D76** (2007) p. 094506, arXiv: 0708.3705 [hep-lat].

[77] R. Frezzotti and G. C. Rossi, *Chirally improving Wilson fermions. I: O(a) improvement*, JHEP **08** (2004) p. 007, eprint: hep-lat/0306014.

[78] R. Frezzotti and G. C. Rossi, *Twisted-mass lattice QCD with mass non-degenerate quarks*, Nucl. Phys. Proc. Suppl. **128** (2004) p. 193, eprint: hep-lat/0311008.

[79] R. Frezzotti and G. C. Rossi, *Chirally improving Wilson fermions. II: Four-quark operators*, JHEP **10** (2004) p. 070, arXiv: hep-lat/0407002.

[80] P. Boucaud et al., *Dynamical Twisted Mass Fermions with Light Quarks: Simulation and Analysis Details*, Comput.Phys.Commun. **179** (2008) p. 695, arXiv: 0803.0224 [hep-lat].

[81] D. Djukanovic, *Quark Contraction Tool - QCT*, (2016), arXiv: 1603.01576 [hep-lat].

[82] J. J. Dudek, R. G. Edwards, and C. E. Thomas, *S and D-wave phase shifts in isospin-2 pi pi scattering from lattice QCD*, Phys. Rev. **D86** (2012) p. 034031, arXiv: 1203.6041 [hep-ph].

[83] C. Helmes et al., *Hadron-Hadron Interactions from $N_f = 2 + 1 + 1$ Lattice QCD: $I = 3/2$ πK Scattering Length*, Phys. Rev. **D98** (2018) p. 114511, arXiv: 1809.08886 [hep-lat].

[84] T. Chiarappa et al., *Numerical simulation of QCD with u, d, s and c quarks in the twisted-mass Wilson formulation*, Eur.Phys.J. **C50** (2007) p. 373, arXiv: hep-lat/0606011 [hep-lat].

[85] N. Carrasco et al., *Up, down, strange and charm quark masses with N_f = 2+1+1 twisted mass lattice QCD*, Nucl.Phys. **B887** (2014) p. 19, arXiv: 1403.4504 [hep-lat].

[86] S. Aoki et al., *Review of lattice results concerning low-energy particle physics*, Eur. Phys. J. **C77** (2017) p. 112, arXiv: 1607.00299 [hep-lat].

[87] C. Morningstar et al., *Improved stochastic estimation of quark propagation with Laplacian Heaviside smearing in lattice QCD*, Phys.Rev. **D83** (2011) p. 114505, arXiv: 1104.3870 [hep-lat].

[88] M. Peardon et al., *A Novel quark-field creation operator construction for hadronic physics in lattice QCD*, Phys. Rev. **D80** (2009) p. 054506, arXiv: 0905.2160 [hep-lat].

[89] C. Helmes et al., *Hadron-hadron interactions from N_f = 2 + 1 + 1 lattice QCD: isospin-2 $\pi\pi$ scattering length*, JHEP **09** (2015) p. 109, arXiv: 1506.00408 [hep-lat].

[90] C. Helmes et al., *Hadron-Hadron Interactions from $N_f = 2 + 1 + 1$ lattice QCD: Isospin-1 KK scattering length*, Phys. Rev. **D96** (2017) p. 034510, arXiv: 1703.04737 [hep-lat].

[91] J. Bulava et al., *Two-particle Correlation Functions with Distilled Propagators*, PoS **LAT2009** (2009) p. 097, arXiv: 0911.2044 [hep-lat].

[92] L. S. Brown and R. L. Goble, *Pion-Pion Scattering, Current Algebra, Unitarity, and the Width of the Rho Meson*, Phys. Rev. Lett. **20** (1968) p. 346.

[93] P. C. Bruns and U.-G. Meißner, *Infrared regularization for spin-1 fields*, Eur. Phys. J. **C40** (2005) p. 97, arXiv: hep-ph/0411223 [hep-ph].

[94] K. Kawarabayashi and M. Suzuki, *Partially conserved axial vector current and the decays of vector mesons*, Phys. Rev. Lett. **16** (1966) p. 255.

[95] Riazuddin and Fayyazuddin, *Algebra of current components and decay widths of rho and K* mesons*, Phys. Rev. **147** (1966) p. 1071.

[96] D. Djukanovic et al., *Complex-mass renormalization in chiral effective field theory*, Phys. Lett. **B680** (2009) p. 235, arXiv: 0902.4347 [hep-ph].

[97] D. Djukanovic et al., *Complex mass renormalization in EFT*, PoS **CD09** (2009) p. 050, arXiv: 1001.1772 [hep-ph].

[98] G. Ecker et al., *Chiral Lagrangians for Massive Spin 1 Fields*, Phys. Lett. **B223** (1989) p. 425.

[99] N. Kaiser and U.-G. Meißner, *Generalized hidden symmetry for low-energy hadron physics*, Nucl. Phys. **A519** (1990) p. 671.

[100] T. N. Truong, *Remarks on the unitarization methods*,
Phys. Rev. Lett. **67** (1991) p. 2260.

[101] A. Dobado and J. R. Pelaez,
A Global fit of pi pi and pi K elastic scattering in ChPT with dispersion relations,
Phys. Rev. **D47** (1993) p. 4883, arXiv: hep-ph/9301276 [hep-ph].

[102] A. Dobado and J. R. Pelaez, *The Inverse amplitude method in chiral perturbation theory*,
Phys. Rev. **D56** (1997) p. 3057, arXiv: hep-ph/9604416 [hep-ph].

[103] A. Gomez Nicola, J. R. Pelaez, and G. Rios,
The Inverse Amplitude Method and Adler Zeros, Phys. Rev. **D77** (2008) p. 056006,
arXiv: 0712.2763 [hep-ph].

[104] M. Niehus, M. Hoferichter, and B. Kubis, "Quark mass dependence of $\gamma^*\pi \to \pi\pi$",
9th International Workshop on Chiral Dynamics (CD18) Durham, NC, USA, September 17-21, 2018, 2019, arXiv: 1902.10150 [hep-ph].

[105] T. Hahn and H. Klapper, *Crystallographic and noncrystallographic point groups*,
International Tables for Crystallography (2006).

APPENDIX A

Appendix

A.1 Point Group Theory Tables

There are 24 proper rotations, that leave a cube invariant. Amongst themselves they already form group so-called chiral / rotational octahedral group O wich falls into $N_{\mathcal{C}} = 5$ conjugacy classes.

E: Identity

3C2: Rotation about face-centered axes by π

8C3: Rotation about body diagonals (corner-centered axes) by $2\pi/3$

6C4: Like 3C2, but by $\pm\pi/2$

6C′2: Rotation about edge-centered axes by π

With the exception of E, the first number in the respective names decode the number of elements belonging to a given conjugacy class. $\mathbf{C}^{(\prime)}$ denotes a proper rotation axes and the last number gives the rotation angle as a fraction of 2π. Implicitly the largest angle defines a principal axis which is conventional chosen in the z direction. In this example it is a rotation by π about a face-centered axis.

The number of irreducible representations (irreps) is equal to the number of conjugacy classes. $N_\Gamma = N_{\mathcal{C}}$. Their dimensions squared must partition the order of the group

$$24 = \sum_{i=1}^{N_\Gamma} |\Gamma_i|^2$$

In conjunction with several orthogonality theorems yields one obtains the partition $24 = 1^2 + 1^2 + 2^2 + 3^2 + 3^2$. There are two one-dimensional, one two-dimensional and two three-dimension irreps labeled A1, A2, E, T1 and T2. The character table is given in Tab. A.1. A always denotes singly-degenerate, E always doubly-degenerate and T always triply-degenerate representations. In addition to A, B will denote singly-degenerate representations which are antisymmetrical with respect to a rotation about the principal axis. A1 always is the trivial representation.

The symmetry group of inversions is $\mathrm{C_i}$. It contains only two elements and falls into $N_{\mathcal{C}} = 2$ conjugacy classes. The conjugacy classes are denoted

O	**E**	**3C2**	**8C3**	**6C4**	**6C′2**
A1	1	1	1	1	1
A2	1	1	1	−1	−1
E	2	2	−1	0	0
T1	3	−1	0	1	−1
T2	3	−1	0	−1	1

Table A.1: Character Table of O the group of proper rotations of an octahadron.

E: Identity

i: Inversion

C_i has two irreducible representations, A_g and A_u. As suggested by the letter A both these

C_i	**E**	**i**
A	1	1
A2	1	−1

Table A.2: Character Table of C_i the group of inversion.

representations are one-dimensional. The index g and u of the irreps abbreviates "gerade" (even) and "ungerade" (odd). In the matrix representation of A_g all elements are 1. An even state is therefore invariant under spatial inversion. On the contrary the matrix representation of A_u has a -1 for the spatial inversion, thus odd states change sign under spatial inversion.

As there is only one group with two elements C_i is of course congruent to the mirror group which will be denoted as C_s for distinction.

$d^2 = 0$: The group O_h As mentioned before, the restricted symmetry group for the lattice in the rest frame is the group of proper and improper rotations that leave a cube invariant. The latter are also often called "rotoflections" and we use "full rotoflections" when we mean both. It is the direct product of the rotation group O and reflection group $C_t exti$:

$$O_h = O \otimes C_i \,.$$

In comparison to O it has twice as many elements $|O_h| = 48$. It consists of $N_{\mathcal{C}} = 10$ conjugacy classes. The classes of O are retained and supplemented by

i: Inversion

3σ: Reflection in planes perpendicular to a face-centered axis

$8S_6$: Rotoflections with rotation by $\pi/6$

$6S_4$: Rotoflections with rotation by $\pi/4$

$6\sigma_d$: Reflection in planes perpendicular to an edge-centered axis

$\boldsymbol{\sigma}$ denotes mirror planes and **S** denotes improper rotation axes.

According to $N_{\mathcal{C}}$, the number of irreducible representations is $N_\Gamma = 10$ as well. All irreps of Tab: A.1 appear twice. The character table is given in Tab. A.3. As one would naively expect,

O_h	**E**	**3C2**	**8C3**	**6C4**	**6C′2**	**i**	**3σ**	**8S$_6$**	**6S$_4$**	**6σ$_d$**
$A1_g$	1	1	1	1	1	1	1	1	1	1
$A2_g$	1	1	1	−1	−1	1	1	1	−1	−1
E_g	2	2	−1	0	0	2	2	−1	0	0
$T1_g$	3	−1	0	1	−1	3	−1	0	1	−1
$T2_g$	3	−1	0	−1	1	3	−1	0	−1	1
$A1_u$	1	1	1	1	1	−1	−1	−1	−1	−1
$A2_u$	1	1	1	−1	−1	−1	−1	−1	1	1
E_u	2	2	−1	0	0	−2	−2	1	0	0
$T1_u$	3	−1	0	1	−1	−3	1	0	−1	1
$T2_u$	3	−1	0	−1	1	−3	1	0	1	−1

Table A.3: Character Table of O_h the group of full rotoflections of an octahedron.

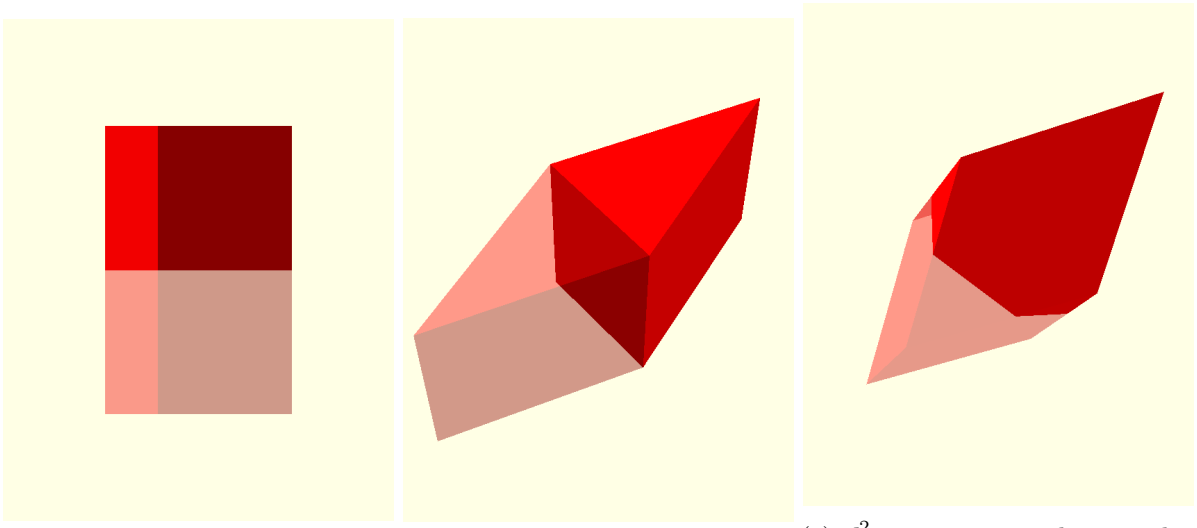

(a) $\boldsymbol{d}^2 = 1, 4$: Rectangular prism (b) $\boldsymbol{d}^2 = 2$: Right rhombic prism (c) $\boldsymbol{d}^2 = 3$: Truncated triangular prism

Figure A.1: Distorted geometries for the different boosts applied in this work. The transparent color is used to clarify thet reflection in the plane perpendicular to the CM momentum is not a symmetry of the lattice

because parity is still conserved the odd irreps are just augmented by an additional minus sign in all conjugacy classes that involve inversion.

$\boldsymbol{d}^2 = 1, 4$: The group C_{4v} When $\boldsymbol{d}^2 = 1$ or 4 the cube is boosted along a face-centered axis e.g. $(0, 0, 1)$ or $(0, 0, 2)$. To an observer in the rest frame the geometrical figure appears as rectangular prism as shown in Fig. A.1(a) which is invariant under rotations from the dihedral group with reflections perpendicular to the principal axis, $D_{4h} \subset O_h$. However, the prism is oriented because the direction of $\boldsymbol{p}_{cm}$ would change under the reflection in the plane perpendicular to it. D_{4h} must be further restricted by taking the factor group $C_{4v} \cong D_{4h}/C_s$ without this reflection.[1]

[1] As $C_s \cong C_i$, C_{4v} is congruent to the dihedral group of a rectangle $D_4 \equiv Dih_4 \cong D_{4h}/C_i$. This distinction is necessary because in the lattice community usually the double cover of C_{4v} is denoted by the dicyclic group Dic_4 [60, 82]

This is the point group of a ditetragonal pyramid [105]

C_{4v} contains only four elements and falls into $N_{\mathcal{C}} = 4$ conjugacy classes.

E: Identity

2C4: Rotation about $\boldsymbol{p}_{\mathrm{cm}}$ by $\pi/4$

C2: Rotation about $\boldsymbol{p}_{\mathrm{cm}}$ by $\pi/2$

$2\sigma_v$: Reflection in planes perpendicular to a face-centered axis

$2\sigma_d$: Reflection in planes perpendicular to an edge-centered axis

According to $N_{\mathcal{C}}$, the number of irreducible representations is $N_\Gamma = 5$ as well. The character table is given in Tab. A.4.

O	**E**	**2C4**	**C2**	**$2\sigma_v$**	**$2\sigma_d$**
A1	1	1	1	1	1
A2	1	1	1	−1	−1
B1	1	−1	1	1	−1
B2	1	−1	1	−1	1
E	2	0	−2	0	0

Table A.4: Character Table of C_{4v} the group of full rotoflections of a ditetragonal pyramid.

$d^2 = 1, 4$: The group C_{2v} When $d^2 = 2$ the cube is boosted along an edge-centered axis e.g. $(1, 1, 0)$. To an observer in the rest frame the geometrical figure appears as a right rhombic prism as shown in Fig. A.1(b) which is invariant under $D_{2h} \subset O_h$. Again a reflection in the plane perpendicular to $\boldsymbol{p}_{\mathrm{cm}}$ would change its sign. The factor group $C_{2v} \cong D_{2h}/C_s$ without this reflection is the point group of a rhombic pyramid [105]

C_{2v} has only four elements and falls into $N_{\mathcal{C}} = 4$ conjugacy classes. The remaining reflections in planes perpendicular to a face-centered axis ($\mathbf{3}\sigma$ of O_h) fall into a class of their own.

E: Identity

C2: Rotation about $\boldsymbol{p}_{\mathrm{cm}}$ by $\pi/2$

σ_x: Reflection in plane perpendicular to a face-centered axis

σ_y: Reflection in plane perpendicular to a face-centered axis

According to $N_{\mathcal{C}}$, the number of irreducible representations is $N_\Gamma = 4$ as well. The character table is given in Tab. A.5.

The symmetry group C_{3v} When $d^2 = 3$ the cube is boosted along a corner-centered axis e.g. $(1, 1, 1)$. To an observer in the rest frame the geometrical figure appears as an edge truncated triangular prism as shown in Fig. A.1(c) which is invariant under $C_{3v} \subset O_h$. This case is special because even the cube is not invariant under reflections in planes perpendicular to corner-centered axes and therefore no further restriction is necessary. C_{3v} is the point group of a ditrigonal pyramid, [105]

C_{3v} falls into $N_{\mathcal{C}} = 3$ conjugacy classes.

O	**E**	**C2**	$\mathbf{2\sigma_x}$	$\mathbf{2\sigma_y}$
A1	1	1	1	1
A2	1	1	−1	−1
B1	1	−1	−1	1
B2	1	−1	1	−1

Table A.5: Character Table of C_{2v} the group of full rotoflections of a rhombic pyramid.

E: Identity

2C3: Rotation about $\boldsymbol{p}_{\mathrm{cm}}$ by $\pi/3$

$3\sigma_v$: Reflection in planes perpendicular to an edge-centered axis

According to $N_{\mathcal{C}}$, the number of irreducible representations is $N_\Gamma = 4$ as well. The character table is given in Tab. A.6.

O	**E**	**2C2**	$\mathbf{3\sigma_v}$
A1	1	1	1
A2	1	1	−1
E	2	−1	0

Table A.6: Character Table of C_{3v} the group of full rotoflections of a ditrigonal pyramid.

A.2 Subduction coefficients

Like before let $|\mathrm{L}, m\rangle$ be a basis vector of the the l^{th} angular momentum irrep of SO(3) and m denote the magnetic quantum number. In Sec. 2.3.3 the operator

$$\hat{P}^{\Gamma}_{\alpha\beta}(\boldsymbol{p}) = \frac{\dim(\Gamma)}{|\mathrm{LG}(\boldsymbol{p})|} \sum_{g \in \mathrm{LG}(\boldsymbol{p})} D^{\Gamma}(g)^{*}_{\alpha\beta} \hat{R}_g \tag{2.87}$$

was introduced and it was stated in Eq. (2.89) that it acts as a projection operator from the span of $|\ \mathrm{L}, m\rangle$ to the α^{th} basis state of the lattice irrep Γ (in a moving reference frame characterized by $\boldsymbol{p}$).

This can be proven by showing that $\hat{P}^{\Gamma}_{\alpha\beta}(\boldsymbol{d})\,|\mathrm{L}, m\rangle$ transforms analogously to $|\boldsymbol{p}; \mathrm{L}, m\rangle$ in Eq. (2.100)

$$\mathbb{z}_{\hat{R}}\,|\ \boldsymbol{p}; \Gamma, \alpha\rangle = \sum_{\gamma} D^{\Gamma}(R)_{\gamma\alpha} \left|\ \hat{R}\,\boldsymbol{p}; \Gamma, \gamma\right\rangle \tag{2.100$'$}$$

under any allowed lattice transformation R.

Let $h \in \mathrm{LG}(\boldsymbol{p})$ so that R_h is an allowed lattice rotation. Let $1 \leq \beta \leq \dim(\Gamma)$ and $1 \leq m \leq l$ by arbitrary but fixed. Then

$$\begin{aligned}
\hat{R}_h\,|\boldsymbol{p}; \Gamma, \alpha\rangle &= \sum_{m'} \frac{\dim(\Gamma)}{|\mathrm{LG}(\boldsymbol{d})|} \sum_{g \in \mathrm{LG}(\boldsymbol{d})} D^{\Gamma}(R_g)^{*}_{\alpha\beta}\, D^{\mathrm{L}}(R_g)_{m'm} \hat{R}_h \left|\hat{R}_g \boldsymbol{p}; \mathrm{L}, m'\right\rangle \\
&= \sum_{m'} \frac{\dim(\Gamma)}{|\mathrm{LG}(\boldsymbol{d})|} \sum_{g \in \mathrm{LG}(\boldsymbol{d})} D^{\Gamma}(R_g)^{*}_{\alpha\beta}\, D^{\mathrm{L}}(R_g)_{m'm} \sum_{m''} D^{\mathrm{L}}(R_h)_{m''m'} \left|\hat{R}_h \hat{R}_g \boldsymbol{p}; \mathrm{L}, m''\right\rangle \\
&= \sum_{m''} \frac{\dim(\Gamma)}{|\mathrm{LG}(\boldsymbol{d})|} \sum_{g \in \mathrm{LG}(\boldsymbol{d})} D^{\Gamma}(R_g)^{*}_{\alpha\beta}\, D^{\mathrm{L}}(R_{h\cdot g})_{m''m} \left|\hat{R}_{h\cdot g} \boldsymbol{p}; \mathrm{L}, m''\right\rangle \qquad \text{(A.1)} \\
&= \sum_{m''} \frac{\dim(\Gamma)}{|\mathrm{LG}(\boldsymbol{d})|} \sum_{k \in \mathrm{LG}(\boldsymbol{d})} D^{\Gamma}(R_h^{-1} \cdot R_k)^{*}_{\alpha\beta}\, D^{\mathrm{L}}(R_k)_{m''m} \left|\hat{R}_k \boldsymbol{p}; \mathrm{L}, m''\right\rangle \\
&= \sum_{m''} \frac{\dim(\Gamma)}{|\mathrm{LG}(\boldsymbol{d})|} \sum_{k \in \mathrm{LG}(\boldsymbol{d})} \sum_{\gamma} D^{\Gamma}(R_h^{-1})^{*}_{\alpha\gamma}\, D^{\Gamma}(R_k)^{*}_{\gamma\beta}\, D^{\mathrm{L}}(R_k)_{m''m} \left|\hat{R}_k \boldsymbol{p}; \mathrm{L}, m''\right\rangle \\
&= \sum_{\gamma} D^{\Gamma}(R_h^{-1})^{*}_{\alpha\gamma} \sum_{m''} \left(P^{\Gamma,\mathrm{L}}_{\gamma\beta}\right)_{m''m} \left|\boldsymbol{p}; \mathrm{L}, m''\right\rangle \\
&= \sum_{\gamma} D^{\Gamma}(R_h^{-1})^{*}_{\alpha\gamma}\, |\boldsymbol{p}; \Gamma, \gamma\rangle \\
&= \sum_{\gamma} D^{\Gamma}(R_h)_{\gamma\alpha}\, |\boldsymbol{p}; \Gamma, \gamma\rangle \qquad \text{(A.2)}
\end{aligned}$$

which proves the statement.

The essential reason why $|\Gamma, \alpha\rangle$ defined in Eq. (2.89) transforms correctly under lattice rotations is the interplay of the sum over all group elements and the matrix representation of Γ. This becomes evident in Eq. (A.1). Every piece of the projection operator that has an angular momentum index transforms under R_h like it would in the continuum. $D^{\Gamma}(R_g)^{*}_{\alpha\beta}$ is the only factor where this does not introduce the product $h \cdot g$. Because LG is a group it is closed under

multiplication all products $h \cdot g$ may be re-expressed by k. Because D^Γ is a representation,

$$D^\Gamma(R_g)^*_{\alpha\beta} = \sum_\gamma D^\Gamma(R_h^{-1})^*_{\alpha\gamma}\, D^\Gamma(R_k)^*_{\gamma\beta}$$

which gives the required $D^\Gamma(R_h^{-1})^*_{\alpha\gamma}$. The sum over all group elements is crucial as it guarantees the equality of both sums.

In the proof of Eq. (A.2) the labels β and M simply carried through and were absorbed into $\mid \boldsymbol{p}; \Gamma, \gamma\rangle$ in the final step. The projected states transform correctly independently of the values chosen for β and m. In particular any linear combination is still transforming correctly. When this freedom may be expressed by phases ϕ_β, ϕ_m the projector becomes

$$\hat{P}^\Gamma_{\alpha\beta}(\boldsymbol{p}; \phi_\beta, \phi_m) = \frac{\dim(\Gamma)}{|\mathrm{LG}(\boldsymbol{p})|} \sum_\beta \phi_\beta \sum_m \phi_m \sum_{g \in \mathrm{LG}(\boldsymbol{p})} D^\Gamma(g)^*_{\alpha\beta} \hat{R}_g \,. \tag{A.3}$$

The projection can be interpreted as $\dim(\Gamma) \times (2l+1)$ matrix $c^{\Gamma,\alpha}_{\mathrm{L},m}(\beta, \phi)$ which describes the distribution of $2l+1$ basis vectors of SO(3) into basis vectors of Γ.

$$\mid \boldsymbol{p}; \Gamma, \alpha\rangle = \sum_{m'} \left(\hat{P}^\Gamma_{\alpha\beta}(\boldsymbol{p}; \phi_\beta, \phi_m)\right)_{m'm} \Big| \; \boldsymbol{p}; \mathrm{L}, m' \Big\rangle \tag{A.4}$$

$$\equiv \sum_{m'} c^{\Gamma,\alpha}_{\mathrm{L},m'}(\boldsymbol{p}; \phi_\beta, \phi_m) \Big| \; \boldsymbol{p}; \mathrm{L}, m' \Big\rangle \tag{A.5}$$

The coefficients $c^{\Gamma,\alpha}_{\mathrm{L},m}(\boldsymbol{p}; \phi_\beta, \phi_m)$ may be interpreted as mapping

$$c^{\Gamma,\alpha}_{\mathrm{L},m'}(\boldsymbol{p}; \phi_\beta, \phi_m) : \mathrm{span}\left(\mid \mathrm{L}, m\rangle\right) \to \mathrm{span}\left(\mid \Gamma, \alpha\rangle\right) \,. \tag{A.6}$$

This prescription is often referred to as "subduction". Note, that the mapping only acts in the space of angular momenta. While the coefficients depend on the linear momentum, the linear momentum itself is unchanged by the subduction process. The image of this mapping is a set of $\dim(\Gamma)$ operators. They depend on the phases and in general may be linear dependent or even zero. We use the phase freedom to orthonormalize the resulting set of operators. The phase-fixed set of coefficients is denoted by $s^\Gamma_{\mathrm{L}}(\boldsymbol{p})$ with the dependence on ϕ_β and ϕ_m suppressed.

$$\sum_{m=-l}^{l} s^{\Gamma,\alpha}_{\mathrm{L},m}(\boldsymbol{p})^*\, s^{\Gamma,\alpha}_{\mathrm{L},m}(\boldsymbol{p}) = 1 \tag{A.7}$$

The coefficients $s^\Gamma_{\mathrm{L}}(\boldsymbol{p})$ encapsulate the whole projection. The projection is condensed into a single set coefficient, called "Subduction coefficients"

A.3 Dirac matrix conventions

The ETMC ensembles were generated with the tmLQCD[2] code. We follow the conventions for the Dirac matrix chosen within. They are given by

$$\gamma_0 = \begin{pmatrix} 0 & 0 & 1 & 0 \\ 0 & 0 & 0 & 1 \\ 1 & 0 & 0 & 0 \\ 0 & 1 & 0 & 0 \end{pmatrix} \tag{A.8}$$

$$\gamma_1 = \begin{pmatrix} 0 & 0 & 0 & \mathrm{i} \\ 0 & 0 & \mathrm{i} & 0 \\ 0 & -\mathrm{i} & 0 & 0 \\ -\mathrm{i} & 0 & 0 & 0 \end{pmatrix} \tag{A.9}$$

$$\gamma_2 = \begin{pmatrix} 0 & 0 & 0 & 1 \\ 0 & 0 & -1 & 0 \\ 0 & -1 & 0 & 0 \\ 1 & 0 & 0 & 0 \end{pmatrix} \tag{A.10}$$

and

$$\gamma_3 = \begin{pmatrix} 0 & 0 & \mathrm{i} & 0 \\ 0 & 0 & 0 & -\mathrm{i} \\ -\mathrm{i} & 0 & 0 & 0 \\ 0 & \mathrm{i} & 0 & 0 \end{pmatrix} \tag{A.11}$$

A.4 Implemented diagrams

C2c

$$C = \langle \Gamma_{\mathtt{Op0}} D^{-1}_{\mathtt{Q0}}(t|t') \Gamma_{\mathtt{Op1}} \gamma_5 D^{-1}_{\mathtt{Q1}}(t|t')^\dagger \gamma_5 \rangle \tag{A.12}$$

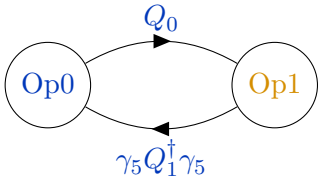

C2+:Op0:Q0:Op1:Q1

Appears in: $\pi^\pm$, $K^\pm$, $\rho^\pm$

C2n

$$C = \langle \Gamma_{\mathtt{Op0}} D^{-1}_{\mathtt{Q0}}(t'|t) \Gamma_{\mathtt{Op1}} D^{-1}_{\mathtt{Q1}}(t|t') \rangle \tag{A.13}$$

[2] https://github.com/etmc/tmLQCD

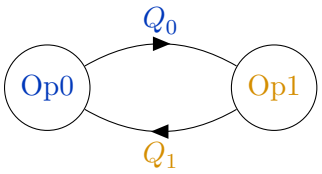

C20:Op0:Q0:Op1:Q1

Appears in: π^0, K^0, σ , ρ^0

C2nV

$$C = \langle \Gamma_{\mathtt{Op0}} D^{-1}_{\mathtt{Q0}}(t|t)\rangle \cdot \langle \Gamma_{\mathtt{Op1}} D^{-1}_{\mathtt{Q1}}(t'|t')\rangle \tag{A.14}$$

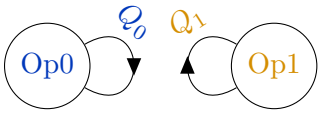

C2nV:Op0:Q0::Op1:Q1

Appears in: σ

C3c

$$C = \langle \Gamma_{\mathtt{Op0}} D^{-1}_{\mathtt{Q0}}(t|t')\Gamma_{\mathtt{Op1}} D^{-1}_{\mathtt{Q1}}(t'|t)\Gamma_{\mathtt{Op2}}\gamma_5 D^{-1}_{\mathtt{Q2}}(t|t)^\dagger\gamma_5\rangle \tag{A.15}$$

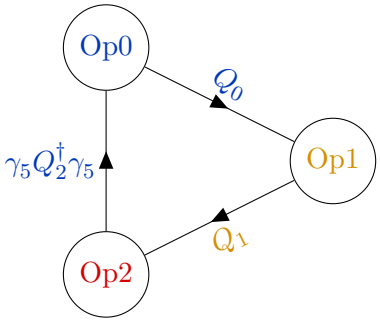

C3+:Op0:Q0:Op1:Q1:Op2:Q2

Appears in: $\pi^+\pi^- \to \rho^0$

C3n

$$C = \langle \Gamma_{\mathtt{Op0}} D^{-1}_{\mathtt{Q0}}(t|t')\Gamma_{\mathtt{Op1}} D^{-1}_{\mathtt{Q1}}(t'|t)\Gamma_{\mathtt{Op2}} D^{-1}_{\mathtt{Q2}}(t|t)\rangle \tag{A.16}$$

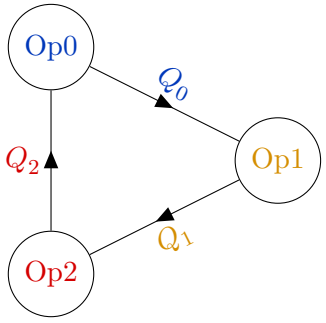

C3n:Op0:Q0:Op1:Q1:Op2:Q2

Appears in: $\pi^0\pi^0 \to \sigma$

C3nV

$$C = \langle \Gamma_{\texttt{Op0}} D^{-1}_{\texttt{Q0}}(t|t) \Gamma_{\texttt{Op1}} D^{-1}_{\texttt{Q1}}(t|t) \rangle \cdot \langle \Gamma_{\texttt{Op2}} D^{-1}_{\texttt{Q2}}(t'|t') \rangle \tag{A.17}$$

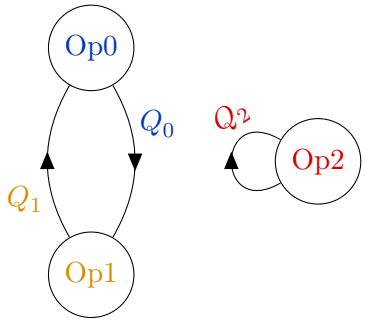

C2nV:Op0:Q0::Op1:Q1:Op2:Q2

Appears in: $\pi^0\pi^0 \to \sigma$

C4cD

$$C = \langle \Gamma_{\texttt{Op0}} D^{-1}_{\texttt{Q0}}(t|t') \Gamma_{\texttt{Op1}} \gamma_5 D^{-1}_{\texttt{Q1}}(t|t')^\dagger \gamma_5 \rangle \cdot \langle \Gamma_{\texttt{Op2}} D^{-1}_{\texttt{Q2}}(t|t') \Gamma_{\texttt{Op3}} \gamma_5 D^{-1}_{\texttt{Q3}}(t|t')^\dagger \gamma_5 \rangle \tag{A.18}$$

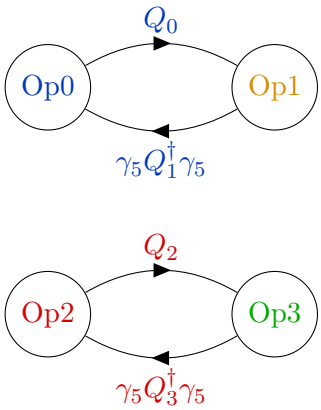

C4+D:0p0:Q0:Op1:Q1:Op2:Q2:Op3:Q3

Apears in: π^+ π^-

C4nD

$$C = \langle \Gamma_{\texttt{Op0}} D^{-1}_{\texttt{Q0}}(t'|t) \Gamma_{\texttt{Op1}} D^{-1}_{\texttt{Q1}}(t|t') \rangle \cdot \langle D^{-1}_{\texttt{Q2}}(t'|t) \Gamma_{\texttt{Op2}} D^{-1}_{\texttt{Q3}}(t|t') \Gamma_{\texttt{Op3}} \rangle \tag{A.19}$$

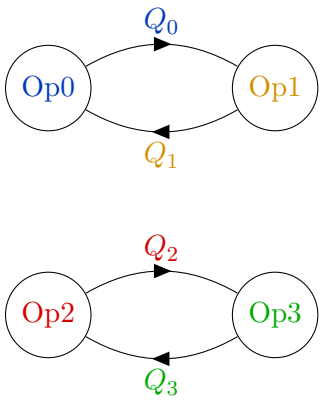

C4nD:Op0:Q0:Op1:Q1:Op2:Q2:Op3:Q3

C4cV

$$C = \langle \Gamma_{\texttt{Op0}} D^{-1}_{\texttt{Q0}}(t|t) \Gamma_{\texttt{Op1}} \gamma_5 D^{-1}_{\texttt{Q1}}(t|t)^\dagger \gamma_5 \rangle \cdot \langle \Gamma_{\texttt{Op2}} D^{-1}_{\texttt{Q2}}(t'|t') \Gamma_{\texttt{Op3}} \gamma_5 D^{-1}_{\texttt{Q3}}(t'|t')^\dagger \gamma_5 \rangle \tag{A.20}$$

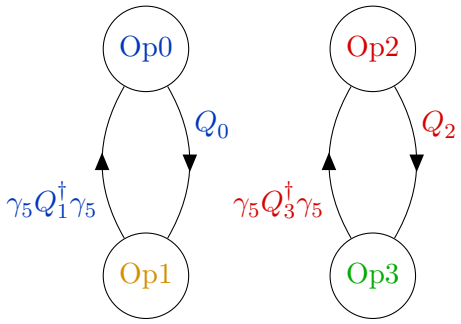

C4+V:Op0:Q0:Op1:Q1:Op2:Q2:Op3:Q3

C4nV

$$C = \langle \Gamma_{\texttt{Op0}} D^{-1}_{\texttt{Q0}}(t|t) \Gamma_{\texttt{Op1}} D^{-1}_{\texttt{Q1}}(t|t) \rangle \cdot \langle \Gamma_{\texttt{Op2}} D^{-1}_{\texttt{Q2}}(t'|t') \Gamma_{\texttt{Op3}} D^{-1}_{\texttt{Q3}}(t'|t') \rangle \tag{A.21}$$

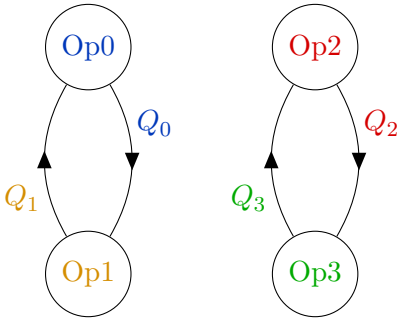

C4nV:Op0:Q0:Op1:Q1:Op2:Q2:Op3:Q3

Apears in: π^0 π^0

C4cB

$$C = \langle \Gamma_{\texttt{Op0}} D^{-1}_{\texttt{Q0}}(t|t')\Gamma_{\texttt{Op1}}\gamma_5 D^{-1}_{\texttt{Q1}}(t'|t')^\dagger \gamma_5 \Gamma_{\texttt{Op2}} D^{-1}_{\texttt{Q2}}(t'|t)\Gamma_{\texttt{Op3}}\gamma_5 D^{-1}_{\texttt{Q3}}(t|t)^\dagger \gamma_5 \rangle \tag{A.22}$$

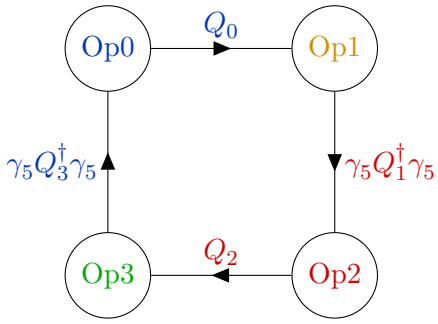

C4+B:Op0:Q0:Op1:Q1:Op2:Q2:Op3:Q3

Appears in: π^+ π^-

C4nB

$$C = \langle \Gamma_{\texttt{Op0}} D^{-1}_{\texttt{Q0}}(t|t')\Gamma_{\texttt{Op1}} D^{-1}_{\texttt{Q1}}(t'|t')\Gamma_{\texttt{Op2}} D^{-1}_{\texttt{Q2}}(t'|t)\Gamma_{\texttt{Op3}} D^{-1}_{\texttt{Q3}}(t|t)\rangle \tag{A.23}$$

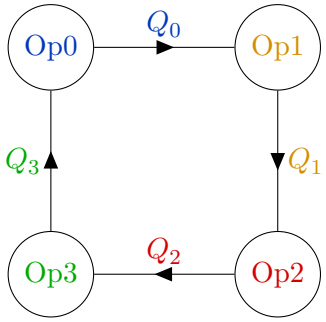

C4nB:Op0:Q0:Op1:Q1:Op2:Q2:Op3:Q3

Apears in: π^0 π^0

C4cC

$$C = \langle \Gamma_{\texttt{Op0}} D^{-1}_{\texttt{Q0}}(t|t')\Gamma_{\texttt{Op1}}\gamma_5 D^{-1}_{\texttt{Q1}}(t|t')^\dagger \gamma_5 \Gamma_{\texttt{Op2}} D^{-1}_{\texttt{Q2}}(t|t')\Gamma_{\texttt{Op3}}\gamma_5 D^{-1}_{\texttt{Q3}}(t|t')^\dagger \gamma_5 \rangle \tag{A.24}$$

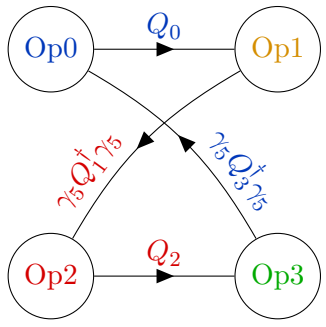

C4+C:Op0:Q0:Op1:Q1:Op2:Q2:Op3:Q3

Appears in: π^+ π^-

C4nC

$$C = \langle \Gamma_{\texttt{Op0}} D^{-1}_{\texttt{Q0}}(t|t') \Gamma_{\texttt{Op1}} D^{-1}_{\texttt{Q1}}(t'|t) \Gamma_{\texttt{Op2}} D^{-1}_{\texttt{Q2}}(t|t') \Gamma_{\texttt{Op3}} D^{-1}_{\texttt{Q3}}(t'|t) \rangle \tag{A.25}$$

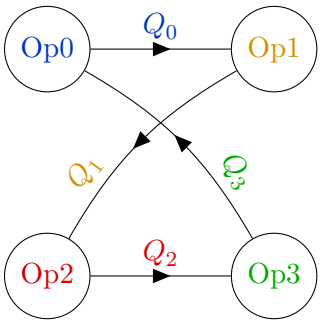

C4nC:Op0:Q0:Op1:Q1:Op:Q2:Op3:Q3

Apears in: π^0 π^0

List of Figures

1.1 Experimental phase shift data for the ρ meson [15]. The characteristic S-shape of resonances can be clearly observed. 2

4.1 Quark line diagram for a charged pion correlation function. 42

4.2 Quark line diagram the disconnected piece of a ρ correlation function. 43

5.1 Visualization of different dilution schemes. Figure courtesy of Martin Ueding . . 58

6.1 Dispersion relation of the pion for ensemble A40.32. 61

6.2 In the left panel we show $\lambda(t, t_0)/C_{\mathrm{th}}(t, t_0)$ as a function of t/a for the ground state energy level in irrep E. The reference time for the GEVP was set to $t_0/a = 3$ and the ensemble is A40.32. The horizontal line with error band indicates the fitted energy value with statistical uncertainty. The extent of the line indicates the fit range. In the right panel we show the effective mass as a function of t/a and the same fitted energy value for reference. 63

6.3 the same as Figure 6.2, but for weighted and shifted $\tilde{\lambda}$. 64

6.4 Example of all energy levels in lattice units for ensemble A40.32 for irrep Γ and $\boldsymbol{p}_{\mathrm{cm}}$ labeled by $\boldsymbol{d}^2$. The two kaon and and two pion thresholds are indicated by the two dashed horizontal lines. The two colours and symbols distinguish the estimate of E_{CM} with and without thermal state removal. 65

6.5 Phase shift δ_1 as a function of E_{CM} in lattice units for ensemble A40.32. The solid line with error band represents the fit result of Eq. (6.7) to all the data w/ thermal state removal. Colours encode the different $\boldsymbol{d}^2$-values, while symbols distinguish the irreps. 66

6.6 We show the phaseshift δ_1 as a function of E_{CM} in lattice units. Left we compare A40.24 (blue) with A40.32 (red) and right B35.48 (red) with B35.32 (blue). The lines with error bars represent the corresponding fits with Eq. (6.7) to the data. . 70

6.7 In the left panel we show $r_0 M_\rho^{\mathrm{av}}$ as a function of $(r_0 M_\pi)^2$. Open symbols are not included in the fit. In the right panel $g_{\rho\pi\pi}^{\mathrm{av}}$ is shown also as a fucntion of $(r_0 M_\pi)^2$. The lines with error bands represent independent fits to the data. 71

6.8 Chiral extrapolation of M_ρ and Γ_ρ as a function of M_π^2, all in units of the Sommer parameter r_0. The lattice spacing is colour and symbol coded, the experimental values are shown as black diamonds. The lines with error bands represent combined fits according to Eq. (6.13) to the data of M_ρ and Γ_ρ. Data points with open symbols are not included in the fit. 72

6.9 Comparison of experimental phase shift data from Ref. [15] to the phase shift curve extracted from our final results for M_ρ and Γ_ρ shown as red solid line. For illustration purposes we also show the phase shift curve in a world with $M_\pi = 220$ MeV as green dashed line, with $M_\pi = 305$ MeV as blue dot-dashed line and with 390 MeV as a purple two-dashed line. 74
6.10 Comparison of lattice results for M_ρ (left) and $g_{\rho\pi\pi}$ (right) as a function of M_π. We compare with all available results that had a dynamic strange quark: Alexandrou et al. [32], Andersen et al. [33], Fu et al. [30], HadSpec [27, 29], PACS-CS [26] as well as the experimental value [38]. 75

A.1 Distorted geometries for the different boosts applied in this work. The transparent color is used to clarify thet reflection in the plane perpendicular to the CM momentum is not a symmetry of the lattice 89

List of Tables

2.1 Choice of reference vectors for the little groups and rotations chosen to relate reference frames to all equivalent moving frames. The physical rotoflections are identified by the Euler angles α, β, γ of the rotation part and the sign i under reflection. 27

3.1 Little groups for all momentum sectors $\boldsymbol{d}^2$ used in this work. Additionally the decomposition of angular momentum irrep for L up to d-wave into irreps of the little group $\mathrm{LG}(\boldsymbol{d}_{\mathrm{cm}})$ is given. [22, 54] 32
3.2 Matrix elements for all momentum sectors $\boldsymbol{d}^2$ and irreps Γ used in this work. Each momentum sector is represented by a single choise $\boldsymbol{d}_{\mathrm{cm}} \in \{\, \boldsymbol{d} \,\}$ and $1 < \alpha < \dim(\Gamma)$. 33
3.3 Juxtaposition of interpolating operators in the physical and twisted basis. 36
3.4 Momentum combinations $\boldsymbol{p}_1 \otimes \boldsymbol{p}_2$ used in Eq. (3.27). We only give one representative CM momentum $\boldsymbol{p}_{\mathrm{cm}} = 2\pi/L\boldsymbol{d}$ for each momentum sector. The other directions may be generated by a global rotation. The momentum combinations depend on the irrep Γ because not all combinations couple to all irreps in which case Eq. (3.27) simply adds up zero. 39
3.5 Same as 3.4 but expressed by $\boldsymbol{q}$ via Eq. (3.24). 39

5.1 The gauge ensembles used in this study. The label is a letter for β followed by $a\mu_\ell \cdot 10^4$, a dot and L/a. In addition to the input parameters relevant for the ensemble generation, we give the spatial and temporal lattice extent as well as the number of evaluated gauge configurations 54
5.2 The gauge ensembles used in this study. The label is a letter for β followed by $a\mu_\ell \cdot 10^4$, a dot and L/a. The most important features are replicated from [35, 36] in physical units. 55
5.3 Values of the Sommer parameter r_0/a and the lattice spacing a at the three values of β. See Ref. [85] for more details. 55
5.4 Choices for number of eigenmodes in dependence of spatial volume 56
5.5 Dilution schemes used in this work for value L of the spatial volume. 58

6.1 ρ mass aM_ρ and coupling $g_{\rho\pi\pi}$ for all ensembles w/ and w/o thermal state removal and the weighted average including the systematic uncertainty as explained in the text. 68
6.2 We give aM_π, the finite size correction factor K_{M_π}, the ρ width $a\Gamma_\rho$ computed from aM_ρ and $g_{\rho\pi\pi}$ using Eq. (6.6) w/ and w/o thermal state removal, and the weighted average as explained in the text. In addition we give the reduced χ^2-values of the corresponding fits to the phase shift data. 69
6.3 Best fit parameters of the combined chiral fit in terms of Z with and without lattice artefacts included in the fit. 73

A.1 Character Table of O the group of proper rotations of an octahadron. 88
A.2 Character Table of C_i the group of inversion. 88
A.3 Character Table of O_h the group of full rotoflections of an octahedron. 89
A.4 Character Table of C_{4v} the group of full rotoflections of a ditetragonal pyramid. . 90
A.5 Character Table of C_{2v} the group of full rotoflections of a rhombic pyramid. . . . 91
A.6 Character Table of C_{3v} the group of full rotoflections of a ditrigonal pyramid. . . 91